Ph.D. Dissertation

International Doctoral School in Information

and Communication Technology

DISI - University of Trento

Advanced Analysis and Synthesis Methods for the Design of Next Generation Reflectarrays

Angelo Gelmini

Tutor:
Paolo Rocca, Associate Professor
University of Trento
Advisor:
Giacomo Oliveri, Associate Professor
University of Trento

October 2019

I wish to thank my parents Mariella and Davide that with their sacrifice, support and example have let me follow my childhood dream of working as a "scientist"

I want to thank also all my familiy, my uncles, cousins and Daniel for the interest and the moral support.

An important thank-you goes to Giulia that has tolerate and support me beyond every difficulties and also to her parents that have accept me in the family.

Special thanks to my friends for the beautiful moments and for having useful and amusing conversations.

To my collegues and friends of the ELEDIA group and to all the people that support me.

Thank you all.

Abstract

The design of reflectarray surface currents that satisfy both *radiation* and user-defined antenna *feasibility* constraints is addressed through a novel paradigm which takes advantage of the non-uniqueness of inverse source (*IS*) problems. To this end, the synthesis is formulated in the *IS* framework and its *non-measurable* solutions are employed as a design *DoF*. Thanks to the adopted framework, a closed-form expression for the design of reflectarray surface currents is derived which does not require any iterative local/global optimization procedure and which inherently satisfies both the radiation and the feasibility design constraints. The features and potentialities of the proposed strategy are assessed through selected numerical experiments dealing with different reflectarray aperture types/sizes and forbidden region definitions.

Keywords
Reflectarray Synthesis, Non-Radiating Currents, Inverse Source Problems, Constrained Reflectarray Design.

Published Conference Papers

[C1] G. Oliveri, F. Apolloni, A. Gelmini, E. Bekele, S. Maci, and A. Massa, "Numerical homogenization and synthesis of wave polarizers through the material-by-design paradigm," *9th European Conference on Antennas and Propagation (EUCAP 2015)* (ISBN 978-8-8907-0185-6), Lisbon, Portugal, pp. 1-4, April 12-17, 2015.

[C2] N. Anselmi, M. Donelli, A. Gelmini, G. Gottardi, G. Oliveri, L. Poli, P. Rocca, L. Tenuti, and A. Massa, "Design and optimization of advanced radar and communications systems and architectures @ ELEDIA Research Center," *Atti XXI Riunione Nazionale di Elettromagnetismo (XXI RiNEm)*, Parma, pp. 164-167, 12-14 Settembre 2016.

[C3] G. Oliveri, M. Salucci, A. Gelmini, L. Poli, P. Rocca, and A. Massa, "SAR array synthesis for next generation Earth observation systems," *11th European Conference on Antennas and Propagation (EUCAP 2017)* (no. 978-88-907018-7-0/17/$31.00©2017 IEEE), Paris, France, pp. 2312-2314, March 19-24, 2017.

[C4] G. Oliveri, A. Gelmini, M. Salucci, D. Bresciani, and A. Massa, "Exploiting non-radiating currents in reflectarray antenna design," *11th European Conference on Antennas and Propagation (EUCAP 2017)* (no. 978-88-907018-7-0/17/$31.00©2017 IEEE), Paris, France, pp. 88-91, March 19-24, 2017.

[C5] A. Gelmini, G. Gottardi, and T. Moriyama, "A compressive sensing-based computational method for the inversion of wide-band ground penetrating radar data," *7th International Workshop on New Computational Methods for Inverse Problems (NCMIP 2017)*, Cachan, France, May 12, 2017.

[C6] M. Salucci, G. Oliveri, A. Gelmini, D. Bresciani, and A. Massa ,"Reflectarray antenna simplification through non-radiating currents synthesis," *2017 IEEE AP-S International Symposium and USNC-URSI Radio Science Meeting* (no. 978-1-5386-3284-0/17/$31.00©2017 IEEE), San Diego, California, USA, pp. 1185-1186, July 9-15, 2017.

[C7] A. Gelmini, M. Salucci, G. Oliveri, and A. Massa, "Robust diagnosis of planar antenna arrays through a Bayesian compressive sensing approach," *6th Asia-Pacific Conference on Antennas and Propagation (APCAP 2017)*, Xi'an, 2017, pp. 1-3. doi: 10.1109/APCAP.2017.8420936.

[C8] M. Salucci, A. Gelmini, G. Oliveri, and A. Massa, "Exploitation of frequency diversity in GPR imaging through an innovative constrained-BCS method," *12th European Conference on Antennas and Propagation (EUCAP 2018)* , London, United Kingdom April 9-13, 2018.

[C9] A. Gelmini, M. Salucci, G. Oliveri, and A. Massa, "Innovative synthesis of reflectarrays within the non-radiating inverse source framework," *12th European Conference on Antennas and Propagation (EUCAP 2018)*, London, United Kingdom, pp. 1-4, April 9-13, 2018 (DOI: 10.1049/cp.2018.0864).

[C10] M. Bertolli, M. Donelli, A. Massa, G. Oliveri, A. Polo, F. Robol, L. Poli, A. Gelmini, G. Gottardi, M. A. Hannan, L. T. P. Bui, P. Rocca, C. Sacchi, F. Viani, T. Moriyama, T. Takenaka, and M. Salucci, "Computational methods for wireless structural health monitoring of cultural heritages," *8th International Conference on New Computational Methods for Inverse Problems (NCMIP 2018)*, Cachan, France, May 25, 2018.

[C11] M. Salucci, G. Oliveri, A. Gelmini, and A. Massa, "Overcoming feasibility constraints in reflecrattary design by exploiting non-radiating currents," *2018 IEEE AP-S International Symposium and USNC-URSI Radio Science Meeting* Boston, Massachussets, USA, July 8-13, 2018.

[C12] N. Anselmi, A. Gelmini, G. Gottardi, G. Oliveri, L. Poli, P. Rocca, M. Salucci, and A. Massa, "Inverse Scattering Methodologies and Applications @ ELEDIA Research Center," *Atti XXII Riunione Nazionale di Elettromagnetismo (XXII RiNEm)*, Cagliari, pp. 325-328, 3-6 Settembre 2018.

[C13] N. Anselmi, R. Azaro, P. Bui, A. Gelmini, G. Gottardi, A. Hannan, G. Oliveri, L. Poli, A. Polo, F. Robol, P. Rocca, M. Salucci, and A. Massa, "Antenna Synthesis and Optimization @ ELEDIA Research Center," *Atti XXII Riunione Nazionale di Elettromagnetismo (XXII RiNEm)*, Cagliari, pp. 333-336, 3-6 Settembre 2018.

[C14] M. Salucci, A. Gelmini, G. Oliveri, and A. Massa, "From inverse-source problems to reflectarray design - An innovative approach for dealing with manufacturing and geometrical constraints," *13th European Conference on Antennas and Propagation (EUCAP 2019)*.

[C15] G. Oliveri, M. Salucci, A. Gelmini, and A. Massa, "Computationally-efficient synthesis of advanced reflectarrays through a system-by-design tool," *13th European Conference on Antennas and Propagation (EUCAP 2019*).

[C16] A. Polo, M. Salucci, A. Gelmini, G. Gottardi, G. Oliveri, P. Rocca, and A. Massa, "Advanced teaching in EM - Towards an integration of theoretical skills and applicative/industrial skills," *13th European Conference on Antennas and Propagation (EUCAP 2019)*.

[C17] G. Oliveri, M. Salucci, A. Gelmini, and A. Massa, "Frontiers in reflectarray design," *2019 IEEE AP-S International Symposium and USNC-URSI Radio Science Meeting*, Atlanta, Georgia, USA.

[C18] G. Oliveri, A. Gelmini, G. Gottardi, and M. Salucci, "Metamaterial-by-design - A Paradigm for the industrial synthesis of EM manipulation devices," *2019 IEEE International Conference on Microwaves, Communications, Antennas & Electronic Systems (COMCAS 2019)*.

Published Journals Papers

[R1] A. Gelmini, G. Gottardi, and T. Moriyama, "A compressive sensing-based computational method for the inversion of wide-band ground penetrating radar data," *Journal of Physics: Conference Series*, , vol. 904, pp. 1-7, 2017 (extended version submitted to revision by an international comitee of [C5]) (DOI: 10.1088/1742-6596/904/1/012002).

[R2] M. Salucci, A. Gelmini, L. Poli, G. Oliveri, and A. Massa, "Progressive compressive sensing for exploiting frequency-diversity in GPR imaging," *Journal of Electromagnetic Waves and Applications*, vol. 32, no. 9, pp. 1164-1193, 2018 (DOI: 10.1080/09205071.2018.1425160).

[R3] M. Salucci, A. Gelmini, G. Oliveri, and A. Massa, "Planar arrays diagnosis by means of an advanced Bayesian compressive processing," *IEEE Transactions on Antennas and Propagation*, vol. 66, no. 11, pp. 5892-5906, November 2018 (DOI: 10.1109/TAP.2018.2866534).

[R4] M. Salucci, A. Gelmini, G. Oliveri, N. Anselmi, and A. Massa, "Synthesis of shaped beam reflectarrays with constrained geometry by exploiting non-radiating surface currents," *IEEE Transactions on Antennas and Propagation*, vol. 66, no. 11, pp. 5805-5817, November 2018 (DOI: 10.1109/TAP.2018.2869036).

[R5] M. Bertolli, M. Donelli, A. Massa, G. Oliveri, A. Polo, F. Robol, L. Poli, A. Gelmini, G. Gottardi, M. A. Hannan, L. T. P. Bui, P. Rocca, C. Sacchi, F. Viani, T. Moriyama, T. Takenaka, and M. Salucci, "Computational methods for wireless structural health monitoring of cultural heritages," *Journal of Physics: Conference Series*, vol. 1131, pp. 1-7, 2018 (extended version submitted to revision by an international comitee of [C10]) (DOI: 10.1088/1742-6596/1131/1/012005).

[R6] M. Salucci, A. Gelmini, J. Vrba, I. Merunka, G. Oliveri, and P. Rocca, "Instantaneous brain stroke classification and localization from real scattering data," *Microwave and Optical Technology Letters*, vol. 61, no. 3, pp. 805-808, March 2019 (DOI: 10.1002/mop.31639).

Contents

List of Tables

List of Figures

Chapter 1

Introduction

Antennas able to exhibit high gains and carefully shaped patterns are of fundamental importance in radar, satellite remote sensing and long-distance/high-capacity communication systems [1]-[6].

In order to meet such ambitious performance requirements, the technologies traditionally employed are reflector antennas [6] and phased arrays[7],[8]. In fact both technologies can achieve a very high gain and are able to generate shaped patterns. In reflector antenna the high gain capability is achieved thanks to the ability to concentrate the field that is coming from the feeder to a single direction in space (due to the parabolic reflector), while the shaped beam can be obtained by shaped profile reflectors (adding some "bumps" into the paraboloid reflector surface) [9].

In [9] it is proposed to use an optimization procedure that takes in input the type of the reflector surface (circular, ellipsoid, square, rectangular, conic etc..), the feed configuration (horn antenna, array antennas, etc..) and position (at the center or shifted), the reflector configuration (single reflector, dual reflector, Cassegrain, etc..) and the radiation characteristics. The optimizer computes the radiated pattern applying the theory of generalized diffraction, i.e. the physical theory of diffraction is used to analyse the antenna and produce a cost function to quantify the matching of the radiation characteristics.If the cost function is not minimized, the optimizer creates a new trial solution.

In phased arrays, high gain and a properly shaped beam are given by the position of the elements (regular lattice, sparse lattice, random lattice, etc..), the element pattern and the weighting function applied to each element (e.g.:

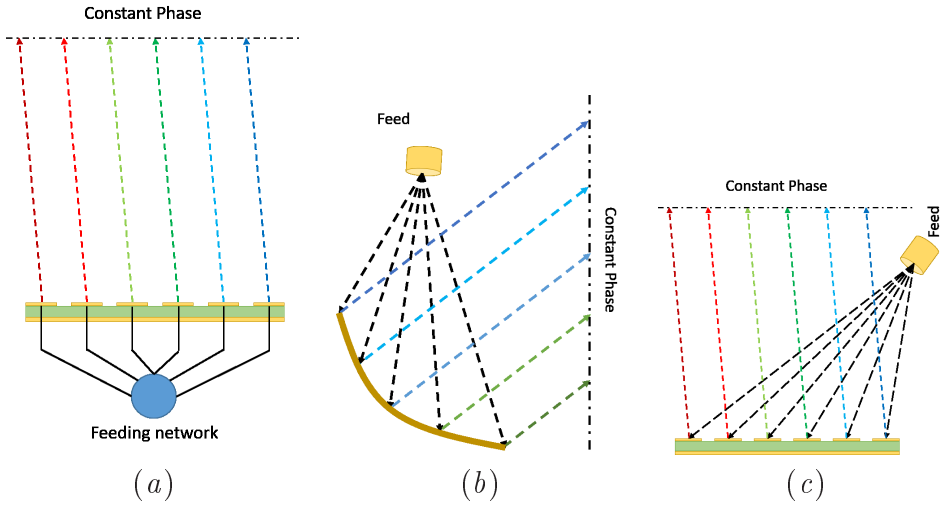

Figure 1.1: Geometry comparison of (a) Phased Array Antenna, (b) Reflector Antenna, (c) Reflectarray Antenna.

tapering, thinning, phase synthesis, time modulated array, clustering techniques, etc..)[7][8].

Though able to achieve the desired requirements, both solutions have significant drawbacks. Reflector antennas exhibit high manufacturing complexity, are difficult to be implemented as reconfigurable antennas (unless mechanical steering is considered, which is typically avoided in space applications) and are also characterized by non-conformal shapes [6]. Moreover, space application reflector antennas suffer manufacture tolerance and deformation problems [10] that can severely affect the antenna operational. Phased antenna arrays are expensive in terms of fabrication and power consumption (and, consequently, need temperature control, not suitable for space applications). In addition, such antennas are also heavy due to support and feeding network, and their design is not trivial [7][8].

In order to deal with the aforementioned issues, reflectarray antennas have emerged as a possible solution to yield high-gain shaped beam antennas with low realization costs, flat/conformal shapes, and low-consumption feed networks [6],[11]. Thanks to their potentials and flexibility [6],[12]-[36], the design of shaped-beam reflectarray antennas has become a very active research field and several methodologies have been proposed to this end [37]-[52].

The key factor that helped the success of reflectarray antennas is their capa-

bility of combining the positive features of both classical reflector antennas (i.e., high gain, low cost and easy fabrication) [6] and phased arrays (i.e., reconfigurability and low profile)[7]. Typically, they consist of a planar array of microstrip patches printed on a ground-backed dielectric substrate and illuminated by a feeder (e.g., a horn antenna, or also a phased array). Size, shape and arrangement of the metallic patches are properly designed such that the field reflected by the passive/active surface meets the desired pattern features (e.g., steering angle, sidelobe level, bandwidth, etc..)[6]. As a main consequence, reflectarrays do not require the use of a bulky parabolic disc, while the tuning of the radiated field is obtained without the need for expensive beam-forming networks or mechanical steering [14].

The first example of a reflectarray antenna was proposed at the beginning of 60's by Berry [11], who proposes to use truncated waveguides as reflecting elements. These waveguides have different lengths that are able to impose a proper phase shift to obtain a desired reflected pattern. The reflectarrays produced with this technology can achieve good performances and can handle very high power (no dielectric substrate) at the cost of using a heavy structure. For this reason, only with the development of the microstrip technology in the late 80's the reflectarray arose as a leading technology.

Before microstrip technology, another kind of reflecting structure was analyzed: the Spiralphase reflectarray [53]. In this work four arms of spirals are connected with switching diodes that activate a different pair of arms and thus permit to control the scan angle of the circular polarized reflectarray. However, due to the diodes circuit and the spiral cavity ($\lambda/4$), the structure becomes too bulky to permit an efficient implementation.

The simplest design of a reflectarray is proposed in [54] and [55] and implemented by [56],[57] [Fig. 1.2(a)], and consists in microstrip patches with fixed shape and different adapting stubs. Since these stubs have different lengths, they can provide a different impedance, and consequently a different phase shift. The major problem with the stub technology is that this method is inherently narrowband, since the stub structure must be dimensioned for a specific wavelength, and parasitic coupling with adjacent elements could be a possible issue.

Pozar et al. in [58],[59] and Chaharmir et al. [60] propose to introduce, in the same planar structure, patches with different dimension, rotation, or even different geometry in order to introduce a different phase shift for each element.

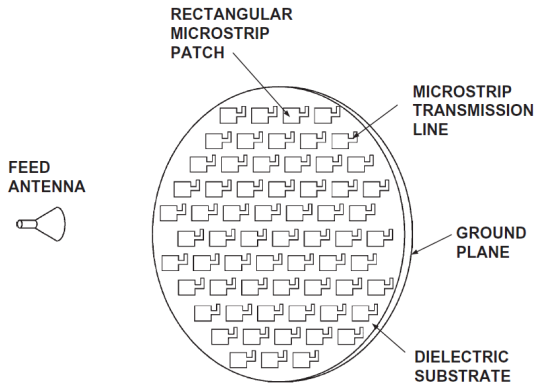

(a)

/media/new_home/Ph.D.Thesis/Ph.D.Thesis.GEL

(b)

Figure 1.2: Reflectarray Antenna implemented by (a)[56] and by (b)Pozar (http://www.ecs.umass.edu/ece/pozar/reflect.jpg).

This kind of design solves the problems of the stubs, improves the bandwidth and allows the designer to have a better control on polarization. However, a trade-off must be taken into account when designing reflectarray antennas that radiated shaped beams. If a particular shaped beam is desired in order to cover only some regions of the Earth (e.g. a beam that can cover northern Europe without sending power on sea areas) the phase distribution on the reflectarray aperture has a non-smooth behavior. This means that adjacent elements could have a significantly different phase shift and this implies very different and complex shapes. As a consequence, manufacturing costs are high (also due to manufacture tolerances), and there may also be problems involving incorrect shape definition and coupling. This kind of design is improved by Encinar et al. in [15],[16],[37],[61] that propose to design shaped beams by using more layers (2 or 3) of different shaped patches and exploiting an optimization technique in order to define the best phase distribution on different layers. This kind of design, based on multiple layers, can improve the performance and decrease the complexity of each singular layer, although the overall structure is still complex, expensive to manufacture, and it could be hard to insert a control network for beam-steering applications.

In general, reflectarray layouts are usually synthesized by a two-step procedure in which:

(*a*) the reflectarray surface currents that radiate the desired shaped beam are

computed;

(*b*) the feed and reflecting elements (e.g., microstrip patches) able to approximately generate such currents are deduced/designed.

Several methods have been developed in the literature to solve (*b*) for various unit cell geometries and architectures [2],[6],[15],[59],[62]-[66]. On the contrary, very few approaches have been proposed to address (*a*) [37]-[39].

One example of solution in literature that deals with *step (b)* is [59], in which the authors describe a method of computing the phase response characteristics for a square patch microstrip and then synthesizing the patch distribution to obtain a pencil beam in different reflectarray configurations: squared reflectarray offset beam having the feeder in broadside, circular diameter reflectarray with both feeder and far-field maximum in broadside, square reflectarray with prime focus rectangular horn and square reflectarray in Cassegrian configuration.

Instead [15] [Fig. 1.3(*a*)], in order to enlarge the operational bandwidth of the system, a multi-layer structure is employed. In particular the number of layer is set to 2 and a simple square patch is selected to have the desired phase shift. More in detail, the size of the side of the square patch can vary the phase response of the specific cell and by fixing the ratio between the cell in the two layers (the upper layer patches are 0.7 times the lower layer ones) the reflectarray is synthesized using the simple phase delay compensation (the phase of the patch has to compensate the same travelling time that should be occurred in case of a reflector) and good performance are obtained within 16.67% of the operational bandwidth.

When reflectarray patches are designed, a problem that can occur is that their phase response does not cover the full 360° phase range. To overcome this problem [64] [Fig. 1.3(*b*)]propose to use a kind of structure that is cyclic. This kind of element comes back to the original geometry shape when a full phase range is covered. In fact the proposed element is a "phoenix element" (i.e. called phoenix for its rebirthing capabilities) that is composed by a centered square patch of fixed dimension, an external ring of fixed dimension that delimits the element with the adjacent ones and a variable ring that can "move" from the inner to the outer. Furthermore, this element is designed to be metal-only, thus without the presence of the substrate (in fact the inner patch, the varying ring

and the external one are connected by a metallic strip). This element can increase the efficiency of the reflectarray since it can cover the full phase range and it does not require any dielectric substrate. Nonetheless, the connecting strips exhibits some drawbacks in controlling the cross-polarization.

To better control the cross polarization, but maintaining the full range cover, it is proposed by [65] [Fig. 1.3(c)] to use two different cycles to define the element. Firstly the element is made by dipole crossed with same arms (to ensure dual-polarization), whose width is half of their length. To implement the cycle, the length is increased until the element touches the adjacent ones, then the element geometry changes and becomes a grid. The second step of the cycle is done keeping fixed the length and vary only the width of the arms unless the metalization disappear, then the cycle restart as a crossed dipole. The designed reflectarray using this elements can handle both polarizations and demonstrate to have an operational bandwidth of 11.1%.

Reflectarray are used also for non-microwave application moving to the terahertz domain [66] [Fig. 1.3(d)]. In this domain stubs or many cells with different shapes can not be manufactured (or are too expensive). Thus, it is proposed to use metal blocks with different height in order to compensate the phase with respect to a reference plane. In this way it is the same as if the physical behavior of a reflector is obtained by sampling and then applying a modulus operation with respect to the wavelength at the heights of the blocks. It is demonstrated that with this approach a good gain can be achieved and the pattern behavior is quite stable to the frequency band (30%) obtaining also a very good performance in antenna efficiency due to the absence of dielectrics.

Considering step (a), the exploitation of local optimization strategies (such as the *Intersection Approach* [37],[39]) has been proposed as a first step of a shaped beam reflectarray synthesis [37],[39]. However, such methodologies can be computationally expensive (especially if wide apertures are at hand) and their effectiveness and convergence rate strongly depend on the choice of the initialization point [37]. Alternatively, ray-tracing techniques have been proposed to deduce the reflectarray surface currents starting from the knowledge of a previously synthesized shaped reflector affording the desired beam pattern [38]. Unfortunately, such a strategy does not allow the designer to specify any feasibility constraints on the solution (e.g., presence of "forbidden regions" in the array aperture) and therefore it does not guarantee that the deduced currents are implementable.

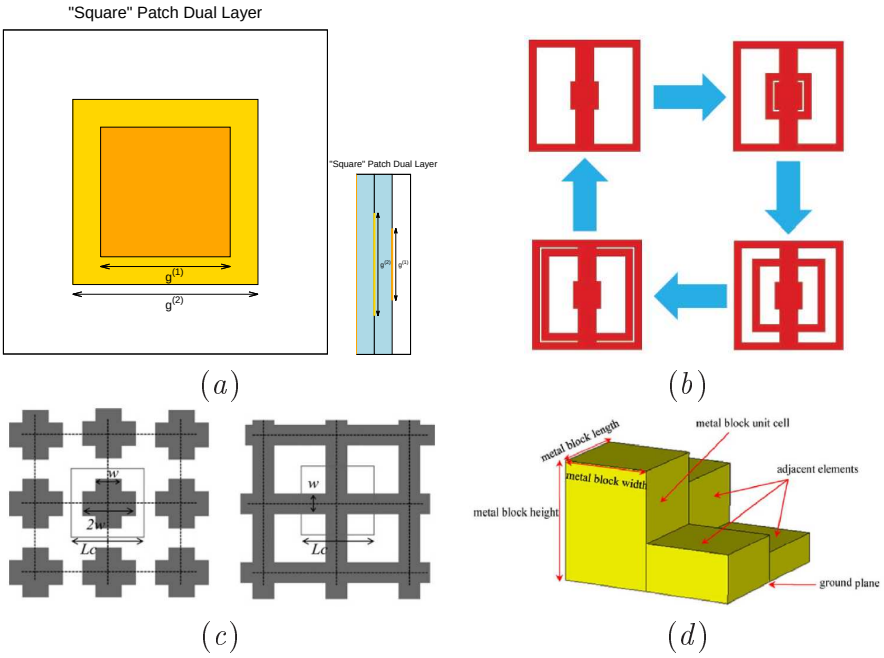

Figure 1.3: Geometry of the reflectarray antenna elements: (a)[15], (b)[64], (c)[65], (d)[66].

In the *Intersection Approach* [67] two sets are considered: the first set is composed by all the radiation pattern that respects the required specification and the second contains all the radiation pattern that the reflectarray can radiate. Roughly, the synthesis procedure makes continue projection of the patterns in the two sets from the first set to the second, until the mismatch between the projected patterns is almost null. Thus, as the dimension of the reflectarray increases the dimension of the sets increases as well, and this is one of the drawbacks of techniques explained in [37],[39]. While [37] has a reflectarray made with three layer of squared patches and can achieve very good performance in covering the South America region with a bandwidth of 10%, and [39] (that has also used the FFT to increase efficiency of the approach) can achieve good performance with a reflectarray made of black boxes (it does not take into account the real element, only its reflection coefficient) synthesizing an isoflux pattern and a shaped-beam for the Europe covering with a Direct Broadcast Satellite (DBS).

From a different perspective, it is known that the relation between the reflectarray currents and their radiated patterns can be effectively modeled exploiting Green's functions theory [6][68]. Accordingly, problem (a) can be actually seen

as an *inverse source* (*IS*) one [69]-[72] where the data is the desired beam pattern and the unknowns are the surface currents.

In [69] and [70] the problem addressed is to retrieve the current distribution that radiates a measured field. In the first one it is minimized the distance of reconstructed Equivalent Magnetic Current (*EMC*) by the near-field measured in a cylindrical way using the Marquardt algorithm, and in the second its almost the same but taking into account a near-field measured on a spherical surface (hence three components of the field, instead of only two).

In [71] the problem is to reconstruct equivalent currents distribution using integral equation algorithm. Using the integral equation the authors are able to reconstruct the current over user-defined surfaces, not only cylindrical or spherical surface (that are easier to compute using the tangential fields and the Equivalence Principle) but also, for example, on the surface of a horn antenna.

In [72] metallic bodies are reconstructed as equivalent currents. In particular the Source Reconstruction method is applied to the retrieval of metal object in an investigation domain and use a minimization (using a *Conjugate Gradient* method) of a cost function that, taking into account the Tikhonov regularization and the normalization of the equations terms, of the $\mathcal{L}_2$-norm of the measured and reconstructed field (by the radiation of the equivalent current).

In the framework of inverse scattering and antenna diagnosis/characterization [69]-[72], such a problem is known to be ill-posed because of the non-uniqueness of the radiation operator [73], which is related to the existence of *non-measurable/non-radiating* currents [74]-[76]. While this feature can be an issue in traditional inverse problems requiring suitable countermeasures [74]-[76], it actually represents a degree-of-freedom (*DoF*) in the framework of constrained reflectarray design. In fact, by superimposing a suitably designed *non-measurable* current to an available (e.g., minimum-norm [74]-[77]) solution of the *IS* problem, a current could be synthesized which radiates the desired far-field pattern, and complies with the user-defined constraints.

According to such considerations, an innovative paradigm to synthesize reflectarray surface currents [i.e., to address step (*a*)] is proposed which, by leveraging on the non-uniqueness of the *IS* problem as a design *DoF*, enables to deduce solutions also satisfying user-defined antenna feasibility constraints (e.g., on the presence and shape of "forbidden regions" in the aperture). To this end, the design is formulated a two step process in which (*i*) the *minimum-norm* solution of

the *IS* problem is firstly derived, and then (*ii*) a suitable *non-measurable* source is computed so that the resulting surface current [i.e., the superposition of the solutions (*i*) and (*ii*)] complies with the user-defined requirements. Thanks to the features of the proposed formulation, a closed-form expression is finally derived for both the *minimum-norm* and the *non-measurable* currents which does not require any iterative local/global optimization procedure and which inherently satisfies both the radiation and the feasibility design constraints.

In particular, it is proposed to apply the Singular Value Decomposition (*SVD*) to a defined Green's operator. The outcome of this process are two set of orthonormal bases and a matrix of singular values. This output has to be analyzed in order to find a good trade-off between, on one side, the precision of the minimum-norm current able to radiate the desired field; on the other side, the possibility to have the greatest number of non-measurable bases. This analysis it is done by defining a variable threshold on the value of the singular values and collecting different combination of orthonormal bases that are linked to the singular values above or below the threshold.

The innovative methodological contributions of the paper therefore include the introduction, for the first time to the best of the author knowledge, of a reflectarray surface current synthesis paradigm which leverages on the non-uniqueness of the *IS* problem and the existence of non-measurable currents to improve the features of the obtained solution (e.g., in terms of feasibility), and the introduction of explicit *closed-form* expressions for the computation of reflectarray surface currents affording a desired far-field pattern and complying with geometrical constraints regarding the presence of "forbidden regions".

Thesis outline

The thesis is organized as follows. After the formulation of the shaped-beam constrained reflectarray currents synthesis problem (Chapter 2), the proposed design method is illustrated and its final closed-form solution is derived (Chapter 3). A set of numerical examples based on realistic reflectarray architectures are then illustrated to assess the effectiveness and potentialities of the considered design paradigm (Chapter 4). At the end are presented the conclusion and remarks (Chapter 5).

Chapter 2

Problem Formulation

In this chapter the problem formulation is explained throgh the understanding of the radiation problem in a reflectarray antenna and how to formulate it as an *Inverse Source* problem. In particular, firstly it is described the radiation problem formulation and its discretization on the reflectarray surface (that is not continuous) and then the problem to find the current that generate a specified radiated field is formulated as an *Inverse Source* problem.

2.1 Radiation from surface current

We consider a reflectarray antenna, oriented like in Fig. 2.1, with both ground plane and patches made by a Perfect Electric Conductor separated by a layer of substrate with standard complex permittivity value $\varepsilon = \varepsilon_0 \varepsilon_r \left(1 - j \tan\delta\right)$ and illuminated by a feeder positioned in $\mathbf{r}^f = (x_f,\, y_f,\, z_f)$ that in far-field generates a plane-wave that has a relative angular position $(\theta_{inc}, \phi_{inc})$ (see Fig. 2.1). The incident vector for each cell of the reflectarray is $\underline{\nu}^{inc}(\mathbf{r}) = -(\sin\theta_{inc}\cos\phi_{inc},$ $\sin\theta_{inc}\sin\phi_{inc},\ \cos\theta_{inc})$.

The incident plane wave on a reflectarray element can be model as:

$$\begin{bmatrix} E^{\theta}_{inc} \\ E^{\phi}_{inc} \end{bmatrix} = \begin{bmatrix} E^{\theta}_{0} \\ E^{\phi}_{0} \end{bmatrix} e^{-jk\left(\underline{\nu}^{inc}(\mathbf{r})\cdot\underline{r}\right)} \tag{2.1}$$

where $\underline{E}_0$ is the vector that describes amplitude and polarization of the incident plane-wave, $\underline{r}$ is the position of the reflectarray element, $k = 2\pi f\sqrt{\mu\varepsilon}$, μ, ε are

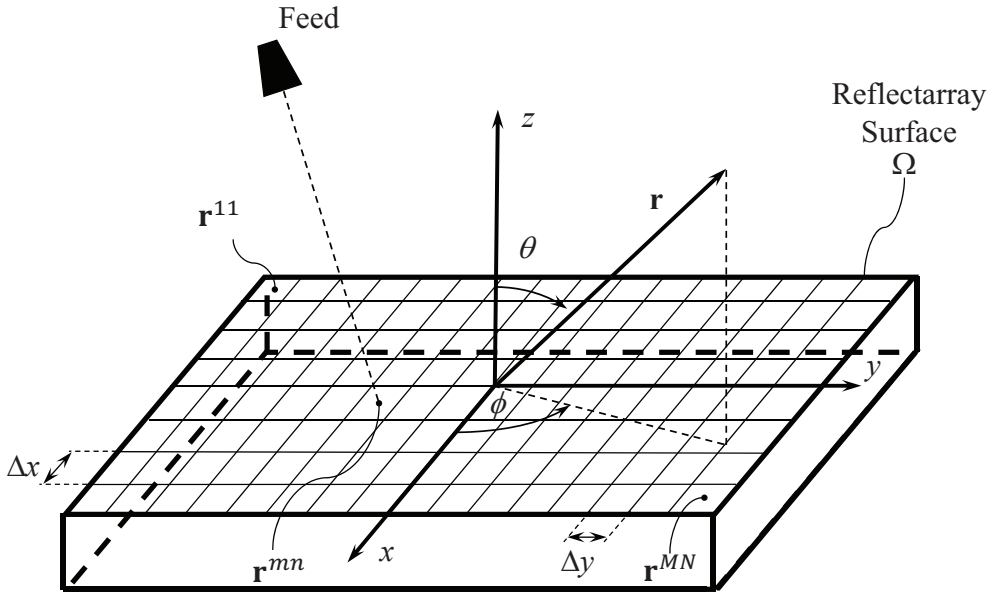

Figure 2.1: Geometry of the reflectarray antenna.

the free-space wave number, permeability, and permittivity, respectively, and f is the frequency.

The presence of the grounded dielectric slab and of the layer printed patches generates different kind of field that are back-radiated. The total field that is present in the region of the space in front of the reflectarray antennas can be described as the sum of these contributes:

$$\underline{E}_{tot} = \underline{E}_{inc} + \underline{E}_{RGDS} + \underline{E}_{RPP} \tag{2.2}$$

The term $\underline{E}_{RGDS}$ indicates the reflected field by the infinite grounded dielectric slab without any kind of patch printed on, and can be definite as:

$$\underline{E}_{RGDS} = \mathbf{R}\underline{E}_0 e^{jk(x\sin\theta_{inc}\cos\phi_{inc}+y\sin\theta_{inc}\sin\phi_{inc}-z\cos\theta_{inc})} \tag{2.3}$$

where matrix $\mathbf{R}$ is the diagonal reflection matrix, and its non-null entries $R_{\theta\theta}$ and $R_{\phi\phi}$ are defined as in [79].

The other term $\underline{E}_{RPP}$ represents the reflected field when the microstrip patches are present. On this patches, made of *PEC,* the $\underline{E}_{inc}$ induces a sur-

face current that radiates a field defined as:

$$\underline{E}_{RPP} = \mathbf{S}\underline{E}_0 e^{jk(x\sin\theta_{inc}\cos\phi_{inc}+y\sin\theta_{inc}\sin\phi_{inc}-z\cos\theta_{inc})} \tag{2.4}$$

where $\mathbf{S}$ is the scattering matrix and its coefficients characterize the reflection:

$$\mathbf{S} = \begin{bmatrix} S_{\theta\theta} & S_{\theta\phi} \\ S_{\phi\theta} & S_{\theta\theta} \end{bmatrix} \tag{2.5}$$

Each scattering coefficient is defined as the ratio between the scattered and incident field of the microstrip surface for each polarization:

$$S_{ji} = \frac{E^j_{RPP}(z=0)}{E^i_{inc}(z=0)} \quad j,i = \{\theta,\phi\} \tag{2.6}$$

These coefficients can be computed for each microstrip patch and then used to obtain the surface current on the reflectarray aperture. Since we want to defined the current on the microstrip surface $\underline{J}_s$:

$$\underline{J}_s = \hat{\underline{n}} \times \underline{H} \tag{2.7}$$

(where $\hat{\underline{n}}$ is the normal to the surface) and we have defined all the terms in (2.2) we can express also the total magnetic field as:

$$\underline{H} = \frac{1}{\eta}\underline{\nu}^{inc} \times \underline{E}_{inc} + \frac{1}{\eta}\underline{\nu}^{refl} \times \underline{E}_{RGDS} + \frac{1}{\eta}\underline{\nu}^{refl} \times \underline{E}_{RPP} \tag{2.8}$$

where $\underline{\nu}^{refl}$ is the specular reflection direction (Snell's law on a PEC) of the incidence direction $\underline{\nu}^{inc}$, and η is the free-space impedance.

In case of far-field, following [80], the radiated field by an electric current $\underline{J}_s$ can be approximates as:

$$\underline{E}_{RAD}(\underline{r}) \approx -j\eta\frac{\exp(-jkr)}{2\lambda r}\left(N_\theta(\theta,\phi) + N_\phi(\theta,\phi)\right) \tag{2.9}$$

where the radiation vector in carthesian coordinates $\underline{N}$ can be expressed as

$$\begin{aligned}\underline{N}(\theta,\phi) = \; & \int\int_\Omega \left[J_x(\underline{r})\,\hat{\underline{x}} + J_y(\underline{r})\,\hat{\underline{y}}\right] \times \\ & \exp\left(j\tfrac{2\pi}{\lambda}\left(x\sin\theta\cos\phi + y\sin\theta\sin\phi\right)\right)\,\mathrm{dx}\,\mathrm{dy}\end{aligned} \tag{2.10}$$

and λ is the wavelength.

In order to be easier computed the radiation vectors can be expressed in spherical coordinates form:

$$\begin{cases} N_\theta(\theta,\phi) = N_x(\theta,\phi)\cos\theta\cos\phi + N_y(\theta,\phi)\cos\theta\sin\phi \\ N_\phi(\theta,\phi) = -N_x(\theta,\phi)\sin\phi + N_y(\theta,\phi)\cos\phi \end{cases} \tag{2.11}$$

In this way, bu substituting (2.11) in (2.9) we can obtain:

$$\begin{cases} \underline{E}_{RAD,\theta}(\underline{r}) = -j\eta\frac{\exp(-jkr)}{2\lambda r}\left(N_x(\theta,\phi)\cos\theta\cos\phi + N_y(\theta,\phi)\cos\theta\sin\phi\right) \\ \underline{E}_{RAD,\phi}(\underline{r}) = -j\eta\frac{\exp(-jkr)}{2\lambda r}\left(-N_x(\theta,\phi)\sin\phi + N_y(\theta,\phi)\cos\phi\right) \end{cases} \tag{2.12}$$

The equations (2.12) and (2.10) completely describe the far-field radiation of an induced current from a feeder on the reflectarray surface. In order to make possible the utilization of these equation and the problem definition we need to discretize the reflectarray surface.

2.2 Discretization of the reflectarray surface

Lets assume to discretize the reflectarray surface in a regular lattice, and each cell of the lattice includes only one reflectarray element. Thus, the reflectarray consists of a grid of $M \times N$ elements with unit cells of size $\Delta x \times \Delta y$ and in order to discretize (2.10) we will apply a pixel-basis function $\mathcal{P}$ centered at $\mathbf{r}^{mn} \triangleq \left[\left(m - \frac{M}{2}\right)\Delta x,\ \left(n - \frac{N}{2}\right)\Delta y,\ 0\right]$, $m = 1, ..., M$, $n = 1, ..., N$ to the current distribution and we obtain:

$$J_q(\mathbf{r}) \triangleq \sum_{m=1}^{M}\sum_{n=1}^{N} J_q^{mn}\mathcal{P}^{mn}(\mathbf{r}) \qquad q \in \{x, y\} \tag{2.13}$$

In particular, the x-component of the current can be expressed as:

$$\begin{aligned} J_x|_{mn} = \ & -\tfrac{\nu_x^{\text{inc}}(\mathbf{r}^{mn})\sin(\theta)}{\eta}\Big[\left(1 + S_{\theta\theta}(\mathbf{r}^{mn})\right)E_{inc}^{\theta}(\mathbf{r}^{mn}) + \\ & + S_{\theta\phi}(\mathbf{r}^{mn})\,E_{inc}^{\phi}(\mathbf{r}^{mn})\Big] + \\ & -\tfrac{\nu_z^{inc}(\mathbf{r}^{mn})\cos(\theta)\cos(\phi)}{\eta}\Big[\left(1 - S_{\theta\theta}(\mathbf{r}^{mn})\right)E_{inc}^{\theta}(\mathbf{r}^{mn}) + \\ & - S_{\theta\phi}(\mathbf{r}^{mn})\,E_{inc}^{\phi}(\mathbf{r}^{mn})\Big] + \\ & + \tfrac{\nu_z^{inc}(\mathbf{r}^{mn})\sin(\phi)}{\eta}\Big[\left(1 - S_{\phi\theta}(\mathbf{r}^{mn})\right)E_{inc}^{\theta}(\mathbf{r}^{mn}) + \\ & - S_{\phi\phi}(\mathbf{r}^{mn})\,E_{inc}^{\phi}(\mathbf{r}^{mn})\Big] \end{aligned} \tag{2.14}$$

and the y-component as:

$$\begin{aligned} J_y|_{mn} = \ & -\tfrac{\nu_y^{\text{inc}}(\mathbf{r}^{mn})\sin(\theta)}{\eta}\Big[\left(1 + S_{\theta\theta}(\mathbf{r}^{mn})\right)E_{inc}^{\theta}(\mathbf{r}^{mn}) + \\ & + S_{\theta\phi}(\mathbf{r}^{mn})\,E_{inc}^{\phi}(\mathbf{r}^{mn})\Big] + \\ & + \tfrac{\nu_z^{inc}(\mathbf{r}^{mn})\cos(\theta)\sin(\phi)}{\eta}\Big[\left(1 - S_{\theta\theta}(\mathbf{r}^{mn})\right)E_{inc}^{\theta}(\mathbf{r}^{mn}) + \\ & - S_{\theta\phi}(\mathbf{r}^{mn})\,E_{inc}^{\phi}(\mathbf{r}^{mn})\Big] + \\ & + \tfrac{\nu_z^{inc}(\mathbf{r}^{mn})\cos(\phi)}{\eta}\Big[\left(1 - S_{\phi\theta}(\mathbf{r}^{mn})\right)E_{inc}^{\theta}(\mathbf{r}^{mn}) + \\ & - S_{\phi\phi}(\mathbf{r}^{mn})\,E_{inc}^{\phi}(\mathbf{r}^{mn})\Big] \end{aligned} \tag{2.15}$$

where the reflection matrix of the ground plane is substituted by 1 since it is perfectly reflecting, while the component z is obviously null ($J_z|_{mn} = 0$, $m = 1, ..., M$ and $n = 1, ..., N$).

Substituting (2.13) in (2.10):

$$\begin{array}{rl} N_q(\theta,\varphi) = & \sum_{m=1}^{M}\sum_{n=1}^{N}\exp\left[jk\hat{r}\mathbf{r}^{mn}\right]J_q^{mn}\times \\ & \int_{\Omega_{mn}}\mathcal{P}^{mn}(\mathbf{r})\exp\left[jk\hat{r}\mathbf{r}^{\Omega_{mn}}\right]\mathrm{d}\Omega_{mn} \quad q\in\{x,y\} \end{array} \tag{2.16}$$

where Ω_{mn} is the area of the mn-th rectangular pixel. Due to the presence of the pixel-basis function the integral in the radiation vector formula becomes:

$$\int_{x_n-\frac{\Delta x}{2}}^{x_n+\frac{\Delta x}{2}}\int_{y_m-\frac{\Delta y}{2}}^{y_m+\frac{\Delta y}{2}}\exp\left[j\frac{2\pi}{\lambda}x\sin\theta\cos\phi\right]\exp\left[j\frac{2\pi}{\lambda}y\sin\theta\sin\phi\right]\mathrm{dx}\,\mathrm{dy} \tag{2.17}$$

where (x_n, y_m) is the center of the mn-th reflectarray element/rectangular pixel. Moreover, with some simple step can be proven that this integral can be solved as:

$$\begin{array}{l} \exp\left[j\frac{2\pi}{\lambda}x\sin\theta\cos\phi\right]\exp\left[j\frac{2\pi}{\lambda}y\sin\theta\sin\phi\right]\times \\ \frac{4}{\Delta x\Delta y}\mathrm{sinc}\left(\frac{k\Delta x}{2}\sin\theta\cos\phi\right)\mathrm{sinc}\left(\frac{k\Delta y}{2}\sin\theta\sin\phi\right) \end{array} \tag{2.18}$$

Now substituting the integral solution (2.18) in (2.16) we finally have:

$$\begin{array}{rl} N_q(\theta,\varphi) = & \frac{4}{\Delta x\Delta y}\mathrm{sinc}\left(\frac{k\Delta x}{2}\sin\theta\cos\phi\right)\mathrm{sinc}\left(\frac{k\Delta y}{2}\sin\theta\sin\phi\right)\times \\ & \sum_{m=1}^{M}\sum_{n=1}^{N}J_q^{mn}\exp\left[jk\left(x_n\sin\theta\cos\phi+y_m\sin\theta\sin\phi\right)\right] \end{array} \tag{2.19}$$

This final equation is important because it describes, in a discretized way, the radiation vectors and thus we can compute the far-field having a non continuous current definition.

The usual way to describe the far-field pattern in reflectarray antenna system is using the third Ludwig definition [78][6][81] of the coordinate system.

The far field radiated by a reflectarray displaced on a surface Ω (Fig. 2.1) can be modeled as [68]

$$\mathbf{E}(\mathbf{r}) \approx \frac{j\mu f}{2}\frac{\exp(-jkr)}{r}\left[F_{CO}(\theta,\varphi)\,\widehat{\mathbf{p}}_{CO}+F_{CX}(\theta,\varphi)\,\widehat{\mathbf{p}}_{CX}\right] \tag{2.20}$$

where $r=|\mathbf{r}|$, $\mathbf{r}=(r\sin\theta\cos\varphi,\, r\sin\theta\sin\varphi,\, r\cos\theta)$ is the position vector, and the co-polar $\widehat{\mathbf{p}}_{CO}$ and cross-polar $\widehat{\mathbf{p}}_{CX}$ unit vectors agree with the third definition of Ludwig [78][6][81](Fig. 2.2)

$$\begin{cases} \widehat{\mathbf{p}}_{CO} = \cos(\varphi)\,\widehat{\boldsymbol{\theta}} - \sin(\varphi)\,\widehat{\boldsymbol{\varphi}} \\ \widehat{\mathbf{p}}_{CX} = \sin(\varphi)\,\widehat{\boldsymbol{\theta}} + \cos(\varphi)\,\widehat{\boldsymbol{\varphi}} \end{cases} \tag{2.21}$$

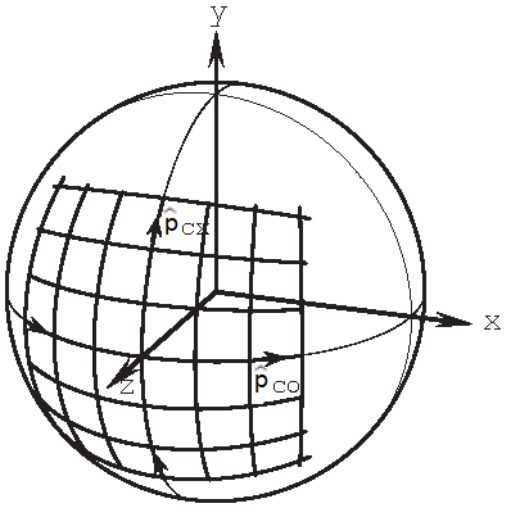

Figure 2.2: Co-polar and cross-polar unit vector following the Ludwig third definition.

with some manipulation the co-polar and cross-polar pattern can be retrieved from (2.20) and (2.12):

$$\begin{aligned} F_{CO}(\theta,\varphi) = \quad & \left\{1+\cos^2(\varphi)\left[1-\cos(\theta)\right]\right\} N_x(\theta,\varphi) + \\ & + \left[\cos(\theta)-1\right]\sin(\varphi)\cos(\varphi)\, N_y(\theta,\varphi) + \\ & - \sin(\theta)\cos(\varphi)\, N_z(\theta,\varphi) \end{aligned} \tag{2.22}$$

$$\begin{aligned} F_{CX}(\theta,\varphi) = \quad & \left[\cos(\theta)-1\right]\sin(\varphi)\cos(\varphi)\, N_x(\theta,\varphi) + \\ & + \left\{1+\sin^2(\varphi)\left[1-\cos(\theta)\right]\right\} N_y(\theta,\varphi) + \\ & - \sin(\theta)\sin(\varphi)\, N_z(\theta,\varphi) \end{aligned} \tag{2.23}$$

At this point we have defined how to compute the reference pattern in the standard components we can move to the synthesis problem definition. Since there are many works in the literature that deal with the problem to find a proper technology (e.g. printed patches type, number of layers, all-metal structures, etc...)[2],[6],[15],[59],[62]-[66] to obtain the wanted value of the scattering matrix **S** for a given current distribution, now we do not take this step into account (step (b)) and we will continue handling only the problem related to the surface current definition when *feasibility constraints* are present (e.g. *forbidden region*).

2.3 Inverse Source problem definition

According to the previous formulation, the synthesis of the constrained surface currents of a reflectarray with desired far-field shaped-beam pattern

$$\mathbf{E}^{ref}(\mathbf{r}) \triangleq \frac{j\mu f}{2}\frac{\exp(-jkr)}{r}\left[F_{CO}^{ref}(\theta,\varphi)\,\widehat{\mathbf{p}}_{CO} + F_{CX}^{ref}(\theta,\varphi)\,\widehat{\mathbf{p}}_{CX}\right] \tag{2.24}$$

can be formulated as an *inverse source* problem.

The inverse source problem is defined as:

> *Constraint-Geometry Reflectarray-Currents Synthesis* problem (*CG-RCS*) and its definition is:
>
> Find the surface current $\underline{J}(\underline{r})$ (or its numerical counterpart $\mathbf{J}_q \triangleq \left\{J_q^{mn};\ m=1,...,M,\ n=1,...,N\right\}$, $q \in \{x,y\}$), whose radiate a far-field, $\underline{E}$, whose associated co-polar and cross-polar component, fit the following reference pattern *matching condition:*
>
> $$\begin{cases} F_{CO}^{ref}(\theta,\varphi) = F_{CO}(\theta,\varphi) \\ F_{CX}^{ref}(\theta,\varphi) = F_{CX}(\theta,\varphi) \end{cases} \tag{2.25}$$
>
> having that $\mathbf{J}_q \in \mathcal{S}_q$, $q \in \{x,y\}$.Where $\mathcal{S}_q$, $q \in \{x,y\}$, are the *feasibility sets*, which account for the constraints provided by the end-user/designer (i.e., the presence of *forbidden regions* in the aperture).

For example, if Φ identifies the arbitrary-shaped user-defined 2-D *forbidden region* (within the reflectarray $\Phi \in \Omega$), the feasibility condition state that $\underline{J}(\underline{r}) = \underline{0}$ if $\underline{r} \in \Phi$(i.e.: in numerical form: $J_q^{mn} = 0$, $q = \{x,y\}$, if $\mathbf{r}^{mn} \in \Phi$). It is worth remarking that many techniques can be adopted for the synthesis of feed and associated reflectarray elements (step (b)) (depending on the selected unit-cell geometry [2],[6],[15],[59],[62]-[66]) once $\mathbf{J}_q$, $q \in \{x,y\}$, has been found by solving the above problem.

Chapter 3

Non-Measurable Currents-based Solution Method

In this chapter the solution method, that solve the *Inverse Source* problem, is explained. In particular, after some mathematical computation needed to obtain a matrix formulation of the problem, it is applied a Truncated Singular Value Decomposition (*T-SVD*) in order to obtain the *minimum-norm* solution. This solution can radiate the desired field but can not deal with *feasibility constraint* (e.g. *forbidden region*). In order to overcome this problem, it is proposed to superimpose the *non-radiating/non-measurable* currents, that are derived from the *T-SVD*, to the *minimum-norm* solution. Moreover, given the definition of the handled *feasibility constraint* (i.e. *forbidden region*), the closed-form formulation to solve the problem is defined.

3.1 Field discretization

In order to address the *CG-RCS* problem, taking in consideration that the z-component of the current is not present, its discretized version is firstly computed by substituting (2.22) and (2.23), in (2.25), sampling it in a set of L angles (θ_l, φ_l), $l = 1, ..., L$ as follows

$$\begin{cases} F_{CO}^{ref}(\theta_l, \varphi_l) = \{1 + \cos^2(\varphi_l)[1 - \cos(\theta_l)]\} N_x(\theta_l, \varphi_l) + \\ \qquad + [\cos(\theta_l) - 1] \sin(\varphi_l) \cos(\varphi_l) N_y(\theta_l, \varphi_l) \\ F_{CX}^{ref}(\theta_l, \varphi_l) = [\cos(\theta_l) - 1] \sin(\varphi_l) \cos(\varphi_l) N_x(\theta_l, \varphi_l) + \\ \qquad + \left\{1 + \sin^2(\varphi_l)[1 - \cos(\theta_l)]\right\} N_y(\theta_l, \varphi_l) \\ \qquad\qquad\qquad\qquad\qquad\qquad\qquad\qquad l = 1, ..., L \end{cases} \tag{3.1}$$

which, by exploiting (2.19), can be rewritten as

$$\begin{cases} F_{CO}^{ref}(\theta_l, \varphi_l) = & \Gamma(\theta_l, \varphi_l) (\{1 + \cos^2(\varphi_l)[1 - \cos(\theta_l)]\} \\ & \times \sum_{m=1}^{M} \sum_{n=1}^{N} J_x^{mn} e^{mn}(\theta_l, \varphi_l) + \\ & + [\cos(\theta_l) - 1] \sin(\varphi_l) \cos(\varphi_l) \\ & \times \sum_{m=1}^{M} \sum_{n=1}^{N} J_y^{mn} e^{mn}(\theta_l, \varphi_l)\Big) \\ F_{CO}^{ref}(\theta_l, \varphi_l) = & \Gamma(\theta_l, \varphi_l) ([\cos(\theta_l) - 1] \sin(\varphi_l) \cos(\varphi_l) \\ & \times \sum_{m=1}^{M} \sum_{n=1}^{N} J_x^{mn} e^{mn}(\theta_l, \varphi_l) + \\ & + \left\{1 + \sin^2(\varphi_l)[1 - \cos(\theta_l)]\right\} \\ & \times \sum_{m=1}^{M} \sum_{n=1}^{N} J_y^{mn} e^{mn}(\theta_l, \varphi_l)\Big) \\ & \qquad\qquad\qquad\qquad l = 1, ..., L \end{cases} \tag{3.2}$$

where, for easy of compactness:

$$e^{mn}(\theta_l, \varphi_l) \triangleq \exp[jk_0 (m\Delta x \sin\theta_l \cos\varphi_l + n\Delta y \sin\theta_l \sin\varphi_l)] \tag{3.3}$$

and

$$\Gamma(\theta_l, \varphi_l) = \frac{4}{\Delta x \Delta y} \text{sinc}\left(\frac{k\Delta x}{2} \sin\theta \cos\phi\right) \text{sinc}\left(\frac{k\Delta y}{2} \sin\theta \sin\phi\right) \tag{3.4}$$

In order to further simplify the notation and to better handle the problem we need to express the equation in matrix form.

In this way equation (3.2) can be re-organized in a more compact form as the

following matrix equation

$$\mathbf{F}^{ref} = \mathcal{G}\mathbf{J} \tag{3.5}$$

where $\mathbf{F}^{ref} \triangleq \left[\mathbf{F}_{CO}^{ref},\, \mathbf{F}_{CX}^{ref}\right]^T$, $\mathbf{F}_t^{ref} = \left\{F_t^{ref}\left(\theta_l, \varphi_l\right),\, l = 1, ..., L\right\}$, $t \in \{CO,\, CX\}$, $\mathbf{J} \triangleq [\mathbf{J}_x,\, \mathbf{J}_y]^T$, and:

$$\mathcal{G} \triangleq \begin{bmatrix} \mathcal{G}_{CO,x} & \mathcal{G}_{CO,y} \\ \mathcal{G}_{CX,x} & \mathcal{G}_{CX,y} \end{bmatrix} \tag{3.6}$$

is the $(2 \times L) \times (2 \times P)$ overall Green matrix ($\cdot^T$ being the transpose operator) featuring the sub-matrices:

$$\begin{aligned} &\mathcal{G}_{CO,x} \triangleq \left\{\Gamma\left(\theta_l, \varphi_l\right) e^{mn}\left(\theta_l, \varphi_l\right)\left\{1 + \cos^2\left(\varphi_l\right)\left[1 - \cos\left(\theta_l\right)\right]\right\}\right. \\ &\mathcal{G}_{CO,y} = \mathcal{G}_{CX,x} \triangleq \left\{\Gamma\left(\theta_l, \varphi_l\right) e^{mn}\left(\theta_l, \varphi_l\right)\left[\cos\left(\theta_l\right) - 1\right]\sin\left(\varphi_l\right)\cos\left(\varphi_l\right)\right. \\ &\mathcal{G}_{CX,y} \triangleq \left\{\Gamma\left(\theta_l, \varphi_l\right) e^{mn}\left(\theta_l, \varphi_l\right)\left\{1 + \sin^2\left(\varphi_l\right)\left[1 - \cos\left(\theta_l\right)\right]\right\}\right. \\ &m = 1, ..., M,\ n = 1, ..., N,\ l = 1, ..., L \end{aligned} \tag{3.7}$$

where Γ was defined in (3.4) and e^{mn} in (3.3).

Now we have all the formulation ready for start tacking the *Inverse Source* problem.

The problem to retrieve a current distribution from a field is well-known to be ill-posed. This means that multiple current distribution can radiate the same field. In the literature, one of the most used tool to obtain a minimum-norm (or generalized) solution of the system is the regularization and inversion technique Truncated Singular Value Decomposition. Using this algorithm the obtained solution is the ones that best represents the radiated field with the smallest norm.

3.2 Truncated Singular Value Decomposition

In order to compute the minimum norm solution is well-known the procedure based on the truncated version of the Singular Value Decomposition (SVD)[73]-[77].

We assume that the number of the reflectarray elements ($2 \times P = 2 \times M \times N$) is less than the number of field samples ($2 \times L$). Given that ψ_1^2, ψ_2^2, ..., ψ_W^2 ($W \triangleq \min\{2 \times L, 2 \times P\}$) are the positive eigenvalues of symmetric matrix $\mathcal{G}^*\mathcal{G}$ (where * indicate the conjugate transpose) and $\mathbf{c}_1, \mathbf{c}_2$, ..., $\mathbf{c}_{2\times P}$ the corresponding orthonormal eigenvectors:

$$\begin{aligned} \mathcal{G}^*\mathcal{G}\mathbf{c}_j = \psi_j^2\mathbf{c}_j \qquad & \mathbf{c}_j^*\mathbf{c}_k = \delta_{jk} \\ & j,k = 1, ..., 2 \times L \end{aligned} \tag{3.8}$$

being:

$$\psi_j \mathbf{b}_j = \mathcal{G}\mathbf{c}_j \quad j = 1, ..., 2 \times L \tag{3.9}$$

substituting (3.8) in (3.9) it can be obtained:

$$\mathcal{G}^*\mathbf{b}_j = \psi_j \mathbf{c}_j \quad j = 1, ..., 2 \times L \tag{3.10}$$

multiplying left and right side of (3.10) for $\mathcal{G}$ and thanks to (3.9) immediately follow that:

$$\begin{aligned} \mathcal{G}\mathcal{G}^*\mathbf{b}_j = \psi_j^2 \qquad & \mathbf{b}_j^*\mathbf{b}_j = \delta_{jk} \\ & j,k = 1, ..., 2 \times L \end{aligned} \tag{3.11}$$

Equations (3.10) and (3.11) shown the orthonormal properties of the two matrices $\mathbf{B}$ and $\mathbf{C}$.

In matrix notation (3.9) can be written as:

$$\mathcal{G} = \mathbf{B}\Psi\mathbf{C}^* \tag{3.12}$$

can be noticed that Ψ is a diagonal matrix in the form:

$$\Psi = \begin{bmatrix} \psi_1 & & & 0 \\ & \ddots & & \\ & & \ddots & \\ 0 & & & \psi_W \end{bmatrix}_{W \times W} \tag{3.13}$$

another note is that the singular values are ordered in descending order (i.e., $\psi_w \geq \psi_{w+1}$, $w = 1, ..., W-1$).

Writing now the *minimum-norm* current as a weighted sum as:

$$\mathbf{J}^{\mathcal{MN}} = \mathbf{C}\boldsymbol{\gamma} \qquad \textit{with} \qquad \boldsymbol{\gamma} = \begin{bmatrix} \gamma_1 \\ \vdots \\ \vdots \\ \gamma_W \end{bmatrix} \tag{3.14}$$

from (3.9) we can obtain that:

$$\gamma_j \psi_j \mathbf{b}_j = \gamma_j \mathcal{G} \mathbf{c}_j \quad j = 1, \ldots, W \tag{3.15}$$

and using the ration expressed in (3.5):

$$\mathbf{F}^{ref} = \sum_{j=1}^{W} \gamma_j \psi_j \mathbf{b}_j \tag{3.16}$$

Since $\psi_i \mathbf{b}_j = 0$ for $j > W$, it is simply to derive that only the first W $\mathbf{c}_w$ bases that are used to describe $\mathbf{J}^{\mathcal{MN}}$ are measurable.

For these bases the coefficients γ_j are given using:

$$\gamma_j = \psi_j^{-1} \left\{ \mathbf{b}_j^* \mathbf{F}^{ref} \right\} \qquad j = 1, ..., W \tag{3.17}$$

and substituting (3.17) in (3.14):

$$\mathbf{J}^{\mathcal{MN}} = \sum_{j=1}^{W} \psi_j^{-1} \left\{ \mathbf{b}_j^* \mathbf{F}^{ref} \right\} \mathbf{c}_j \tag{3.18}$$

we obtain the *minimum-norm* (or generalized) solution.

Dually in matrix form (3.18) became:

$$\mathbf{J}^{\mathcal{MN}} = \mathbf{C}\Psi^{-1}\mathbf{B}^{*}\mathbf{F}^{ref} \tag{3.19}$$

This resulting problem is well-known [74]-[77] to be not well-posed due to the ill-conditioning of the $\mathcal{G}$ matrix.

The solution instability occurs due to the fact that some singular values ψ are much lower in magnitude with respect to the first one (ψ_1). This problem can be measured by using the *condition number* that is defined as:

$$d = \frac{\psi_1}{\psi_W} \tag{3.20}$$

This value measures the instability of the problem. In fact as higher is the value, as higher is the instability, and this means that the a small variation in the $\mathbf{F}^{ref}$ generate a great variation in $\mathbf{J}^{\mathcal{MN}}$.

In literature this problem is well-known [74]-[77] and the solution is to use a *truncated* version of the *SVD*.

It is defined H as the *truncation order*, and is computed as:

$$H \triangleq \arg\left\{\min_{w}\left|\frac{\psi_w}{\psi_1} - \tau\right|\right\} \quad s.t.\ \frac{\psi_w}{\psi_1} \geq \tau \tag{3.21}$$

where τ being the associated user-defined *SVD* truncation threshold. The threshold τ, the truncation order H and an example of singular value behavior ψ are shown in Fig. 3.1. By selecting the value of the *SVD* truncation threshold τ the user implicitly defines the precision on the reproduction the far-field and the instability of the current, thus lower value of the threshold means better reproduction of the far-field but also higher variation in the solution (e.g. current distribution with high space variations).

Then, are computed the truncated version of matrices $\mathbf{C}$, $\mathbf{B}$ and Ψ by selecting the first H bases of the corresponding sets:

$$\begin{aligned} \mathbf{B}_\tau &= \{\mathbf{b}_h,\ h = 1, ..., H\} \\ \mathbf{C}_\tau &= \{\mathbf{c}_h,\ h = 1, ..., H\} \\ \Psi_\tau &= diag\,(\psi_h,\ h = 1, ..., H) \end{aligned} \tag{3.22}$$

By substituting (3.22) in (3.19), the *minimum-norm* component can be defined

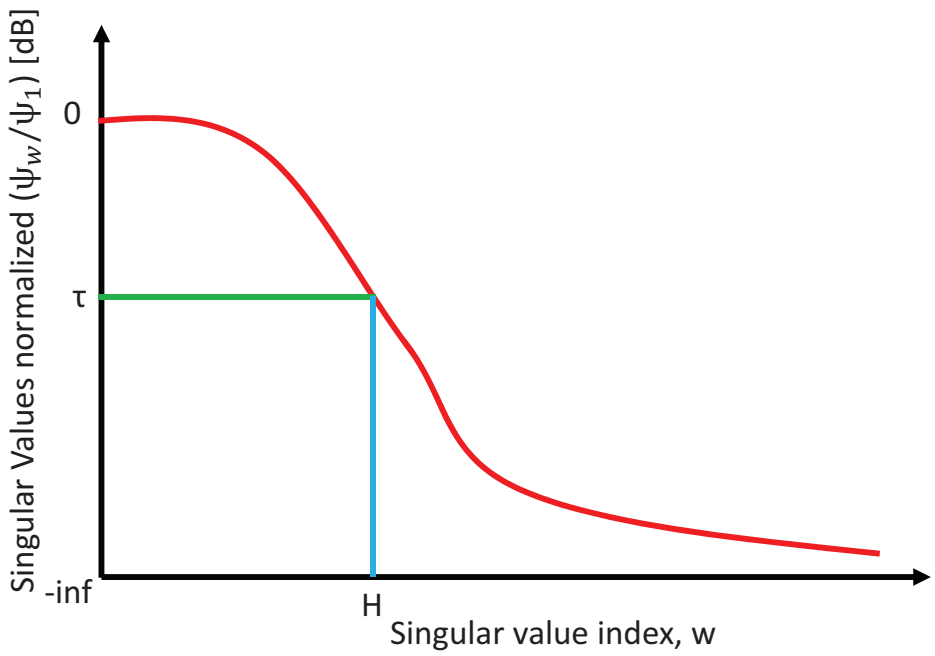

Figure 3.1: Example of singular values distribution ψ_w, $w = 1, ..., W$, taking into account a truncation order H and a truncation threshold τ.

as:

$$\mathbf{J}^{\mathcal{MN}} \triangleq \mathbf{C}_\tau \Psi_\tau^{-1} \mathbf{B}_\tau^* \mathbf{F}^{ref} \tag{3.23}$$

This kind of solution (*minimum-norm*) can be achieved also in other ways (not only *T-SVD*), however the truncation operation on the SVD give us a set of bases that will radiate a null field outside of the support and thus, each basis can be interpreted as a different current with different shape that do not radiate any field (or at least a field that is not measurable).

3.3 Synthesis approach

Now we have a solution that can radiate the wanted field with an error that can be controlled using the threshold τ.

The solution of the *CG-RCS* can be carried out by inverting (3.5) subject to $\mathbf{J} \in \mathcal{S}$ ($\mathcal{S} \triangleq \{\mathcal{S}_q,\, q \in \{x, y\}\}$). Such an *inverse source* problem is known to be ill-posed because of the non-uniqueness of the solution (owing to the existence of non-radiating/non-measurable currents) [74]-[76]. While such a feature can be an issue in microwave imaging and antenna diagnosis applications [74]-[76], it can be actually employed as a *DoF* in the framework of reflectarray current synthesis. Thanks to such a *DoF*, the following innovative two-step procedure is introduced to solve (3.5):

- the *radiating* currents [i.e., $\mathbf{J}^{\mathcal{MN}}$] are firstly computed (*Step A*) as the minimum-norm solution of (3.5);

- the *non-radiating/non-measurable* currents $\mathbf{J}^{\mathcal{NR}}$ are then designed (*Step B*) so that the overall solution of (3.5)

$$\mathbf{J} \triangleq \mathbf{J}^{\mathcal{MN}} + \mathbf{J}^{\mathcal{NR}} \tag{3.24}$$

  complies with $\mathbf{J} \in \mathcal{S}$.

While we have already explain how to obtain the radiating part of the total current $\mathbf{J}^{\mathcal{MN}}$, the *Step B* is not mathematically explicated.

3.4 Non-measurable/Non-radiating definition

The outlined *SVD* procedure in Sect. 3.2 on $\mathcal{G}$ is also the starting point for the solution of *Step B*. In fact, it is known from inverse source theory [74]-[76] that $\mathbf{J}^{\mathcal{NR}}$ can be expressed as a linear combination of the the last $2 \times P - H$ right singular vectors of $\mathbf{C}$ (i.e., $\mathbf{C}^{\mathcal{NR}} \triangleq \{\mathbf{c}_h,\, h = H+1, ..., 2 \times P\}$) as follows

$$\mathbf{J}^{\mathcal{NR}} \triangleq \mathbf{C}^{\mathcal{NR}} \boldsymbol{\alpha} \tag{3.25}$$

where $\boldsymbol{\alpha} \triangleq \{\alpha_h;\, h = H+1, ..., 2 \times P\}$ are the arbitrary $2 \times P - H$ coefficients (i.e., the *DoF*s) associated to the non-radiating/non-measurable current basis $\mathbf{C}^{\mathcal{NR}}$.

It is highlighted that the matrices $\mathbf{C}$ and $\mathbf{B}$ obtained in (3.12) are subdivided as:

$$\begin{aligned}
\mathbf{C} &= \left[\mathbf{C}_\tau | \mathbf{C}^{\mathcal{NR}}\right] = \left[\begin{array}{ccc|ccc} c_{1,1} & \cdots & c_{1,H} & c_{1,H+1} & \cdots & c_{1,2\times P} \\ \vdots & \ddots & \vdots & \vdots & \ddots & \vdots \\ c_{2\times P,1} & \cdots & c_{2\times P,H} & c_{2\times P,H+1} & \cdots & c_{2\times P,2\times P} \end{array}\right] \\
\mathbf{B} &= \left[\mathbf{B}_\tau | \mathbf{B}^{\mathcal{NR}}\right] = \left[\begin{array}{ccc|ccc} b_{1,1} & \cdots & b_{1,H} & b_{1,H+1} & \cdots & b_{1,2\times L} \\ \vdots & \ddots & \vdots & \vdots & \ddots & \vdots \\ b_{2\times L,1} & \cdots & b_{2\times L,H} & b_{2\times L,H+1} & \cdots & b_{2\times L,2\times L} \end{array}\right]
\end{aligned} \tag{3.26}$$

This means that by selecting the proper value of $\boldsymbol{\alpha}$ the designer can define a wanted current distribution that do not radiate any field (or at least is not measurable) that can be added to the radiating current ($\mathbf{J}^{\mathcal{MN}}$) to fulfill some constraints in the design procedure. In this work the feasibility constraint is proposed to be the "forbidden region" constraint, that is highlighted in the next section.

3.5 Forbidden region constraint definition

Using (3.23) and (3.25) in (3.24), *Step B* can be then addressed by finding $\boldsymbol{\alpha}$ such that

$$\left(\mathbf{C}_\tau \Psi_\tau^{-1} \mathbf{B}_\tau^* \mathbf{F}^{ref} + \mathbf{C}^{\mathcal{NR}} \boldsymbol{\alpha}\right) \in \mathcal{S} \tag{3.27}$$

The actual procedure to find $\boldsymbol{\alpha}$ in (3.27) depends on the definition of $\mathcal{S}$. Since in this work the design constraint is represented by the presence of user-defined forbidden areas in Ω (where no reflectarray elements are allowed), the following mathematical definition is adopted

$$\mathcal{S} \triangleq \left\{ J_q^{mn} = 0 \quad \text{if } \mathbf{r}^{mn} \in \Phi;\, q \in \{x, y\} \right\} \tag{3.28}$$

where Φ identifies the arbitrary-shaped 2D *forbidden region* and it is composed by K reflectarray unit cells (i.e., corresponding to $2 \times K$ constraints since the K equations are enforced separately on $\mathbf{J}_x$ and on $\mathbf{J}_y$), and can be seen in Fig. 3.2.

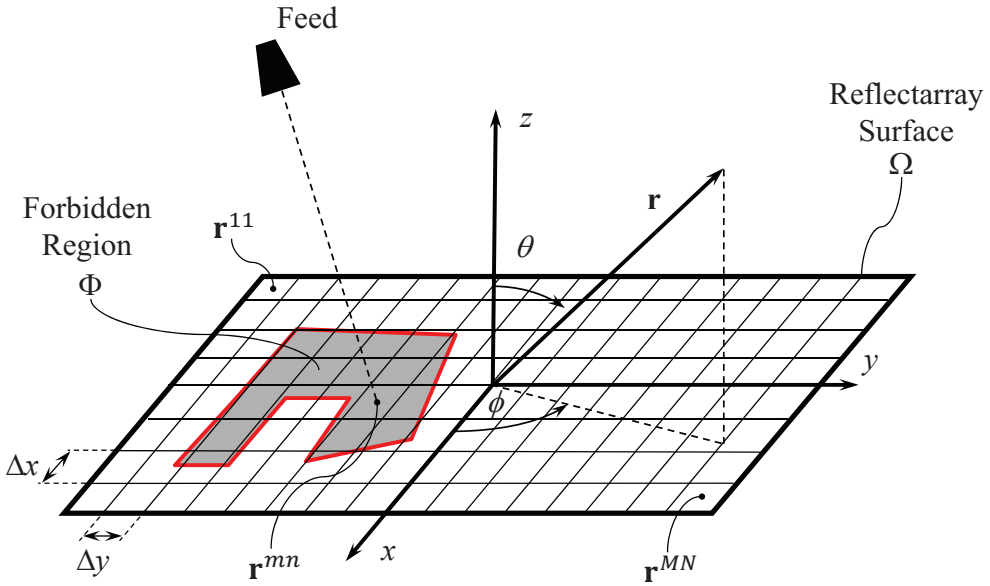

Figure 3.2: Geometry of the reflectarray antenna.

By using (3.28), (3.27) can be rewritten as the following set of $2 \times K$ linear equations in $2 \times P - H$ unknowns

$$\left[\mathcal{D}_\Phi \left(\mathbf{C}_\tau \Psi_\tau^{-1} \mathbf{B}_\tau^* \mathbf{F}^{ref}\right)\right] + \left[\mathcal{D}_\Phi \left(\mathbf{C}^{\mathcal{NR}}\right)\right] \boldsymbol{\alpha} = \mathbf{0}_{2K} \tag{3.29}$$

where $\mathbf{0}_{2K}$ is a null-vector of size $2 \times K$, and $\mathcal{D}_\Phi(\cdot)$ is an operator which extracts a sub-matrix comprising the $2 \times K$ rows corresponding to the mn-indexes for which $\mathbf{r}^{mn} \in \Phi$. The matrix problem (3.29) can be re-arranged as:

$$\left[\mathcal{D}_\Phi\left(\mathbf{C}^{\mathcal{NR}}\right)\right]\boldsymbol{\alpha} = -\left[\mathcal{D}_\Phi\left(\mathbf{C}_\tau \Psi_\tau^{-1} \mathbf{B}_\tau^* \mathbf{F}^{ref}\right)\right] \tag{3.30}$$

and (3.30) according to linear system theory, has at least one solution if the following *solvability condition* is satisfied

$$2 \times K \leq 2 \times P - H \tag{3.31}$$

(i.e., the number of constraints is equal or lower than the number of DoFs in the linear problem).

Moreover, since $\mathcal{D}_\Phi\left(\mathbf{C}^{\mathcal{NR}}\right)$ is always full-rank (because the right singular vectors composing $\mathbf{C}^{\mathcal{NR}}$ are orthonormal by definition [74][75]), (3.30) has actually ∞^Q different solutions ($Q \triangleq 2 \times P - H - 2 \times K$) if (3.31) holds true. Consequently, under the assumption (3.31) and without loss of generality, a unique solution to (3.30) can be found by setting

$$\boldsymbol{\alpha} = \left[\widetilde{\boldsymbol{\alpha}};\, \mathbf{0}_Q\right]^T \tag{3.32}$$

where

$$\widetilde{\boldsymbol{\alpha}} = -\left[\widetilde{\mathcal{D}}_\Phi\left(\mathbf{C}^{\mathcal{NR}}\right)\right]^{-1}\left[\mathcal{D}_\Phi\left(\mathbf{C}_\tau \Psi_\tau^{-1} \mathbf{B}_\tau^* \mathbf{F}^{ref}\right)\right] \tag{3.33}$$

is the reduced coefficient vector which contains only the first $2 \times K$ entries of $\boldsymbol{\alpha}$, and $\widetilde{\mathcal{D}}_\Phi\left(\mathbf{C}^{\mathcal{NR}}\right)$ is the reduced version of $\mathcal{D}_\Phi\left(\mathbf{C}^{\mathcal{NR}}\right)$ which contains only its first $2 \times K$ columns.

3.6 Final closed-form formulation

The solution to the *CG-RCS* is finally obtained by combining (3.33), (3.32), (3.25), and (3.23) in (3.24) to obtain the closed-form expression

$$\begin{aligned}\mathbf{J} = \; & \mathbf{C}_\tau \Psi_\tau^{-1} \mathbf{B}_\tau^* \mathbf{F}^{ref} + \\ & + \mathbf{C}^{\mathcal{NR}} \left[- \left[\widetilde{\mathcal{D}}_\Phi \left(\mathbf{C}^{\mathcal{NR}} \right) \right]^{-1} \left[\mathcal{D}_\Phi \left(\mathbf{C}_\tau \Psi_\tau^{-1} \mathbf{B}_\tau^* \mathbf{F}^{ref} \right) \right] ; \mathbf{0}_Q \right]^T \end{aligned} \tag{3.34}$$

which can be easily demonstrated to comply with (3.5) by substitution.

As regards the closed-form solution (3.34), it is worthwhile to notice that:

- the deduced methodology enables the computation of the reflectarray surface currents without requiring any iterative local/global optimization procedure and satisfying both the radiation (3.5) and the geometrical requirements (3.28) by definition;

- such an expression is derived as a proof-of-concept to demonstrate the possibility to employ non-radiating currents as a *DoF* in reflectarray design. However, other solutions [among the ∞^Q available in (3.30)] may be selected to comply with other geometry/antenna requirements and guidelines;

- analogously, other definitions of $\mathcal{S}$ (out of the scope of the current manuscript) could be seamlessly taken into account within the same framework to encode different design objectives instead of (3.28);

- the design process only requires the user to specify the desired far-field copolar and cross-polar patterns (i.e., $\mathbf{F}$), the reflectarray aperture and unit cell size (i.e., $M \times N$ and $\Delta x \times \Delta y$), the forbidden region (i.e., Φ), and the *SVD* threshold value τ.

With reference to this last parameter, while the choice of τ in (3.21) can be challenging in microwave imaging [74], its definition in the reflectarray source synthesis problem only requires that the magnitude of the truncated singular

values (i.e., ψ_h, $h = H+1, ..., W$) is small enough to guarantee that

$$\mathcal{G}\left\{\mathbf{C}^{\mathcal{NR}}\left[-\left[\widetilde{\mathcal{D}}_{\Phi}\left(\mathbf{C}^{\mathcal{NR}}\right)\right]^{-1}\left[\mathcal{D}_{\Phi}\left(\mathbf{C}_{\tau}\Psi_{\tau}^{-1}\mathbf{B}_{\tau}^{*}\mathbf{F}\right)\right];\mathbf{0}_{Q}\right]^{T}\right\} \ll \mathbf{F}^{ref} \tag{3.35}$$

(i.e., the residual *non-measurable* field caused by $\mathbf{J}^{\mathcal{NR}}$ is actually negligible with respect to the far-field pattern $\mathbf{F}^{ref}$). Owing to the closed-form nature of (3.35), τ can be then easily chosen in the design phase by the analysis of the singular value distribution Ψ (Sect. 4).

Chapter 4

Method Assessment

In this chapter it is highlighted the numerical assessment of the proposed design strategy. At the beginning is presented also an error metric that takes into account the difference between the reference field and the field radiated by the synthesized current. Then it is shown a step-by-step procedure that illustrate the synthesis procedure and then some example with different shape/dimension of the considered *forbidden region* and then the implementation of the synthesis technique on different reflectarray geometries (square/rectangular).

4.1 Error metrics

This section is aimed at numerically validating the proposed closed-form expression (3.34) for the solution of the *Constraint-Geometry Reflectarray-Currents Synthesis* problem when assuming different aperture sizes and/or "forbidden region" shapes, as well as to illustrate of a set of guidelines for its effective exploitation. To quantitatively assess the accuracy in the matching of the target far-field shaped beam, the following normalized error is reported

$$\xi \triangleq \frac{\left[\sum_{l=1}^{L}\left|F_{CO}^{ref}\left(\theta_l,\varphi_l\right)-F_{CO}\left(\theta_l,\varphi_l\right)\right|+\sum_{l=1}^{L}\left|F_{CX}^{ref}\left(\theta_l,\varphi_l\right)-F_{CX}\left(\theta_l,\varphi_l\right)\right|\right]}{\left[\sum_{l=1}^{L}\left|F_{CO}^{ref}\left(\theta_l,\varphi_l\right)\right|+\sum_{l=1}^{L}\left|F_{CX}^{ref}\left(\theta_l,\varphi_l\right)\right|\right]} \tag{4.1}$$

beyond the graphical representations of the synthesized currents, of the associated patterns, and of the *difference* patterns $\Delta F_t\left(\theta,\varphi\right) \triangleq \left|F_t^{ref}\left(\theta,\varphi\right)-F_t\left(\theta,\varphi\right)\right|$, $t \in \{CO, CX\}$.

4.2 Square reflectarray: 55×55 elements

The first reflectarray antenna taken into account works at $f = 14$[GHz] and has a square aperture of 440×440 [mm^2] ($\sim 20.53\lambda \times 20.53\lambda$). The reflectarray surface is composed by $M \times N = 55 \times 55$ elements of side equal to 8 [mm] that in wavelength is almost 0.37333λ. The reflectarray configuration can be seen in Fig. 4.1 and includes an horn antenna as feeder, that is placed at almost 27λ from the reflectarray center with an inclination of 25.11 [deg] with respect to the output system, and the reflectarray is rotated along the y-axis by 12.63 [deg], thus with a relative inclination between the reflectarray surface and the horn antenna of 12.48 [deg].

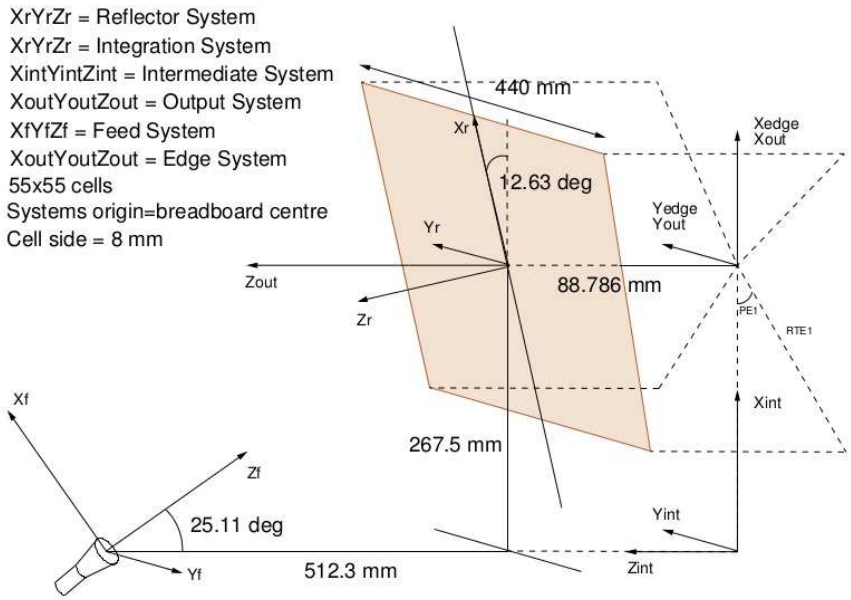

Figure 4.1: *Square Aperture* ($M \times N = 55 \times 55$, $\Delta x = \Delta y = 3.73 \times 10^{-1}\lambda$) - Reflectarray geometry.

4.2.1 Step-by-step procedure with lower dimensionality case

The first numerical experiment is devoted to a step-by-step illustration of the proposed design procedure.

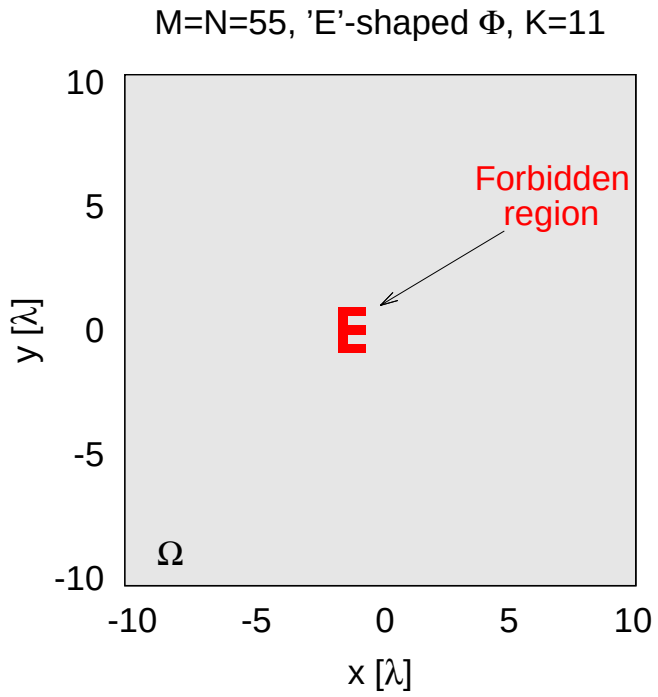

Figure 4.2: *Square Aperture* ($M \times N = 55 \times 55$, $\Delta x = \Delta y = 3.73 \times 10^{-1}\lambda$, $K = 11$) - Example of forbidden region Φ, "E"-Shape forbidden region with $K = 11$ number of elements.

4.2.1.1 Test case definition

To this end, the synthesis of the reflectarray surface currents over a $M \times N = 55 \times 55$ square aperture with a square lattice ($\Delta x = \Delta y = 3.73 \times 10^{-1}\lambda$) assuming an "E-shaped" forbidden region [Fig. 4.2 - $K = 11$] and radiating the far field component (plotted in the uv-domain, where $u = \sin\theta\cos\varphi$, $v = \sin\theta\sin\varphi$) reported in Fig. 4.3($c$) and Fig. 4.3($d$) has been addressed (for the sake of compactness and without loss of generality, only the $t = CO$ component has been considered hereinafter).

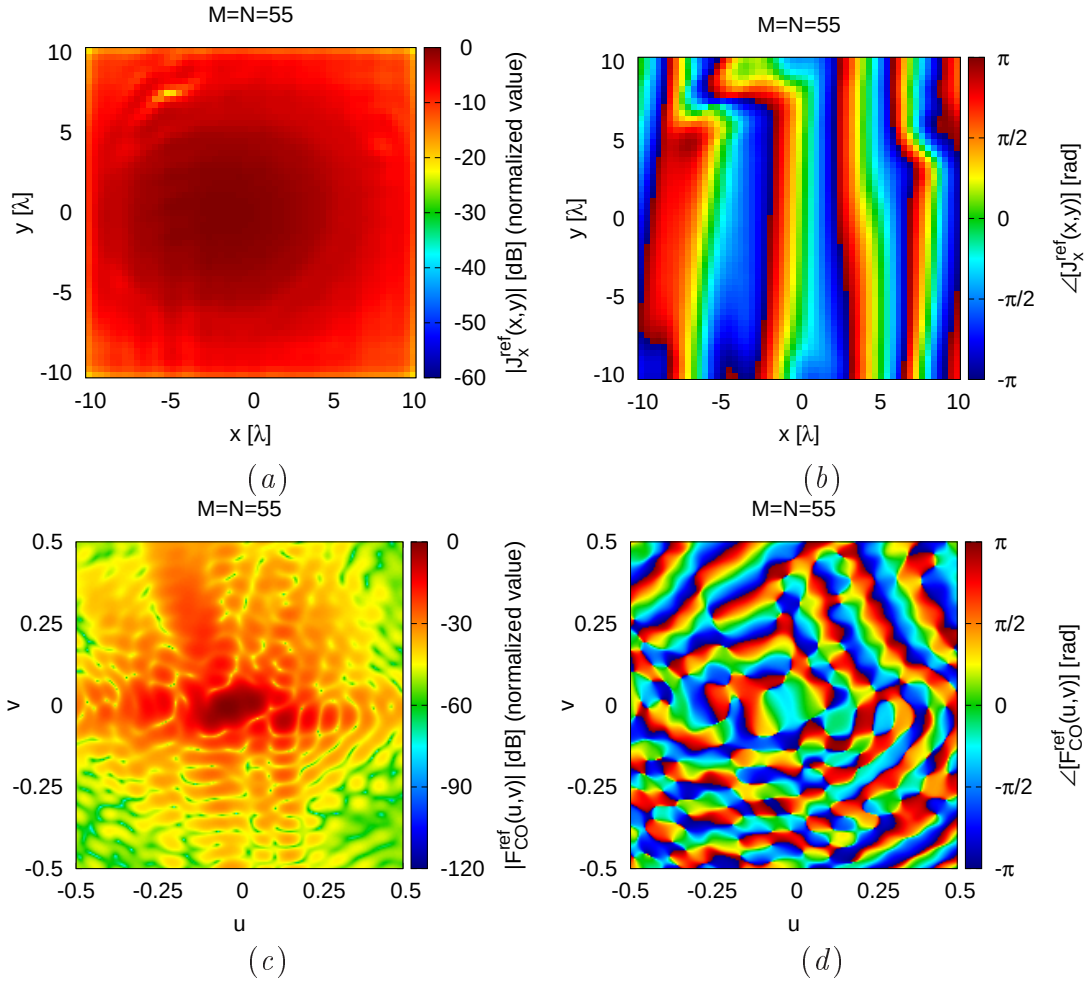

Figure 4.3: *Square Aperture* ($M \times N = 55 \times 55$, $\Delta x = \Delta y = 3.73 \times 10^{-1}\lambda$) - Plot of the reference current (a) magnitude $\left|J_x^{ref}(x,y)\right|$ and (b) phase $\angle J_x^{ref}(x,y)$and radiated field (c) magnitude$\left|F_{CO}^{ref}(u,v)\right|$ and (d) phase $\angle F_{CO}^{ref}(u,v)$.

4.2.1.2 Application of the T-SVD

Such a reference pattern, numerically generated by *TICRA GRASP* simulations [1] starting from the actual currents of a reference reflectarray [Figs. 4.3(a)-4.3(b)], has been firstly sampled in $L = 201 \times 201$ regularly spaced angles in the uv-domain to deduce $\mathbf{F}^{ref}$ in (3.5). The distribution of the singular values ψ_w, $w = 1, ..., W$, of the resulting $\mathcal{G}$ [obtained by the *SVD* decomposition (3.12)] shows that the *knee* of the Green matrix spectrum is observed when $\frac{\psi_w}{\psi_1} \approx 8.8 \times 10^{-1}$ (i.e., $w \approx 370$ - Fig. 4.4).

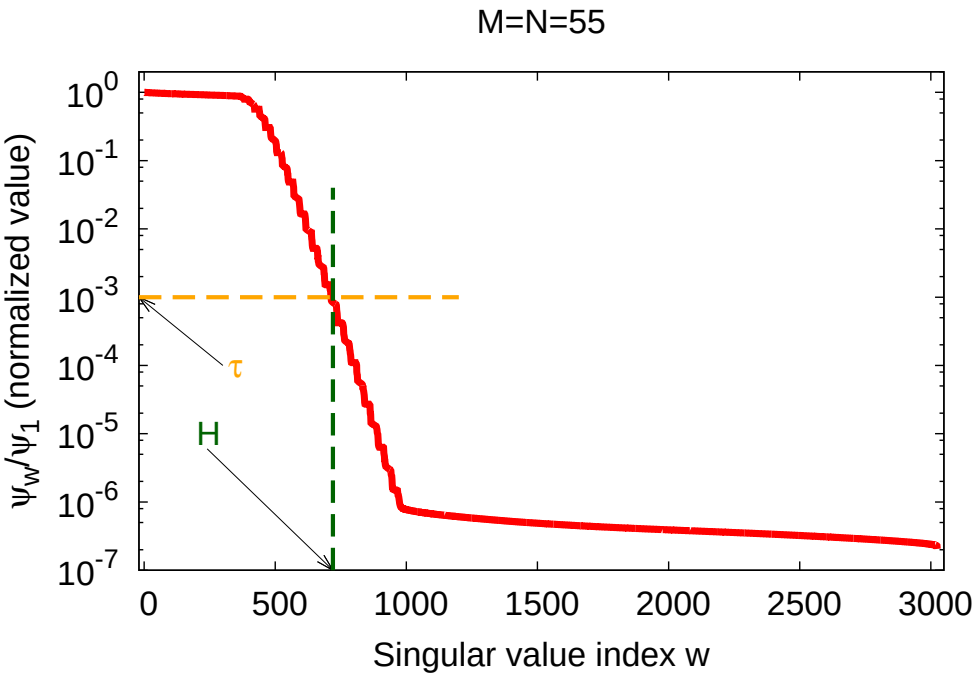

Figure 4.4: *Square Aperture* ($M \times N = 55 \times 55$, $\Delta x = \Delta y = 3.73 \times 10^{-1}\lambda$) - Distribution of the singular values ψ_w, $w = 1, ..., W$, of $\mathcal{G}$.

It is worthwhile to remark that the second *knee* in the spectrum (i.e., $\frac{\psi_w}{\psi_1} \approx 10^{-6}$ - Fig. 4.3) is actually caused by the unavoidable finite precision of the numerical *SVD* computation (which prevents an accurate evaluation of very small ψ_w) [74].

Following the standard guidelines developed in inverse scattering theory and what said in Sect. 3.2 its is computed the normalized error ξ (4.1) with different

[1] All the target field patterns in the numerical validation have been provided by Thales Alenia Space France.

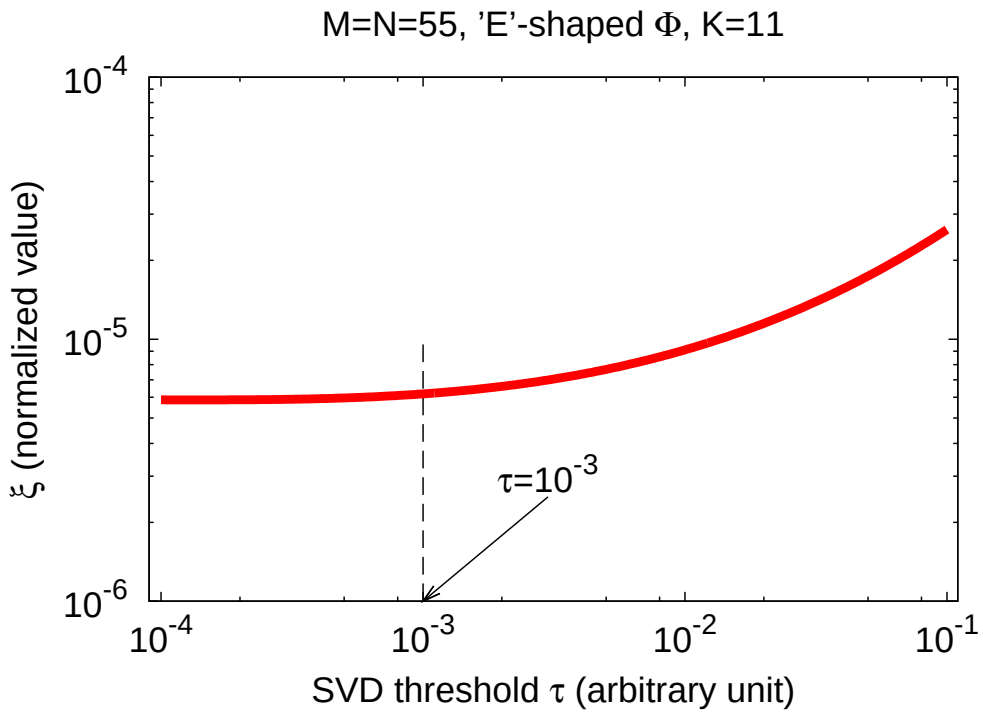

Figure 4.5: *Square Aperture* ($M \times N = 55 \times 55$, $\Delta x = \Delta y = 3.73 \times 10^{-1}\lambda$) - Normalized error ξ varying the *SVD* threshold τ.

value of the threshold τ and is reported in Fig.4.5. Taking into account both Fig. 4.4 and 4.5, it can be then deduced that a *SVD* threshold value sufficiently below such a *knee*, such as

$$\tau \approx 10^{-3} \tag{4.2}$$

(which corresponds to $H \approx 700$ - Fig. 4.4), is enough to guarantee that the field radiated by $\mathbf{J}^{\mathcal{MN}}$ reliably matches $\mathbf{F}^{ref}$ [74]-[77] and to have an relative high number of *DoFs* (number of singular value below the threshold $W - H$).

4.2.1.3 Minimum-norm current definition

To assess such a property, the *minimum-norm* currents are then computed by substituting the truncated *SVD* matrices and $\mathbf{F}^{ref}$ in (3.23).

The plots of the obtained $\mathbf{J}^{\mathcal{MN}}$ shows that such *minimum-norm* solution turns out close to the *reference* reflectarray distribution both in terms of magnitudes [Fig. 4.6(a) vs. Fig. 4.6(c)] and phases [Fig. 4.6(b) vs. Fig. 4.6(d)]. This outcome suggests that (3.23) implicitly yields the same surface currents that would be obtained by back-propagation of the *TICRA GRASP* solution [e.g., Fig. 4.6(a) vs. Fig. 4.6(c)].

Moreover, the far-field beams radiated by the two set of currents perfectly match in terms of magnitude [Fig. 4.6(e) vs. Fig. 4.6(g)] and phase [Fig. 4.6(f) vs. Fig. 4.6(h)], as expected from inverse source theory [74]-[77], thus supporting the choice of τ. Moreover, the error metric is computed also for the obtained $\mathbf{J}^{\mathcal{MN}}$ and the error is very low: $\xi^{\mathcal{MN}} = 5.54 \times 10^{-6}$.

4.2.1.4 Non-measurable current computation

Once $\mathbf{J}^{\mathcal{MN}}$ has been deduced [Figs. 4.6(c)-4.6(d)], the computation of the non-measurable currents [Figs. 4.7(a)-4.7(b)] (and of the associated far-field pattern [Figs. 4.7(c)-4.7(d)]) can be carried out by substituting (3.33) and (3.32) in (3.25). As theoretically expected, the field owing to $\mathbf{J}^{\mathcal{NR}}$ turns out negligible with respect to $\mathbf{F}^{ref}$ [Fig. 4.7(c) vs. Fig. 4.6(e)], therefore further confirming the effectiveness of (4.2).

This procedure is not completely safe. In fact the non-measurable bases $\mathbf{c}_j$ (with $j > H$) have high space variations and thus can have a null in one or more positions of Φ. During the inversion when we compute the related coefficients $\widetilde{\boldsymbol{\alpha}}$ a quasi null will go to the denominator and this generate a very high coefficient (quasi-infinite). Since the non-measurable bases are related to a singular value that is not zero, due to the truncation operation and also to computational problem, if we multiply a non-measurable source with a coefficient that is quasi-infinite we make it measurable.

Thus, the bases are always selected starting from the lower index but removing the basis that have nulls or very-low values in the forbidden region Φ.

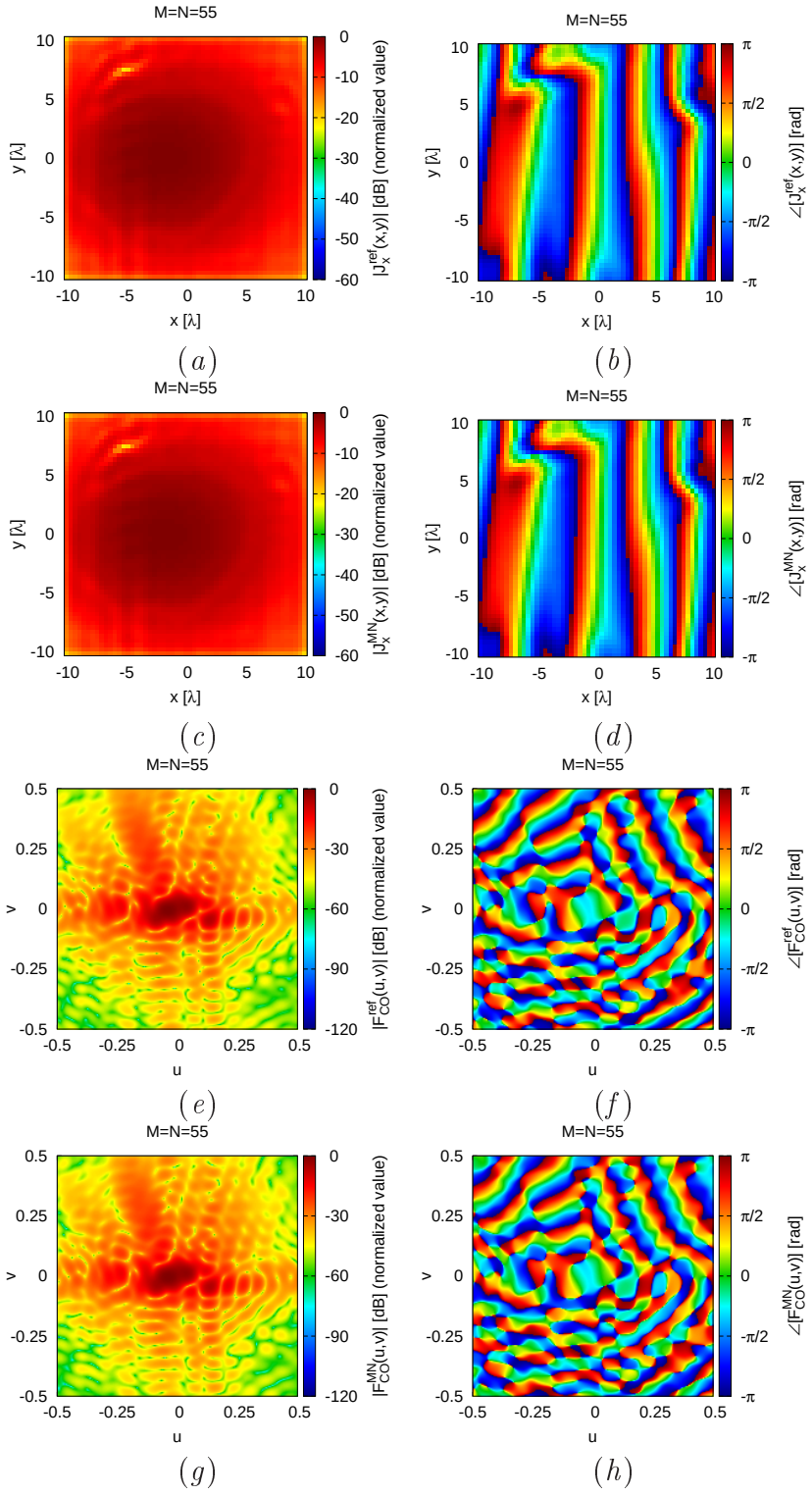

Figure 4.6: *Square Aperture* ($M \times N = 55 \times 55$, $\Delta x = \Delta y = 3.73 \times 10^{-1}\lambda$, $K = 11$) - Plots of $(a)(c)(e)(g)$ the magnitude and $(b)(d)(f)(h)$ the phase of $(a)(b)$ $J_x^{ref}(\mathbf{r})$ and synthesized $(c)(d)$ $J_x^{\mathcal{MN}}(\mathbf{r})$, $(e)(f)$ F_{CO}^{ref}, and $(g)(h)F_{CO}^{\mathcal{MN}}$.

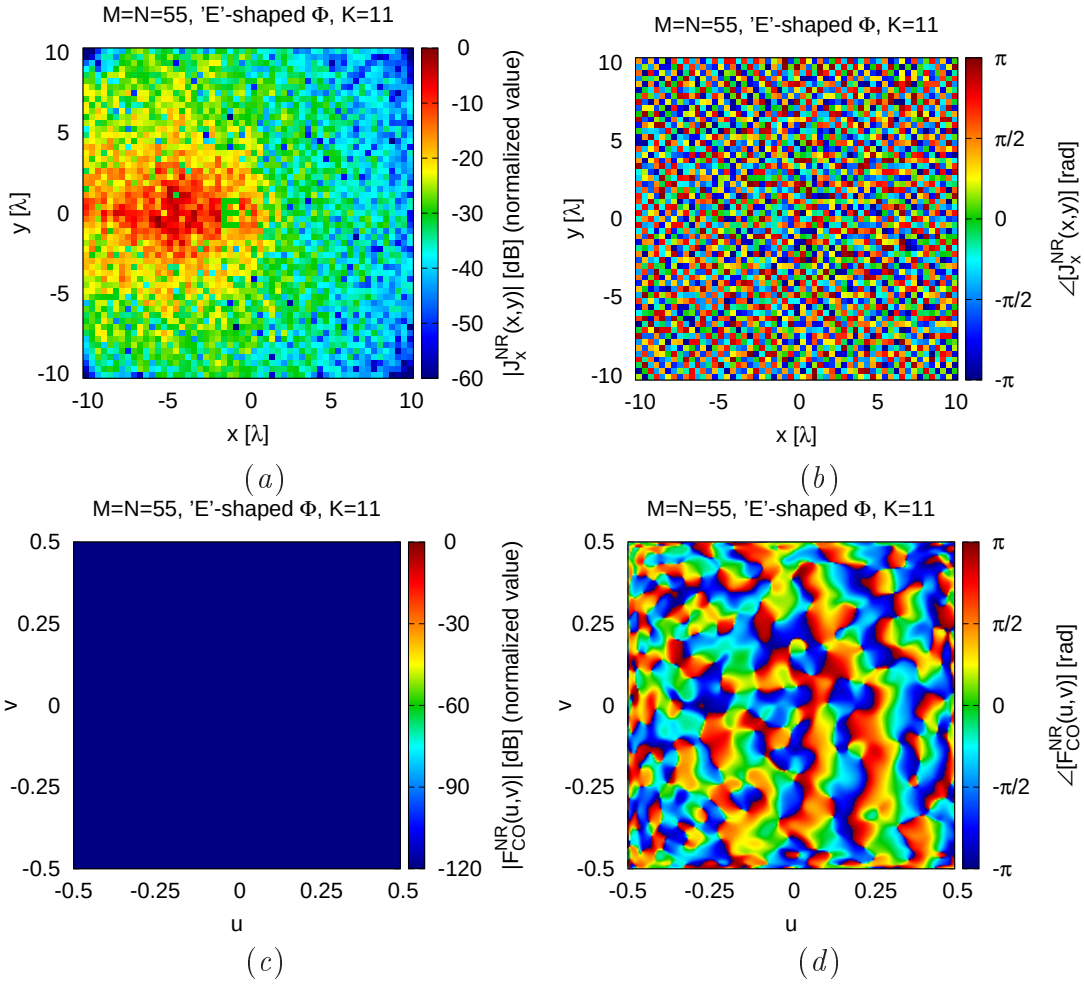

Figure 4.7: *Square Aperture* ($M \times N = 55 \times 55$, $\Delta x = \Delta y = 3.73 \times 10^{-1}\lambda$, $K = 11$) - Plots of $(a)(c)$ the magnitude and $(b)(d)$ the phase of $(a)(b)$ $J_x^{\mathcal{NR}}(\mathbf{r})$ and synthesized $(c)(d)$ $F_{CO}^{\mathcal{NR}}$.

4.2.1.5 Superficial current definition

The final step of the design procedure is then represented by the computation of $\mathbf{J}$ according by superimposing $\mathbf{J}^{\mathcal{MN}}$ and $\mathbf{J}^{\mathcal{NR}}$(3.24).

By comparing the plots of the obtained reflectarray surface current magnitude [Fig. 4.8(a)] with the geometry of the required Φ [Fig. 4.2] it turns out that the proposed method guarantees a perfect matching of the constraints on the forbidden region [Fig. 4.8(a) vs. Fig. Fig. 4.2]. Such a result is actually expected from the theoretical viewpoint since the solvability condition (3.31) is satisfied.

Moreover, despite $\mathbf{J}$ is completely different with respect to $\mathbf{J}^{\mathcal{MN}}$ [Fig. 4.6(c) vs. Fig. 4.8(a); Fig. 4.6(d) vs. Fig. 4.8(b)], also its radiated far-field matches $\mathbf{F}^{ref}$ [Fig. 4.8(c) vs. Fig. 4.6(e); Fig. 4.8(d) vs. Fig. 4.6(f)] likewise the one radiated by $\mathbf{J}^{\mathcal{MN}}$ [i.e., Figs. 4.6(g)-4.6(h)].

This outcome, which is also supported by the corresponding normalized error (i.e., $\xi = 5.84 \times 10^{-6}$- Tab. 4.1), is a proof-of-concept that suitable components $\mathbf{J}^{\mathcal{NR}}$ [Figs.4.7(a)-4.7(b)] can be superimposed to $\mathbf{J}^{\mathcal{MN}}$ [Figs.4.6(c)-4.6(d)] to satisfy user-defined current constraints while yielding a *non-measurable* variation in the radiated field [i.e., negligible with respect to $\mathbf{F}^{ref}$ - Fig. 4.8(c) vs. Fig. 4.6(e)].

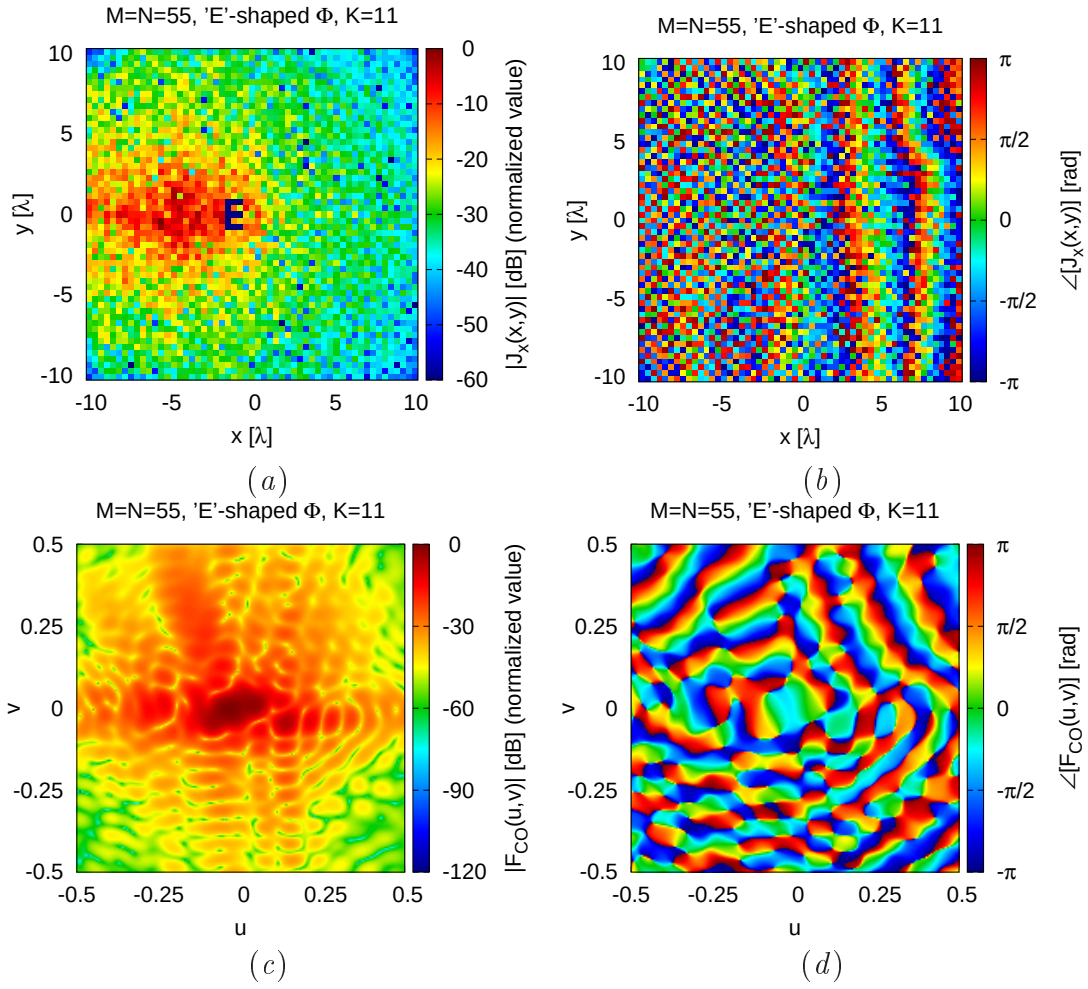

Figure 4.8: *Square Aperture* ($M \times N = 55 \times 55$, $\Delta x = \Delta y = 3.73 \times 10^{-1}\lambda$, $K = 11$) - Plots of $(a)(c)$ the magnitude and $(b)(d)$ the phase of the synthesized $(a)(b)$ $J_x(\mathbf{r})$ and $(c)(d)$ $F_{CO}(\mathbf{r})$.

4.2.2 Analysis vs. various forbidden region shapes keeping same order dimension

Given the step-by-step procedure now we want to analyse the flexibility of the proposed methodology by considering the same reflectarray setup (i.e., yielding the same SVD and $\mathbf{J}^{\mathcal{MN}}$) but different Φ definitions with almost the same geometrical dimension ($K \approx 33$): "Cross"-shaped ($K = 28$) - Fig. 4.9(a), "Ring"-shaped ($K = 32$) - Fig. 4.9(b), "Circular Ring"-shaped ($K = 36$) - Fig. 4.9(b) and "Circle"-shaped ($K = 37$) - Fig. 4.9(d).

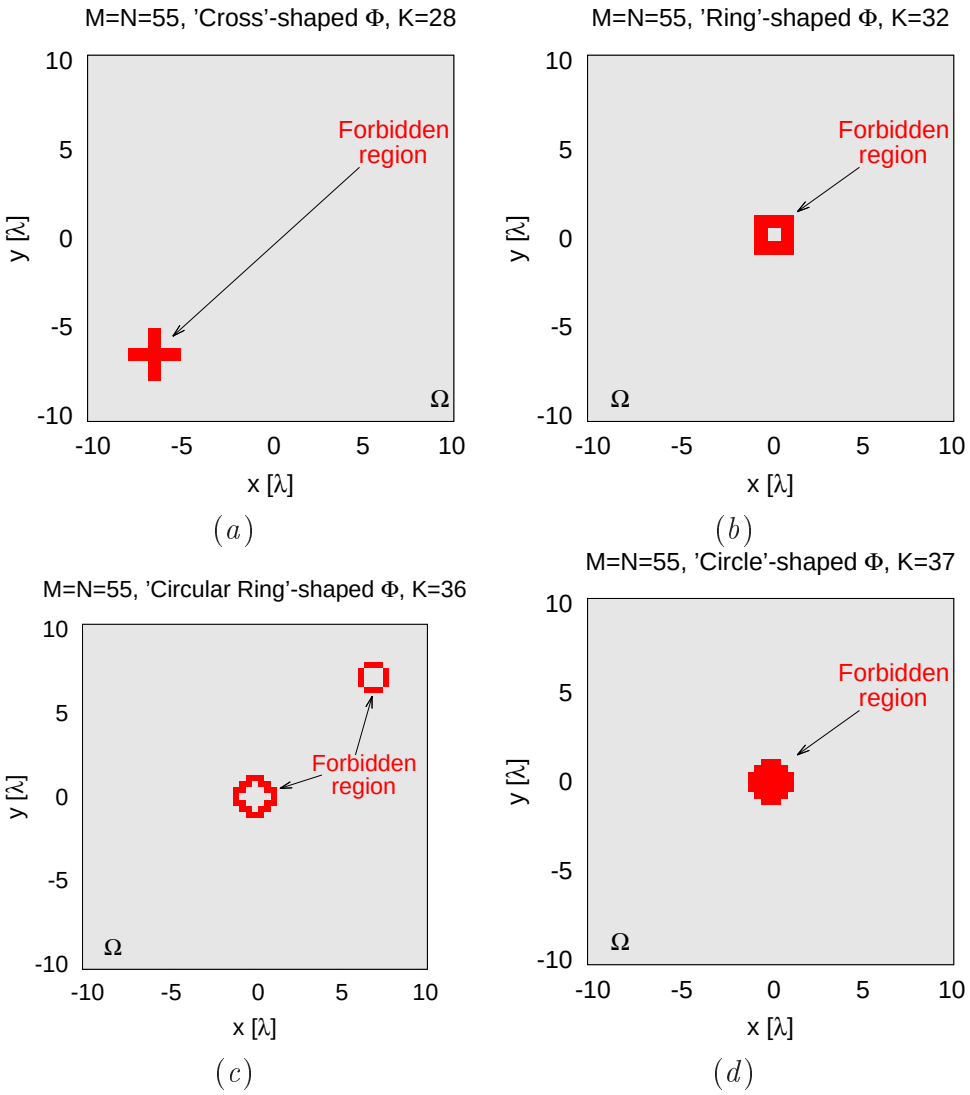

Figure 4.9: *Square Aperture* ($M \times N = 55 \times 55$, $\Delta x = \Delta y = 3.73 \times 10^{-1}\lambda$) - Definition of forbidden regions Φ.

The plots of $|\mathbf{J}|$ (Fig. 4.10) obtained by means of the closed-form expression (3.34) and associated $\Delta F_{CO}(\theta,\varphi)$ (Fig. 4.11) show that:

(i) the proposed strategy enables to deduce surface currents that comply with arbitrary Φ locations/shapes [Fig. 4.9(b) vs. Fig. 4.10(a); Fig. 4.9(c) vs. Fig. 4.10(b); Fig. 4.9(d) vs. Fig. 4.10(c)],

(ii) the resulting difference pattern is always negligible with respect to $\mathbf{F}^{ref}$ [$\Delta F_{CO}(\theta,\varphi) \leq -110$ dB - Fig. 4.11(a); $\Delta F_{CO}(\theta,\varphi) \leq -90$ dB - Fig. 4.11(b); $\Delta F_{CO}(\theta,\varphi) \leq -80$ dB - Fig. 4.11(c)], although the mismatch slightly increases with K as confirmed by the associated normalized errors (i.e., $\xi^{cross} = 1.18 \times \times 10^{-5}$, $\xi^{ring} = 3.34 \times 10^{-5}$, $\xi^{circular-ring} = 1.57 \times 10^{-5}$ and $\xi^{circle} = 1.35 \times 10^{-3}$ - Tab. 4.1).

This result is motivated by the fact that wider Φ regions require more entries to be included in $\widetilde{\boldsymbol{\alpha}}$ in (3.33) (thus potentially increasing the energy in the "non-measurable" current components). However, it is worthwhile to remark that $|\Delta F_{CO}(\theta,\varphi)| \ll \left|F_{CO}^{REF}(\theta,\varphi)\right|$ in all cases [e.g., Fig. 4.11(e) vs. Fig. 4.3(a)], and that even better ξ results could be easily obtained by further decreasing τ with respect to (4.2), as it is known from inverse source theory [74]-[76].

Φ- Shape	K	ξ	Δt (s)
-	-	5.55×10^{-6}	-
E	11	5.84×10^{-5}	1.03×10^{-1}
Cross	28	1.18×10^{-5}	1.21×10^{-1}
Ring	32	3.34×10^{-5}	1.28×10^{-1}
Circular Ring	36	1.57×10^{-5}	1.34×10^{-1}
Circle	37	1.35×10^{-3}	1.36×10^{-1}

Table 4.1: *Square Aperture* ($M \times N = 55 \times 55$, $\Delta x = \Delta y = 3.73 \times 10^{-1}\lambda$) - *Performance Assessment* - Varying the geometry.

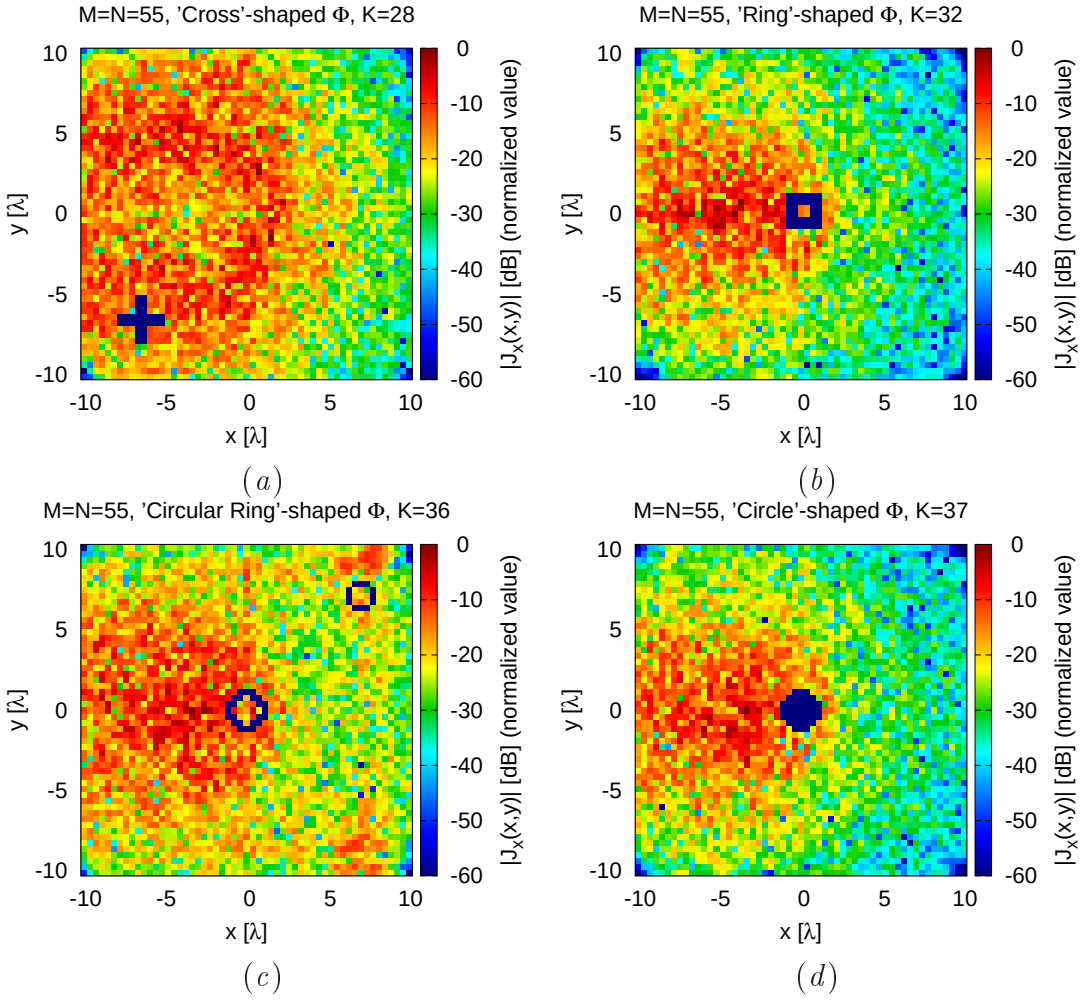

Figure 4.10: *Square Aperture* ($M \times N = 55 \times 55$, $\Delta x = \Delta y = 3.73 \times 10^{-1}\lambda$) - Plots of $|J_x(\mathbf{r})|$ assuming (a) "Cross"-shaped ($K = 28$), (b) "Ring"-shaped ($K = 32$), (c) "Circular Ring"-shaped ($K = 36$) and (d) "Circle"-shaped ($K = 37$) forbidden regions.

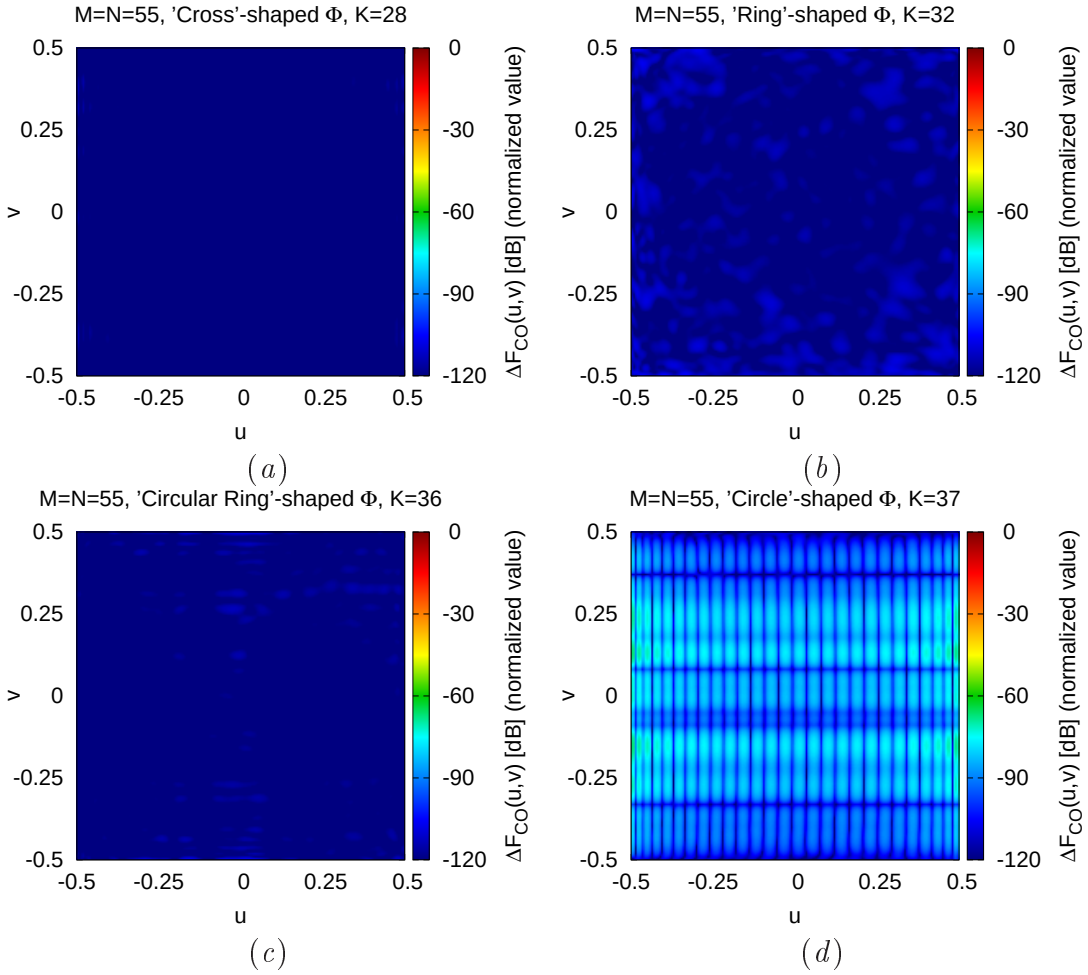

Figure 4.11: *Square Aperture* ($M \times N = 55 \times 55$, $\Delta x = \Delta y = 3.73 \times 10^{-1}\lambda$) - Plots of $\Delta F_{CO}(u, v)$ when assuming (a) "Cross"-shaped ($K = 28$), (b) "Ring"-shaped ($K = 32$), (c) "Circular Ring"-shaped ($K = 36$) and (d) "Circle"-shaped ($K = 37$) forbidden regions.

4.2.3 Changing the dimension of the same type of forbidden region

To further investigate the features of the proposed current synthesis procedure for different K values, a set of off-centered "Square"-shaped Φ regions with $K \in [4, 100]$ have been considered. The Φ for $K = 4$, $K = 25$, $K = 49$, $K = 100$ are shown in Fig. 4.12.

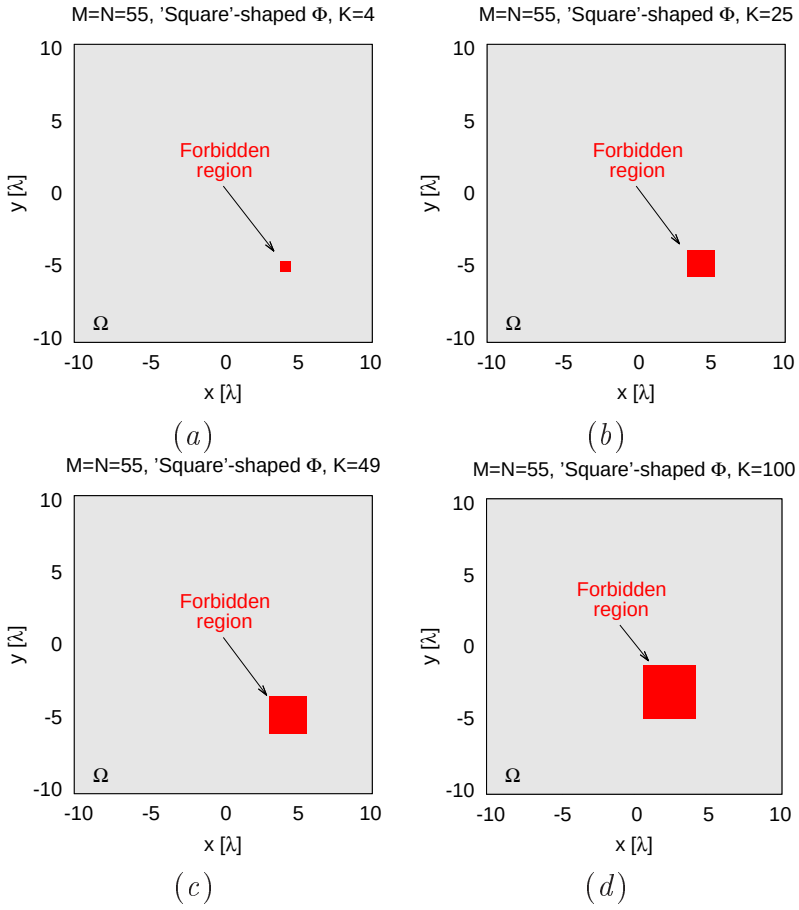

Figure 4.12: *Square Aperture* ($M \times N = 55 \times 55$, $\Delta x = \Delta y = 3.73 \times 10^{-1}\lambda$) - Definition of forbidden regions Φ keeping the same shape but varying the dimension: $(a)K = 4$, $(b)K = 25$, $(c)K = 49$ and $(d)K = 100$.

The behaviour of the normalized error vs. the forbidden region size shows that, analogously to the previous examples, ξ is proportional to K. In fact when $K = 4$ the normalized error is very small and comparable with the normalized error of the minimum-norm term $\xi\rfloor_{K=4} \approx 5.71 \times 10^{-6}$, while when $K = 100$ the

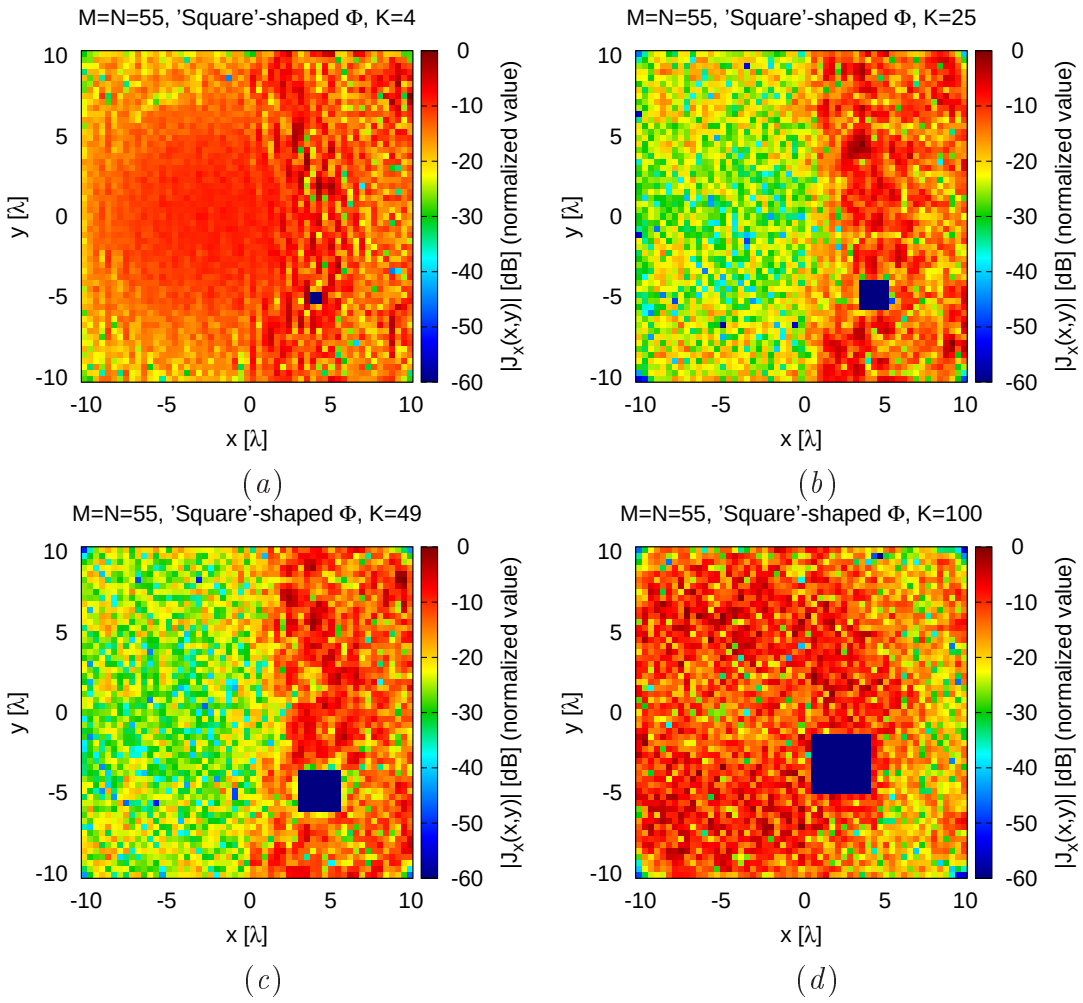

Figure 4.13: *Square Aperture* ($M \times N = 55 \times 55$, $\Delta x = \Delta y = 3.73 \times 10^{-1}\lambda$) - Plots of $|J_x(\mathbf{r})|$ assuming different dimension of a "Square"-shape $(a) K = 4$, (b) $K = 25$, (c) $K = 49$ and (d) $K = 100$ forbidden regions.

normalized error grown up until $\xi\rfloor_{K=100} \approx 2.07 \times 10^{-3}$ (shown in Fig. 4.15 and in Tab. 4.2). Nevertheless, $|\Delta F_{CO}(\theta, \varphi)|$ still turns out negligible with respect to $\left|F_{CO}^{REF}(\theta, \varphi)\right|$ even for wide Φ regions [e.g., $K = 100$ - Fig. 4.14(d) vs. Fig. 4.3(a)].

Furthermore, a perfect matching of the current constraints in the forbidden region is obtained also in this case for each of the selected dimensions [$K = 4$ - Fig. 4.13(a), $K = 25$ - Fig. 4.13(b), $K = 49$ - Fig. 4.13(c) and $K = 100$ - Fig. 4.13(d)], as expected thanks to the compliancy with the solvability condition (3.31).

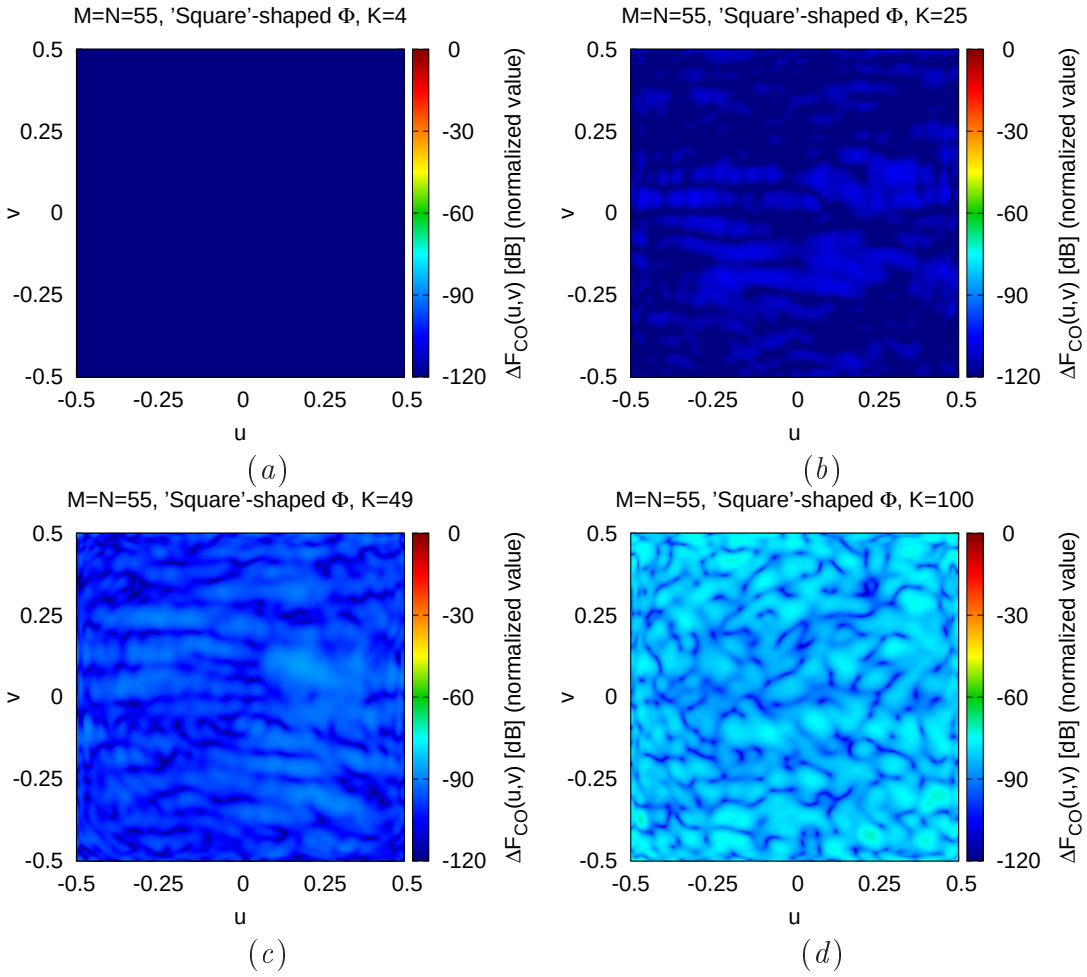

Figure 4.14: *Square Aperture* ($M \times N = 55 \times 55$, $\Delta x = \Delta y = 3.73 \times 10^{-1}\lambda$) - Plots of $\Delta F_{CO}(u, v)$ when assuming different dimension of a "Square"-shape $(a) K = 4$, (b) $K = 25$, (c) $K = 49$ and (d) $K = 100$ forbidden regions.

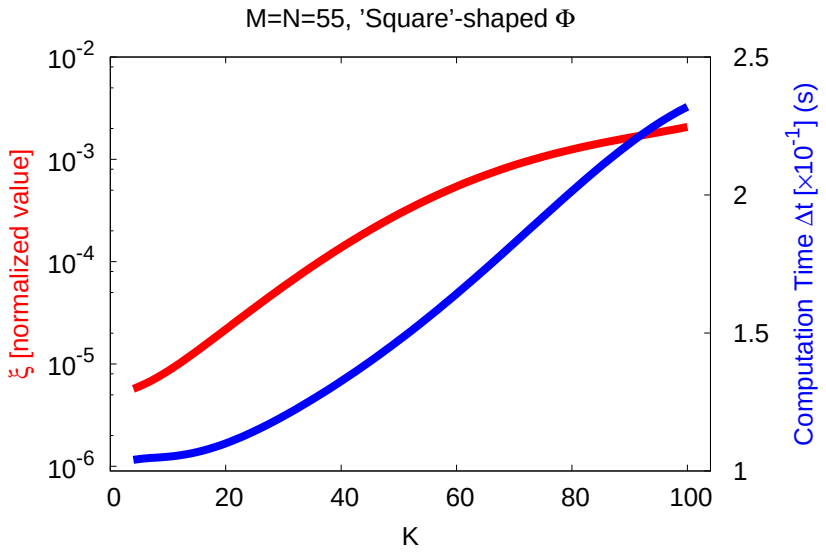

Figure 4.15: *Square Aperture* ($M \times N = 55 \times 55$, $\Delta x = \Delta y = 3.73 \times 10^{-1}\lambda$, "Square"-shaped forbidden region) - Behaviour of ξ and Δt versus K.

Φ- Shape	K	ξ	Δt (s)
-	-	5.55×10^{-6}	-
Square	4	5.71×10^{-6}	1.03×10^{-1}
Square	9	7.32×10^{-6}	1.06×10^{-1}
Square	16	1.20×10^{-5}	1.04×10^{-1}
Square	25	4.32×10^{-5}	1.04×10^{-1}
Square	36	1.11×10^{-4}	1.36×10^{-1}
Square	49	3.59×10^{-4}	1.32×10^{-1}
Square	64	1.09×10^{-3}	1.68×10^{-1}
Square	81	1.27×10^{-3}	2.12×10^{-1}
Square	100	2.07×10^{-3}	2.32×10^{-1}

Table 4.2: *Square Aperture* ($M \times N = 55 \times 55$, $\Delta x = \Delta y = 3.73 \times 10^{-1}\lambda$) - *Performance Assessment* - Fixed geometry varying the dimension.

4.2.4 Large dimension and complex topology forbidden region

The next example is aimed at assessing the performance of (3.34) when more complex forbidden regions are at hand.

To this end, a synthesis of **J** has been carried out when assuming a Φ area composed of:

(*i*) a "Triangle"-shaped, $K = 55$ in slightly different position [Fig. 4.16$(a)(b)$],

(*ii*) 6 disconnected sub-parts ["ELEDIA"-shaped, $K = 54$ - Fig. 4.16(c)],

(*iii*) a large region centered in the reflectarray aperture ["Diamond"-shaped, $K = 115$ - Fig. 4.16(d)].

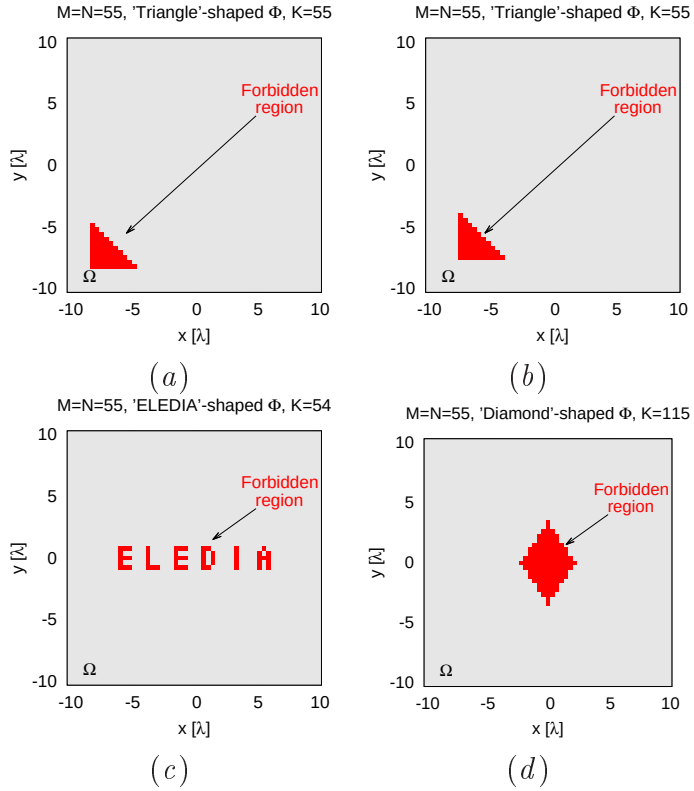

Figure 4.16: *Square Aperture* ($M \times N = 55 \times 55$, $\Delta x = \Delta y = 3.73 \times 10^{-1}\lambda$) - Definition of forbidden regions Φ with complex shape and large dimension: (a) "Triangle"-shaped $K = 55$ nearer to the corner, (b) "Triangle"-shaped $K = 55$, (c) "ELEDIA"-shaped $K = 54$ and (d) "Diamond"-shaped $K = 115$.

By analyzing the graphical representation of the surface current magnitudes ["Triangle"-shaped - Fig. 4.17$(a)(b)$, "ELEDIA"-shaped - Fig. 4.17(c), "Diamond"-shaped - Fig. 4.17(d)] and corresponding $\Delta F_{CO}(\theta, \varphi)$ ["Triangle"-shaped - Fig. 4.18$(a)(b)$, "ELEDIA"-shaped - Fig. 4.18(b), "Diamond"-shaped - Fig. 4.18(d)], it can be noticed once again that the deduced solution fully complies with the enforced geometrical restrictions [Fig. 4.17(a) vs. Fig. 4.16(a), Fig. 4.17(b) vs. Fig. 4.16(b), Fig. 4.18(c) vs. Fig. 4.16(c) and Fig. 4.17(d) vs. Fig. 4.16(d)].

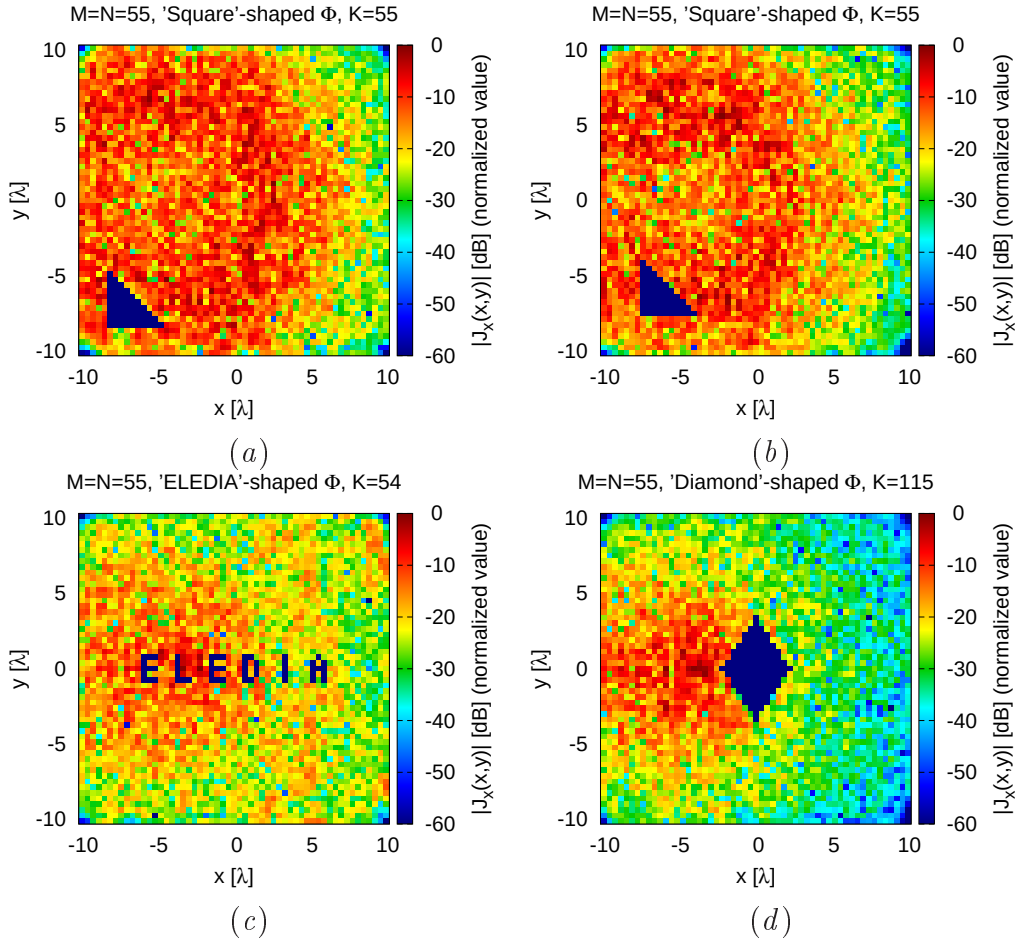

Figure 4.17: *Square Aperture* ($M \times N = 55 \times 55$, $\Delta x = \Delta y = 3.73 \times 10^{-1}\lambda$) - Plots of $|J_x(\mathbf{r})|$ assuming different dimension of a "Square"-shape $(a) K = 4$, (b) $K = 25$, (c) $K = 49$ and (d) $K = 100$ forbidden regions.

Moreover, also the radiation features achieve good performance [$|\Delta F_{CO}(\theta,\varphi)| \ll |F_{CO}^{REF}(\theta,\varphi)|$ - Fig. 4.18 vs. Fig. 4.3(a)], as it is also confirmed by the associated error figures ($\xi^{triangle-a} = 9.94 \times 10^{-4}$, $\xi^{triangle-b} = 1.07 \times 10^{-4}$,$\xi^{eledia} = 1.41 \times 10^{-5}$, $\xi^{diamond} = 4.34 \times 10^{-3}$ - Tab. 4.3).

This result points out the capability of the proposed methodology to exploit *non-measurable* currents to comply with arbitrary-shaped forbidden areas comprising disconnected regions [Fig. 4.17(a)] regardless of their position in the aperture [Fig. 4.17(c)] if Φ complies with (3.31).

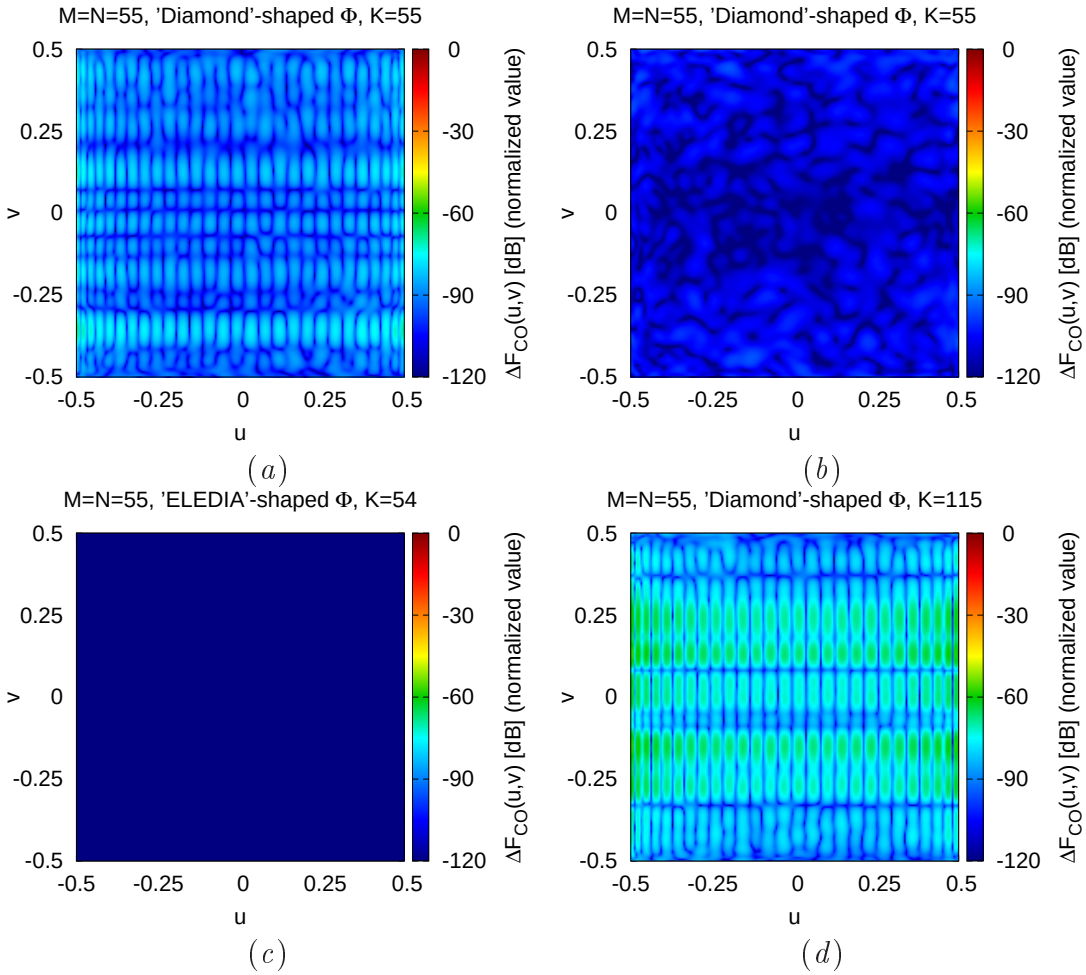

Figure 4.18: *Square Aperture* ($M \times N = 55 \times 55$, $\Delta x = \Delta y = 3.73 \times 10^{-1}\lambda$) - Plots of $\Delta F_{CO}(u,v)$ when assuming different dimension of a "Square"-shape (a)$K = 4$, (b) $K = 25$, (c) $K = 49$ and (d) $K = 100$ forbidden regions.

Φ- Shape	K	ξ	Δt (s)
-	-	5.55×10^{-6}	-
Triangle (a)	55	9.94×10^{-4}	1.41×10^{-1}
Triangle (b)	55	1.07×10^{-4}	1.40×10^{-1}
ELEDIA	54	1.41×10^{-5}	1.39×10^{-1}
Diamond	115	4.34×10^{-3}	2.62×10^{-1}

Table 4.3: *Square Aperture* ($M \times N = 55 \times 55$, $\Delta x = \Delta y = 3.73 \times 10^{-1}\lambda$) - *Performance Assessment* - Complex and large geometries.

4.3 Rectangular reflectarray: 81×69 elements

Since the previous examples have all dealt with a square reflectarray geometry with a $M = N = 55$ aperture, the final set of numerical studies is devoted to the validation of the proposed methodology when *wider* and *rectangular* layouts are at hand.

The second reflectarray antenna taken into account works at $f = 3.6$[GHz] and has a rectangular aperture of 1766.4×2073.6 [mm^2] ($\sim 21.19\lambda \times 24.88\lambda$). The reflectarray surface is composed by $M \times N = 81 \times 69$ elements of side equal to 25.6 [mm] that in wavelength is almost 0.3072λ. This reflectarray configuration (shown in Fig. 4.19) has as a feeder an horn antenna that is placed with an inclination of 35.06 [deg] with respect to the output system at almost 30λ from the reflectarray center, the plane of the reflectarray surface is rotated along the y-axis by 17.53 [deg], thus with a relative inclination between the reflectarray surface and the horn antenna of 17.53 [deg].

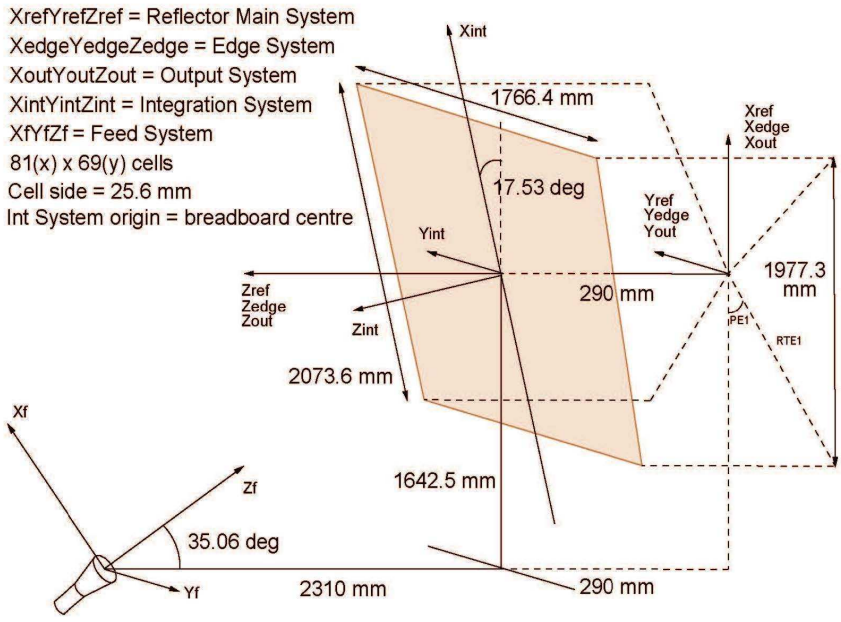

Figure 4.19: *Rectangular Aperture* ($M \times N = 81 \times 69$, $\Delta x = \Delta y = 3.07 \times 10^{-1}\lambda$) - Reflectarray geometry.

This reflectarray antenna is used to synthesize a surface current assuming the reference far-field pattern in Fig. 4.20$(c)(d)$ still sampled in $L = 201 \times 201$

regularly spaced angles in the uv-domain to deduce $\mathbf{F}^{ref}$ in (3.5). Moreover the reference current distribution magnitude and phase are shown in Fig. 4.20(a) and Fig. 4.20(b) respectively. Also in this case the *SVD* threshold τ is set to 10^{-3} and the normalized error of the radiated field of the *minimum-norm* solution [magnitude and phase of $\mathbf{J}^{\mathcal{MN}}$ in Fig. 4.20(e) and Fig. 4.20(f) respectively] with respect to the reference field [Fig. 4.20(g) vs. 4.20(c)] is very low also in this case $\xi = 4.47 \times 10^{-6}$ (see Tab. 4.4).

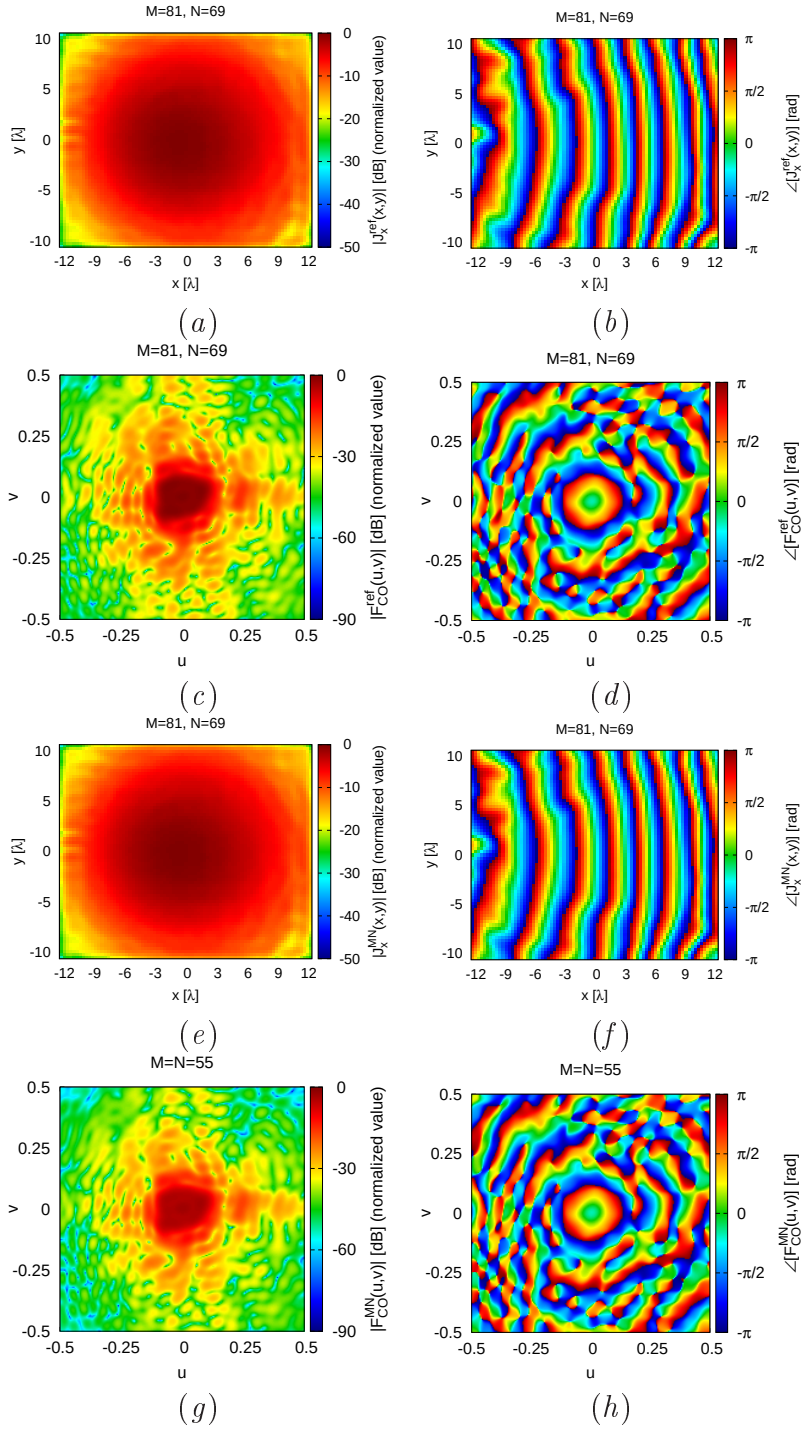

Figure 4.20: *Rectangular Aperture* ($M \times N = 81 \times 69$, $\Delta x = \Delta y = 3.07 \times 10^{-1}\lambda$) - Plot of the reference current (a) magnitude $\left|J_x^{ref}(x,y)\right|$ and (b) phase $\angle J_x^{ref}(x,y)$ and radiated field (c) magnitude $\left|F_{CO}^{ref}(u,v)\right|$ and (d) phase $\angle F_{CO}^{ref}(u,v)$ and the *minimum-norm* solution (e) magnitude $\left|J_x^{\mathcal{MN}}(x,y)\right|$ and (f) phase $\angle J_x^{\mathcal{MN}}(x,y)$and radiated field (g) magnitude $\left|F_{CO}^{\mathcal{MN}}(u,v)\right|$ and (h) phase $\angle F_{CO}^{\mathcal{MN}}(u,v)$.

4.3.1 Large dimension and complex topology of the forbidden region

In order to asses the method changing the reflectarray antenna we propose an analysis on the same forbidden region investigated for the previous case (Sect. 4.2.4). Towards this end, we enforce the "ELEDIA"-shaped and "Diamond"-shaped forbidden regions shown in Fig. 4.21(a) and Fig. 4.21(b), respectively.

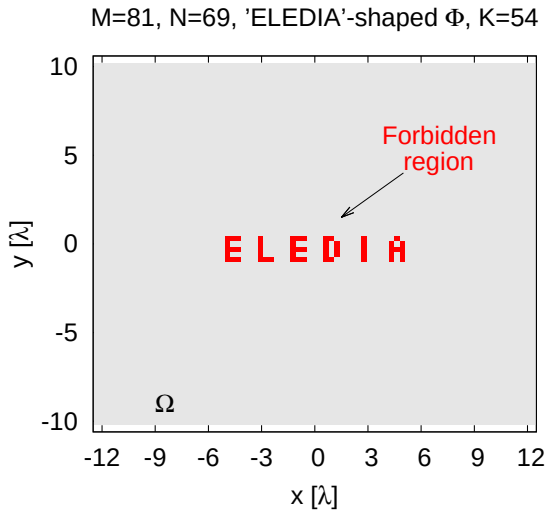

(a)

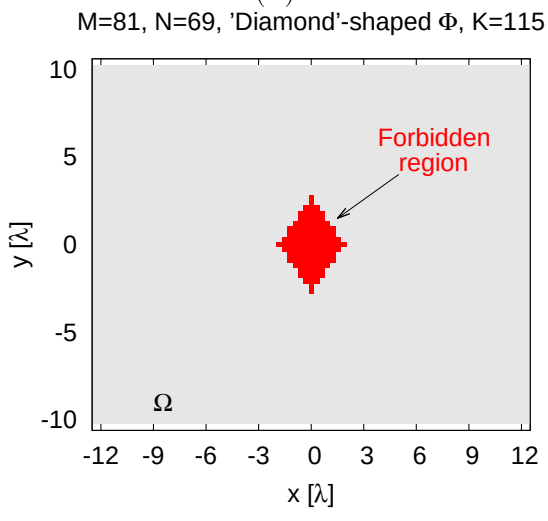

(b)

Figure 4.21: *Square Aperture* ($M \times N = 55 \times 55$, $\Delta x = \Delta y = 3.73 \times 10^{-1}\lambda$) - Definition of forbidden regions Φ with complex shape and large dimension: (a) "ELEDIA"-shaped $K = 54$ and (b) "Diamond"-shaped $K = 115$.

The plots the magnitude [Fig. 4.20(e)] and phase [Fig. 4.20(f)] of $\mathbf{J}^{\mathcal{MN}}$ [obtained assuming (4.2)] indicate that the *minimum-norm* solution of the problem obviously does not comply with any Φ requirements [i.e., the current is not zero in Φ - Fig. 4.22(a)], as expected.

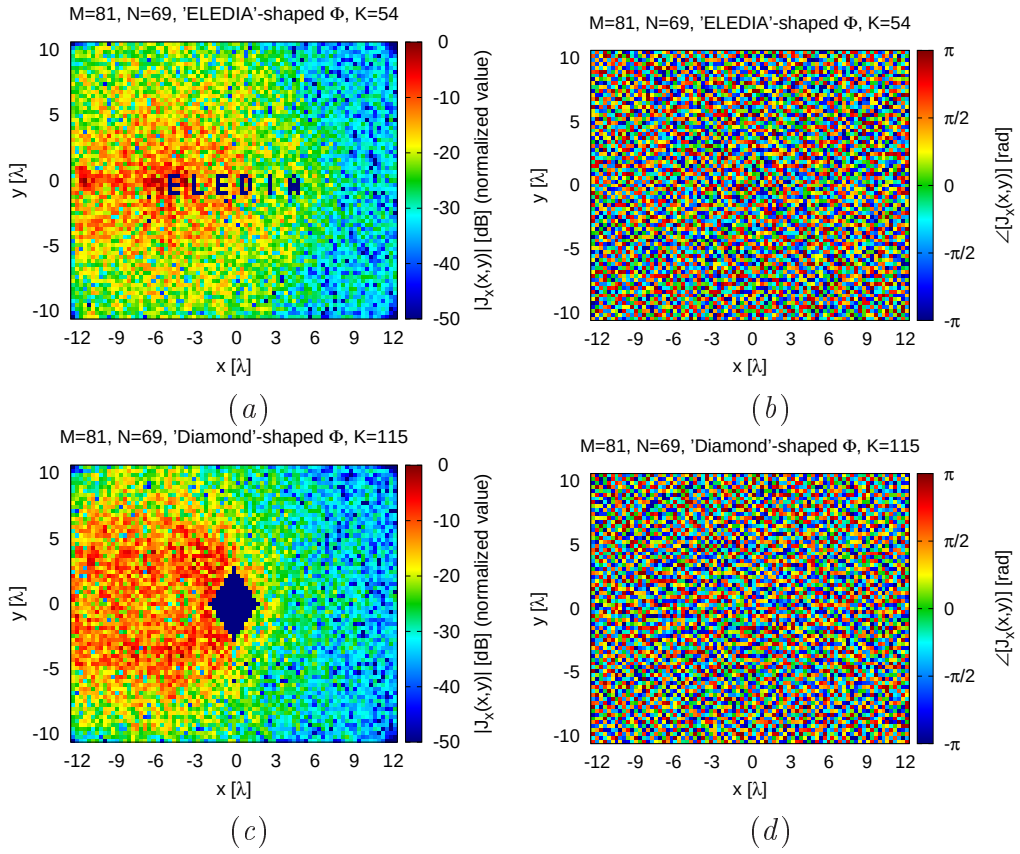

Figure 4.22: *Rectangular Aperture* ($M \times N = 81 \times 69$, $\Delta x = \Delta y = 3.07 \times 10^{-1}\lambda$) - Plots of $(a)(c)$ the magnitude and and $(b)(d)$ the phase of $J_x(\mathbf{r})$ when assuming $(a)(b)$ "ELEDIA"-shaped ($K = 54$) and $(c)(d)$ "Diamond"-shaped ($K = 115$) forbidden regions.

On the contrary, the overall surface currents obtained by superimposing suitably designed *non-measurable* currents to $\mathbf{J}^{\mathcal{MN}}$ through the closed-form expression (3.34) fully satisfy the "forbidden region" constraints [Fig. 4.22(a) vs. Fig. 4.16(a); Fig. 4.22(c) vs. Fig. 4.16(b)], and they also guarantee an excellent pattern matching [i.e., $|\Delta F_{CO}(\theta,\varphi)| \ll \left|F_{CO}^{REF}(\theta,\varphi)\right|$ - Fig. 4.23(a) and Fig. 4.23(b) vs. Fig. 4.20(a)], as it is also confirmed by the corresponding error figures ($\xi \in [1.31 \times 10^{-5}, 7.68 \times 10^{-4}]$ - Tab. 4.4).

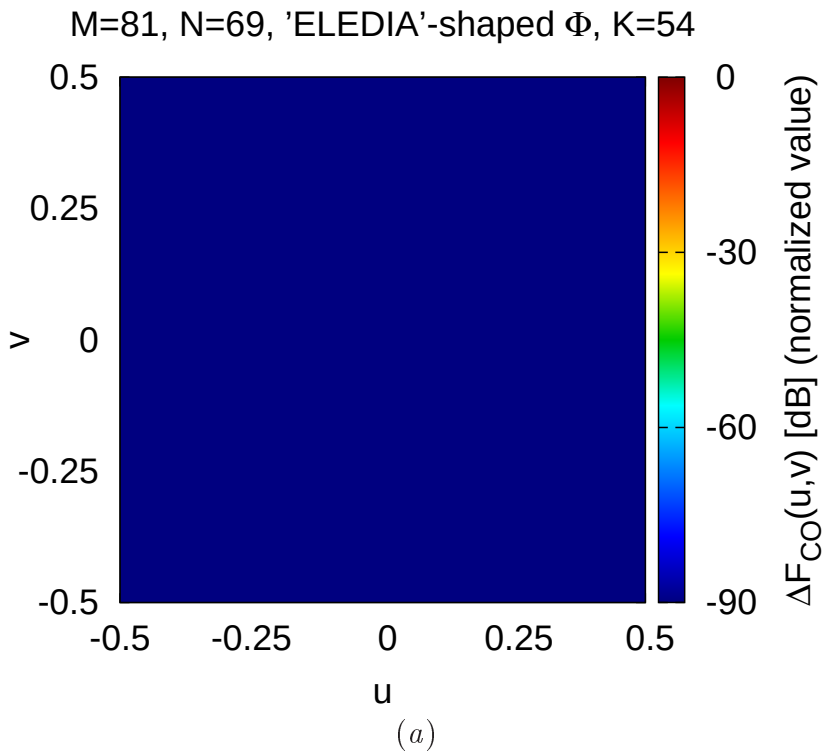

(a)

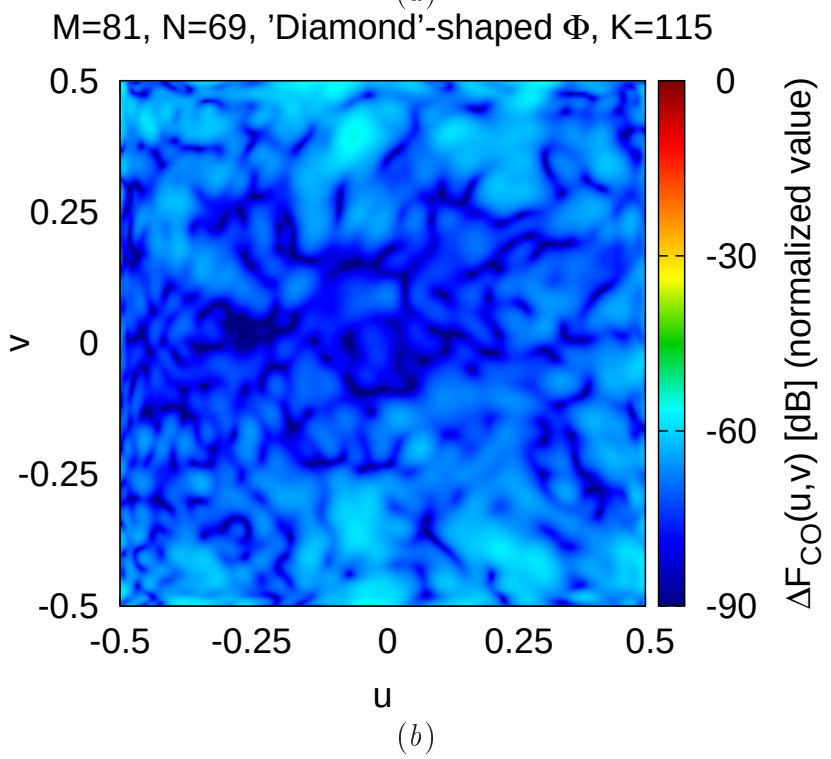

(b)

Figure 4.23: *Rectangular Aperture* ($M \times N = 81 \times 69$, $\Delta x = \Delta y = 3.07 \times 10^{-1}\lambda$) - Plots of $\Delta F_{CO}(u, v)$ when assuming (a) "ELEDIA"-shaped ($K = 54$) and (b) "Diamond"-shaped ($K = 115$) forbidden regions.

4.3.2 Varying shape of forbidden region

Also for this reflectarray it is proposed the analysis varying the shapes of the forbidden region Φ. The same shapes defined for the test case $M \times N = 55 \times 55$ are here proposed. In particular: "E"-shaped $K = 11$ in Fig. 4.24(a), in Fig. 4.24(b) "Cross"-shaped $K = 28$, in Fig. 4.24(c) "Ring"-shaped $K = 32$,in Fig. 4.24 (d) "Circular Ring"-shaped $K = 36$ and in Fig. 4.24(e) "Circle"-shaped $K = 37$.

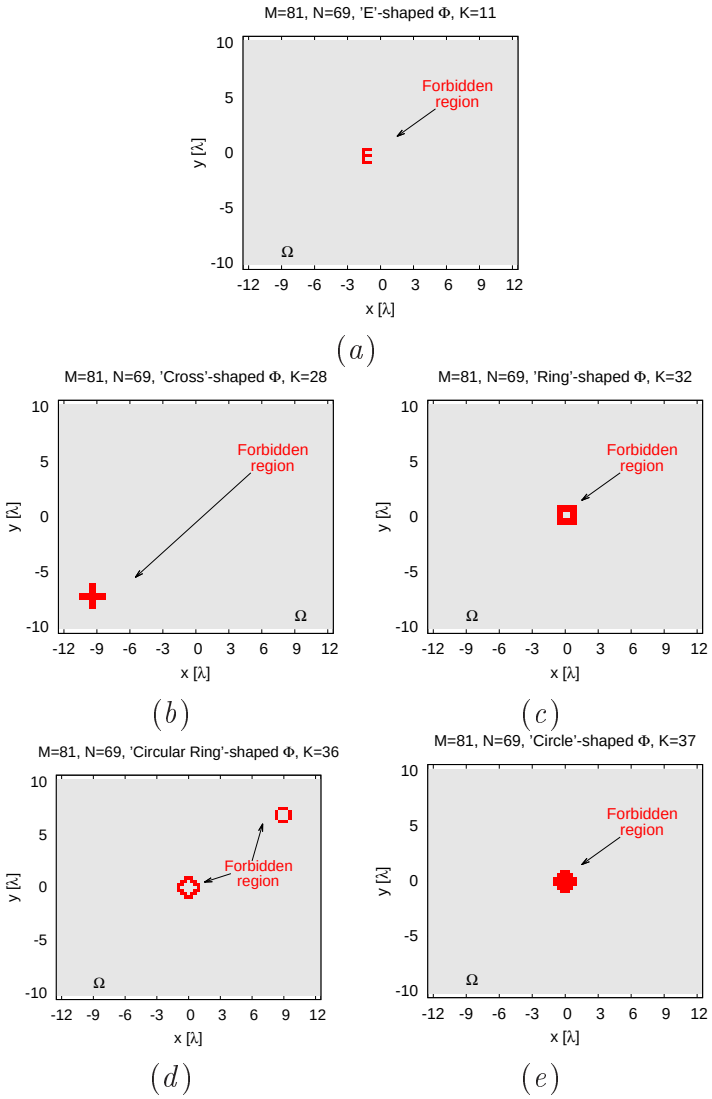

Figure 4.24: *Square Aperture* ($M \times N = 55 \times 55$, $\Delta x = \Delta y = 3.73 \times 10^{-1}\lambda$) - Definition of forbidden regions Φ with different shapes: (a) "E"-shaped $K = 11$, (b) "Cross"-shaped $K = 28$, (c) "Ring"-shaped $K = 32$, (d) "Circular Ring"-shaped $K = 36$ and (e) "Circle"-shaped $K = 37$.

The current obtained using the final closed form (3.34) and the superposition (3.24) perfectly fulfill the requirements $\mathcal{S}$ of the forbidden regions taken into account [“E”-shaped $K = 11$ in Fig. 4.10(a) vs. Fig. 4.24(a) - “Cross”-shaped $K = 28$ in Fig. 4.10(b) vs. Fig. 4.24(b) - “Ring”-shaped $K = 32$ in Fig. 4.10(c) vs. Fig. 4.24(c) - “Circular Ring”-shaped $K = 36$ in Fig. 4.10(d) vs. Fig. 4.24(d) - “Circle”-shaped $K = 37$ in Fig. 4.10(e) vs. Fig. 4.24(e)], as expected since the solvability condition is observed (3.31).

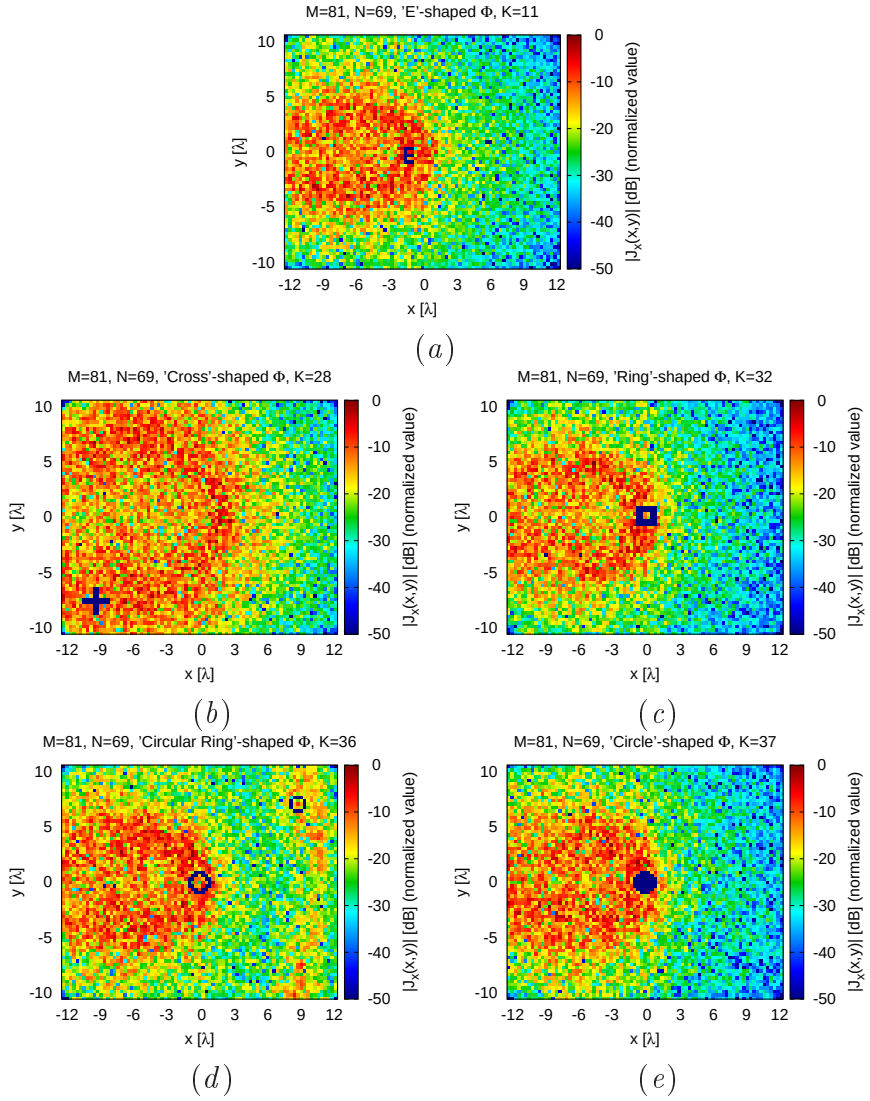

Figure 4.25: *Square Aperture* ($M \times N = 55 \times 55$, $\Delta x = \Delta y = 3.73 \times 10^{-1}\lambda$) - Plots of $|J_x(\mathbf{r})|$ assuming an (a) “E”-shaped $K = 11$, (b) “Cross”-shaped $K = 28$, (c) “Ring”-shaped $K = 32$, (d) “Circular Ring”-shaped $K = 36$ and (e) “Circle”-shaped $K = 37$ forbidden.

Moreover, the difference of the pattern shown in Fig. 4.26 demonstrate the goodness of the pattern matching ($|\Delta F_{CO}(\theta,\varphi)| \ll \left|F_{CO}^{REF}(\theta,\varphi)\right|$), that is confirmed also by the normalized errors: $\xi^{E} = 5.51 \times 10^{-6}$, $\xi^{Cross} = 5.81 \times 10^{-6}$, $\xi^{Ring} = 1.03 \times 10^{-5}$, $\xi^{Circular-Ring} = 9.72 \times 10^{-6}$, $\xi^{Circle} = 1.26 \times 10^{-5}$ (listed in Tab. 4.4).

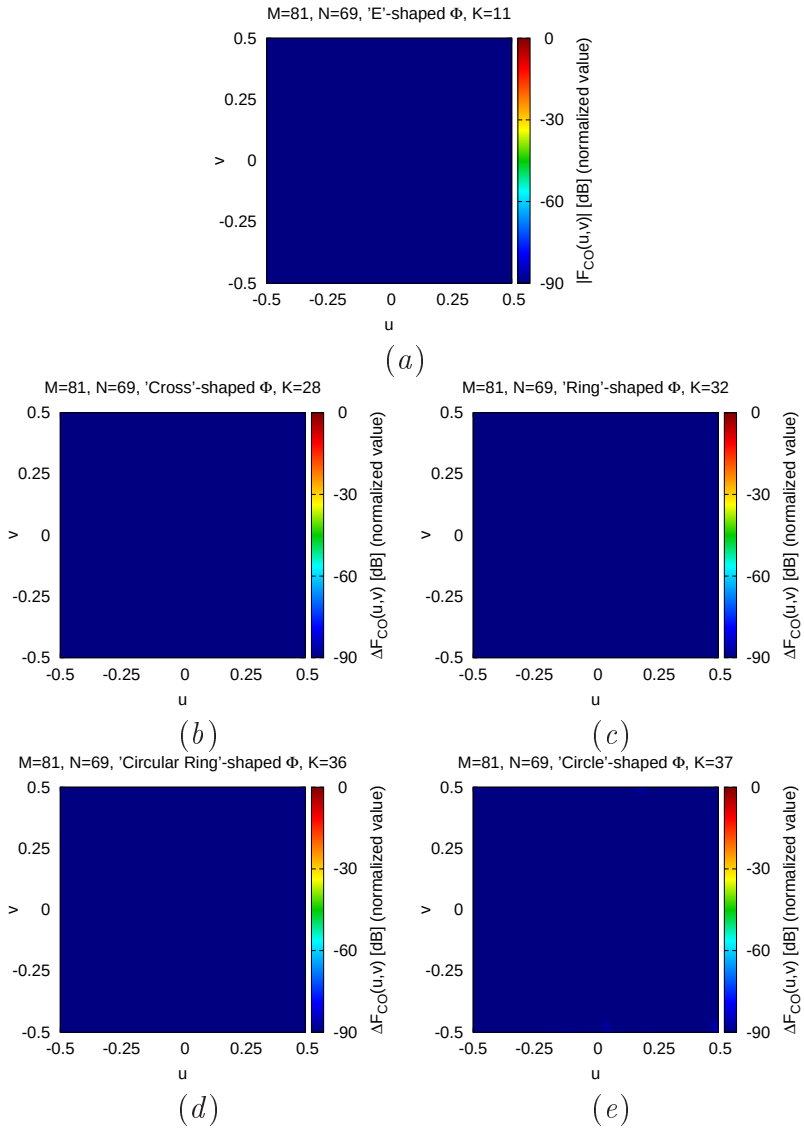

Figure 4.26: *Square Aperture* ($M \times N = 55 \times 55$, $\Delta x = \Delta y = 3.73 \times 10^{-1}\lambda$) - Plots of $\Delta F_{CO}(u,v)$ when assuming an (a) "E"-shaped $K = 11$, (b) "Cross"-shaped $K = 28$, (c) "Ring"-shaped $K = 32$, (d) "Circular Ring"-shaped $K = 36$ and (e) "Circle"-shaped $K = 37$ forbidden region.

4.3.3 Resume normalized errors and computational time in 81x69 test case

For the sake of completeness, the resume of the pattern mismatch ξ and the synthesis time Δt[2] for different Φ definitions (always assuming $\mathbf{F}^{ref}$ in Fig. 4.20(c) and Fig. 4.20(d) and $M = 81$, $N = 69$) is provided in Fig. 4.27. The illustrated results remark that:

(***i***) thanks to its closed-form nature (3.34), the synthesis process is extremely efficient whatever Φ shape and size (i.e., $\Delta t \in [1.40 \times 10^{-1}, 2.60 \times 10^{-1}]$ [s] - Fig. 4.27 - Tab. 4.4), as it happened also in the previous examples (i.e., $\Delta t \in [1.04 \times 10^{-1}, 2.32 \times 10^{-1}]$ [s] - Fig. 4.15; $\Delta t \in [1.03 \times 10^{-1}, 2.60 \times 10^{-1}]$ [s] - Tabs. 4.1-4.2-4.3);

(***ii***) despite the significantly increased problem size with respect to the "square aperture" test cases (i.e., $\frac{MN\rfloor_{square}}{MN\rfloor_{rect.}} \approx 0.54$), the pattern is reliably reproduced in all examples ($\xi < 8.0 \times 10^{-4}$ - Fig. 4.27).

These outcomes further validate the capability of the proposed method to efficiently exploit non-measurable currents $\mathbf{J}^{\mathcal{NR}}$ as a *DoF* to satisfy user-defined constraints on the reflectarray layout while yielding a *non-measurable* variation in the radiated field (Fig. 4.27).

[2]All Δt values refer to a non-optimized MATLAB implementation executed on a single-core laptop featuring a 2.20 GHz CPU clock.

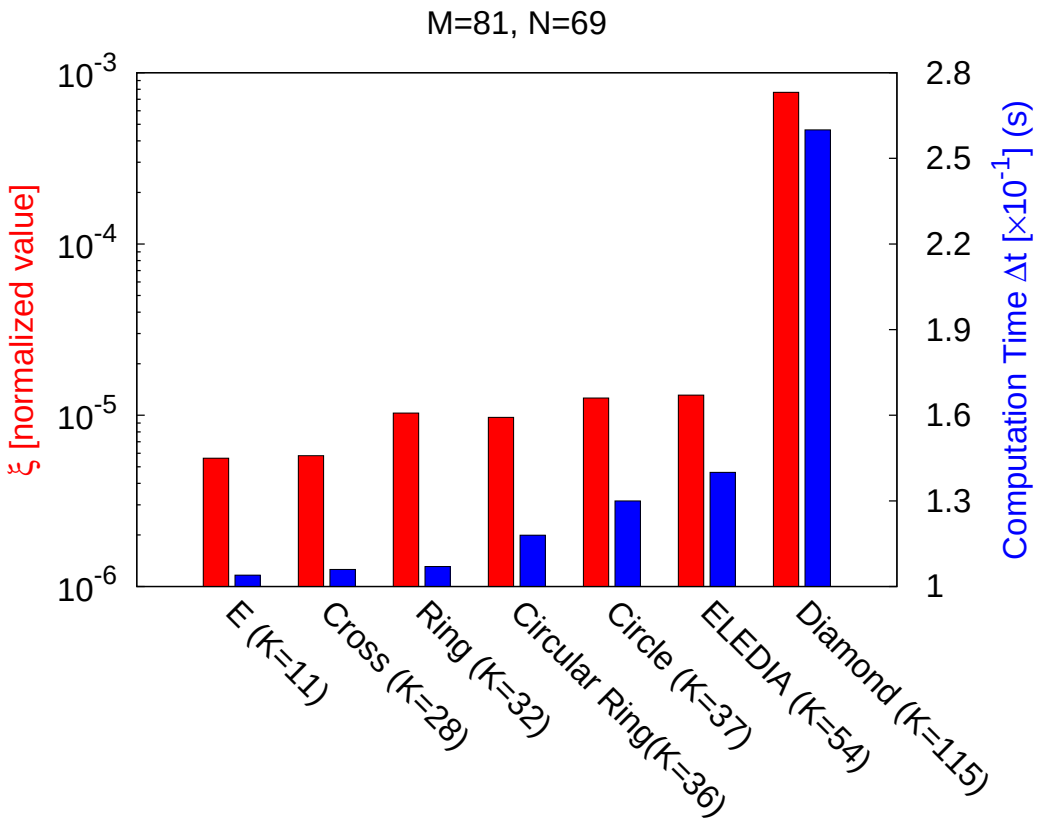

Figure 4.27: *Rectangular Aperture* ($M \times N = 81 \times 69$, $\Delta x = \Delta y = 3.07 \times 10^{-1}\lambda$) - Behaviour of ξ and Δt for different forbidden region shapes Φ.

Φ- Shape	K	ξ	Δt (s)
-	-	4.47×10^{-6}	-
E	11	5.51×10^{-6}	1.04×10^{-1}
Cross	28	5.81×10^{-6}	1.06×10^{-1}
Ring	32	1.05×10^{-5}	1.07×10^{-1}
Circular Ring	36	9.72×10^{-6}	1.15×10^{-1}
Circle	37	1.26×10^{-5}	1.29×10^{-1}
ELEDIA	54	1.31×10^{-5}	1.40×10^{-1}
Diamond	115	7.68×10^{-4}	2.60×10^{-1}

Table 4.4: *Rectangular Aperture* ($M \times N = 81 \times 69$, $\Delta x = \Delta y = 3.07 \times 10^{-1}\lambda$) - *Performance Assessment* - Resume on various test cases.

Chapter 5

Conclusions and Remarks

An innovative paradigm has been proposed for the design of reflectarray surface currents that satisfy both *radiation* and user-defined antenna *feasibility* constraints. To this end, the current synthesis problem has been formulated as an inverse source one, and its well-known non-uniqueness has been leveraged as a design *DoF*. By suitably exploiting the arising *non-measurable* sources, a closed-form solution for the design of reflectarray surface currents has been derived which does not require any iterative local/global optimization procedure and which inherently satisfies both the *radiation* and the *feasibility* design constraints. A selected set of numerical experiments has been illustrated to assess the effectiveness and potentialities of the design procedure when handling different aperture types/sizes and forbidden region definitions.

The numerical assessment has shown that

- the expression (3.34) enables to compute combinations of suitable current components $\mathbf{J}^{\mathcal{NR}}$ and $\mathbf{J}^{\mathcal{MN}}$ that satisfy user-defined current constraints while yielding a *non-measurable* variation in the radiated field with respect to $\mathbf{F}^{ref}$ (Sect. 4);

- the design method only features 1 control parameter (τ) whose choice can be reliably carried out by simple analysis of the Green matrix spectrum *knee* [(4.2) - Fig. 4.4];

- although the pattern matching error ξ slightly increases with the forbidden region size K, the proposed strategy turns out effective regardless of the complexity of Φ (e.g., $\xi \leq 4.34 \times 10^{-3}$ - Tab. 4.3) if the solvability condition

(3.31) is satisfied;

- owing to its closed-form nature (3.34), the synthesis process turns out numerically efficient (i.e., $\Delta t \leq 2.60 \times 10^{-1}$ [s] - Tab. 4.4) whatever Φ shape and size (e.g., Fig. 4.9).

Moreover, the methodological advancements of the paper with respect to the state-of-the-art includ:

(*i*) the formulation and development of a reflectarray current design paradigm which takes advantage of the existence of *non-measurable* surface sources to enhance the solution features according to user-defined objectives,

(*ii*) the derivation of *closed-form* formulas for the synthesis of reflectarray currents that inherently satisfy radiation and geometrical constraints.

Future works, beyond the scope of this work, will be aimed at the generalization of the introduced paradigm to take into account additional user constraints (e.g., regarding the feasible current solutions) as well as more complex/conformal geometries. Moreover, the integration of the proposed strategy with an automatic reflectarray unit-cell synthesis technique is currently under investigation.

Bibliography

[1] T. Clavier, N. Razavi-Ghods, F. Glineur, D. Gonzalez-Ovejero, E. de Lera Acedo, C. Craeye, and P. Alexander, "A global-local synthesis approach for large non-regular arrays," *IEEE Trans. Antennas Propag.*, vol. 62, no. 4, pp. 1596-1606, April 2014.

[2] Y. Rahmat-Samii and A. C. Densmore, "Technology trends and challenges of antennas for satellite communication systems," *IEEE Trans. Antennas Propag.*, vol. 63, no. 4, pp. 1191-1204, Apr. 2015.

[3] C. Coman, I. Lager, and L. Ligthart, "The design of shared aperture antennas consisting of differently sized elements," *IEEE Trans. Antennas Propag.*, vol. 54, no. 2, pp. 376-383, Feb. 2006.

[4] P. Minvielle, E. Tantar, A. Tantar, and P. Berisset, "Sparse antenna array optimization with the cross-entropy method," *IEEE Trans. Antennas Propag.*, vol. 59, no. 8, pp. 2862-2871, Aug. 2011.

[5] Y. Cailloce, G. Caille, I. Albert, and J. Lopez, "A Ka-band direct radiating array providing multiple beams for a satellite multimedia mission," in Proc. IEEE Int. Conf. Phased Array Syst. Techn., Dana Point, CA, May 21-25, 2000, pp. 403-406.

[6] J. Huang and J. A. Encinar, *Reflectarray antennas*. Piscataway, NJ, USA: IEEE Press/Wiley, 2008.

[7] R. J. Mailloux, *Phased Array Antenna Handbook*, 2nd ed. Norwood, MA: Artech House, 2005.

[8] P. Rocca, G. Oliveri, R. J. Mailloux, and A. Massa, "Unconventional phased array architectures and design methodologies - A review," *Proc. IEEE*, vol. 104, no. 3, pp. 544-560, Mar. 2016.

[9] D.-W. Duan and Y. Rahmat-Samii, "A generalized diffraction synthesis technique for high performance reflector antennas," in *IEEE Transactions on Antennas and Propagation*, vol. 43, no. 1, pp. 27-40, Jan. 1995.

[10] P. Rocca, N. Anselmi and A. Massa, "Interval Arithmetic for Pattern Tolerance Analysis of Parabolic Reflectors," in *IEEE Transactions on Antennas and Propagation*, vol. 62, no. 10, pp. 4952-4960, Oct. 2014.

[11] D. G. Berry, R. G. Malech, and W. A. Kennedy, "The reflectarray antenna," *IEEE Trans. Antennas Propag.*, vol. 11, no. 6, pp. 645-651, Nov. 1963.

[12] E. Carrasco, M. Barba and J. A. Encinar, "X-Band reflectarray antenna with switching-beam using PIN diodes and gathered elements," *IEEE Trans. Antennas Propag.*, vol. 60, no. 12, pp. 5700-5708, Dec. 2012.

[13] L. Marnat, R. Loison, R. Gillard, D. Bresciani and H. Legay, "Accurate synthesis of a dual linearly polarized reflectarray," in *2009 3rd European Conference on Antennas and Propagation*, Berlin, 2009, pp. 2523-2526.

[14] P. Rocca, L. Poli, N. Anselmi, M. Salucci and A. Massa, "Predicting antenna pattern degradations in microstrip reflectarrays through interval arithmetic," in *IET Microwaves, Antennas & Propagation*, vol. 10, no. 8, pp. 817-826, 5 6 2016.

[15] J. A. Encinar, "Design of two-layer printed reflectarray using patches of variable size," *IEEE Trans. Antennas Propag.*, vol. 49, no. 10, pp. 1403-1410, Oct. 2001.

[16] J. A. Encinar and J. A. Zornoza, "Broadband design of three-layer printed reflectarrays," *IEEE Trans. Antennas Propag.*, vol. 51, no. 7, pp. 1662-1664, Jul. 2003.

[17] J. A. Encinar, C. Tienda, M. Barba, E. Carrasco and M. Arrebola, "Analysis, design and prototyping of reflectarray antennas for space applications," in *2013 Loughborough Antennas & Propagation Conference*, Loughborough, UK, 2013, pp. 1-5.

[18] R. D. Javor, X.-D. Wu and K.Chang, "Beam steering of a microstrip flat reflectarray antenna," *Proceedings of IEEE Antennas and Propagation So-*

ciety International Symposium and URSI National Radio Science Meeting, Seattle, WA, USA, 1994, pp. 956-959 vol.2.

[19] D.-C. Chang and M.-C. Huang, "Multiple-polarization microstrip reflectarray antenna with high efficiency and low cross-polarization," in *IEEE Transactions on Antennas and Propagation*, vol. 43, no. 8, pp. 829-834, Aug. 1995.

[20] J. Huang, "Bandwidth study of microstrip reflectarray and a novel phased reflectarray concept," *IEEE Antennas and Propagation Society International Symposium*. 1995 Digest, Newport Beach, CA, USA, 1995, pp. 582-585 vol.1.

[21] F. S. Johansson, "A new planar grating-reflector antenna," in *IEEE Transactions on Antennas and Propagation*, vol. 38, no. 9, pp. 1491-1495, Sept. 1990.

[22] S. V. Hum, M. Okoniewski and R. J. Davies, "Realizing an electronically tunable reflectarray using varactor diode-tuned elements," in *IEEE Microwave and Wireless Components Letters*, vol. 15, no. 6, pp. 422-424, June 2005.

[23] L. Boccia, F. Venneri, G. Amendola and G. Di Massa, "Application of varactor diodes for reflectarray phase control," *IEEE Antennas and Propagation Society International Symposium*, San Antonio, TX, USA, 2002, pp. 132-135.

[24] L. Boccia, G. Amendola and G. D. Massa, "Performance Improvement for a Varactor-Loaded Reflectarray Element," in *IEEE Transactions on Antennas and Propagation*, vol. 58, no. 2, pp. 585-589, Feb. 2010.

[25] P. Ratajczak, J. Baracco and P. Brachat, "Adjustable High Impedance Surface for Active Reflectarray Applications," *The Second European Conference on Antennas and Propagation, EuCAP 2007*, Edinburgh, 2007, pp. 1-6.

[26] K. K. Kishor, S. V. Hum, "An Amplifying Reconfigurable Reflectarray Antenna", in *IEEE Transactions on Antennas and Propagation*, vol. 60, no. 1, pp. 197-205, 2012.

[27] D. F. Sievenpiper, J. H. Schaffner, H. J. Song, R. Y. Loo and G. Tangonan, "Two-dimensional beam steering using an electrically tunable impedance surface," in *IEEE Transactions on Antennas and Propagation*, vol. 51, no. 10, pp. 2713-2722, Oct. 2003.

[28] M. Riel and J. Laurin, "Design of an Electronically Beam Scanning Reflectarray Using Aperture-Coupled Elements," in *IEEE Transactions on Antennas and Propagation*, vol. 55, no. 5, pp. 1260-1266, May 2007.

[29] S. V. Hum, M. Okoniewski and R. J. Davies, "Modeling and Design of Electronically Tunable Reflectarrays," in *IEEE Transactions on Antennas and Propagation*, vol. 55, no. 8, pp. 2200-2210, Aug. 2007.

[30] C. Liu and S. V. Hum, "An Electronically Tunable Single-Layer Reflectarray Antenna Element With Improved Bandwidth," in *IEEE Antennas and Wireless Propagation Letters*, vol. 9, pp. 1241-1244, 2010.

[31] G. Perez-Palomino, J. A. Encinar, M. Barba and E. Carrasco, "Design and evaluation of multi-resonant unit cells based on liquid crystals for reconfigurable reflectarrays," in *IET Microwaves, Antennas & Propagation*, vol. 6, no. 3, pp. 348-354, 21 February 2012.

[32] G. Perez-Palomino, P. Baine, R. Dickie, M. Bain, J. A. Encinar, R. Cahill, M. Barba and G. Toso, "Design and Experimental Validation of Liquid Crystal-Based Reconfigurable Reflectarray Elements With Improved Bandwidth in F-Band," in *IEEE Transactions on Antennas and Propagation*, vol. 61, no. 4, pp. 1704-1713, April 2013.

[33] D. Rodrigo, L. Jofre and J. Perruisseau-Carrier, "Unit Cell for Frequency-Tunable Beamscanning Reflectarrays," in *IEEE Transactions on Antennas and Propagation*, vol. 61, no. 12, pp. 5992-5999, Dec. 2013.

[34] S. Bildik, S. Dieter, C. Fritzsch, W. Menzel and R. Jakoby, "Reconfigurable Folded Reflectarray Antenna Based Upon Liquid Crystal Technology," in *IEEE Transactions on Antennas and Propagation*, vol. 63, no. 1, pp. 122-132, Jan. 2015.

[35] X. Yang, S. Xu, F. Yang, M. Li, H. Fang, Y. Hou, S. Jiang and L. Liu, "A Mechanically Reconfigurable Reflectarray With Slotted Patches of Tunable Height," in *IEEE Antennas and Wireless Propagation Letters*, vol. 17, no. 4, pp. 555-558, April 2018.

[36] S. Costanzo, F. Venneri, A. Raffo and G. Di Massa, "Dual-Layer Single-Varactor Driven Reflectarray Cell for Broad-Band Beam-Steering and Fre-

quency Tunable Applications," in *IEEE Access*, vol. 6, pp. 71793-71800, 2018.

[37] J. A. Encinar and J. A. Zornoza, "Three-layer printed reflectarrays for contoured beam space applications," *IEEE Trans. Antennas Propag.*, vol. 52, no. 5, pp. 1138-1148, May 2004.

[38] D. M. Pozar, S. D. Targonski, and R. Pokuls, "A shaped-beam microstrip patch reflectarray," *IEEE Trans. Antennas Propag.*, vol. 47, no. 7, pp. 1167-1173, Jul 1999.

[39] D. R. Prado, M. Arrebola, M. R. Pino, and F. Las-Heras, "Complex reflection coefficient synthesis applied to dual-polarized reflectarrays with cross-polar requirements," *IEEE Trans. Antennas Propag.*, vol. 63, no. 9, pp. 3897-3907, Sept. 2015.

[40] P. Robustillo, J. Zapata, J. A. Encinar and J. Rubio, "ANN Characterization of Multi-Layer Reflectarray Elements for Contoured-Beam Space Antennas in the Ku-Band," in *IEEE Transactions on Antennas and Propagation*, vol. 60, no. 7, pp. 3205-3214, July 2012.

[41] M. Zhou, S. B. Soerensen, O. S. Kim, E. Joergensen, P. Meincke and O. Breinbjerg, "Direct Optimization of Printed Reflectarrays for Contoured Beam Satellite Antenna Applications," in *IEEE Transactions on Antennas and Propagation*, vol. 61, no. 4, pp. 1995-2004, April 2013.

[42] M. Zhou, O. Borries and E. Joergensen, "Design and Optimization of a Single-Layer Planar Transmit-Receive Contoured Beam Reflectarray With Enhanced Performance," in *IEEE Transactions on Antennas and Propagation*, vol. 63, no. 4, pp. 1247-1254, April 2015.

[43] D. R. Prado, J. A. L. Fernandez, M. Arrebola, M. R. Pino and G. Goussetis, "General Framework for the Efficient Optimization of Reflectarray Antennas for Contoured Beam Space Applications," in *IEEE Access*, vol. 6, pp. 72295-72310, 2018.

[44] J. A. Zornoza, R. Leberer, J. A. Encinar and W. Menzel, "Folded multilayer microstrip reflectarray with shaped pattern," in *IEEE Transactions on Antennas and Propagation*, vol. 54, no. 2, pp. 510-518, Feb. 2006.

[45] E. Carrasco, M. Arrebola, J. A. Encinar and M. Barba, "Demonstration of a Shaped Beam Reflectarray Using Aperture-Coupled Delay Lines for LMDS Central Station Antenna," in *IEEE Transactions on Antennas and Propagation*, vol. 56, no. 10, pp. 3103-3111, Oct. 2008.

[46] A. Zeitler, J. Lanteri, C. Pichot, C. Migliaccio, P. Feil and W. Menzel, "Folded Reflectarrays With Shaped Beam Pattern for Foreign Object Debris Detection on Runways," in *IEEE Transactions on Antennas and Propagation*, vol. 58, no. 9, pp. 3065-3068, Sept. 2010.

[47] E. Carrasco, M. Barba, J. A. Encinar, M. Arrebola, F. Rossi and A. Freni, "Design, Manufacture and Test of a Low-Cost Shaped-Beam Reflectarray Using a Single Layer of Varying-Sized Printed Dipoles," in *IEEE Transactions on Antennas and Propagation*, vol. 61, no. 6, pp. 3077-3085, June 2013.

[48] M. Karimipour, A. Pirhadi and N. Ebrahimi, "Accurate method for synthesis of shaped-beam non-uniform reflectarray antenna," in *IET Microwaves, Antennas & Propagation*, vol. 7, no. 15, pp. 1247-1253, 10 December 2013.

[49] A. Tayebi, J. Tang, P. R. Paladhi, L. Udpa, S. S. Udpa and E. J. Rothwell, "Dynamic Beam Shaping Using a Dual-Band Electronically Tunable Reflectarray Antenna," in *IEEE Transactions on Antennas and Propagation*, vol. 63, no. 10, pp. 4534-4539, Oct. 2015.

[50] J. Yu, J. Wang, L. Chen, J. Yang and X. Shi, "Design of circularly polarised beam-shaped RAs using a single layer of concentric dual split loops," in *IET Microwaves, Antennas & Propagation*, vol. 10, no. 14, pp. 1515-1521, 19 11 2016.

[51] D. R. Prado, M. Arrebola, M. R. Pino, R. Florencio, R. R. Boix, J. A. Encinar, F. Las-Heras, "Efficient Crosspolar Optimization of Shaped-Beam Dual-Polarized Reflectarrays Using Full- Wave Analysis for the Antenna Element Characterization," in *IEEE Transactions on Antennas and Propagation*, vol. 65, no. 2, pp. 623-635, Feb. 2017.

[52] G. Carluccio, A. Mazzinghi and A. Freni, "Design and Manufacture of Cosecant-Squared Complementary Reflectarrays for Low-Cost Applica-

tions," in *IEEE Transactions on Antennas and Propagation*, vol. 65, no. 10, pp. 5220-5227, Oct. 2017.

[53] H. R. Phelan , "Spiralphase refl ctarray for multitarget radar," *Microwave Journal* , Vol. 20 , July 1977 , pp. 67-73 .

[54] C. S. Malagisi, "Microstrip disc element reflectarray," *Electronics and Aerospace Systems Convention*, Sep. 1978.

[55] R.E. Munson, H. Haddad, and J. Hanlen, "Microstrip reflectarray antenna for satellite communication and RCS enhancement or reduction", *US Patent 4684952*, Aug. 1987.

[56] J. Huang, "Microstrip reflectarray," in *IEEE Int. AP-S Symposium*, Jun. 1991, pp. 612-615.

[57] J. Huang and R. J. Pogorzelski, "A Ka - band microstrip reflectarray with elements having variable rotation angles," *IEEE Trans. Antennas & Propagation*, vol. 46, May 1998, pp. 650-656.

[58] D. M. Pozar and T. A. Metzler, "Analysis of a reflectarray antenna using microstrip patches of variable size," in *Electronics Letters*, vol. 29, no. 8, pp. 657-658, 15 Apr. 1993.

[59] D. M. Pozar, S. D. Targonski, and H. D. Syrigos, "Design of millimiter wave microstrip reflectarrays," *IEEE Trans. Antennas Propag.*, vol. 45, no. 2, pp. 287-296, Feb. 1997.

[60] M. R. Chaharmir, R. James, J. Ethier, J. Shaker and M. Cuhaci, "Reflectarray design using printed electronics technology," in *Electronics Letters*, vol. 48, no. 22, pp. 1388-1389, October 25 2012.

[61] J. Encinar, M. Arrebola, and. G. Toso, "Design of a Tx/Rx reflectarray for space applications," *Proceedings EuCAP 2007*, Nov. 2007.

[62] D. M. Pozar, "Radiation and scattering from a microstrip patch on a uniaxial substrate," *IEEE Trans. Antennas Propag.*, vol. 35, no. 6, pp. 613-621, Jun. 1987.

[63] L. Moustafa, R. Gillard, F. Peris, R. Loison, H. Legay, and E. Girard, "The Phoenix cell: a new reflectarray cell with large bandwidth and rebirth capabilities," *IEEE Antennas Wireless Propag. Lett.*, vol. 10, pp. 71-74, Jan. 2011.

[64] R. Deng, F. Yang, S. Xu, and M. Li, "A low-cost metal-only reflectarray using modified slot-type phoenix element with 360° phase coverage," *IEEE Trans. Antennas Propag.*, vol. 64, no. 4, pp. 1556-1560, Apr. 2016.

[65] T. Makdissy, R. Gillard, E. Fourn, M. Ferrando Rocher, E. Girard, H. Legay, and L. Le Coq, "'Phoenix' reflectarray unit cell with reduced size and inductive loading," *IET Microw. Antennas Propag.*, vol. 10., no. 12, pp. 1363-1370, May 2016.

[66] R. Deng, F. Yang, S. Xu and M. Li, "A 100-GHz Metal-Only Reflectarray for High-Gain Antenna Applications," in *IEEE Antennas and Wireless Propagation Letters*, vol. 15, pp. 178-181, 2016.

[67] O. M. Bucci, G. Franceschetti, G. Mazzarella and G. Panariello, "Intersection approach to array pattern synthesis," in *IEE Proceedings H - Microwaves*, Antennas and Propagation, vol. 137, no. 6, pp. 349-357, Dec. 1990.

[68] A. Ludwig, "Calculation of scattered patterns from asymmetrical reflector," *Technical Report 32-1430*, Jet Propulsion Laboratory, Feb 1970.

[69] F. Las-Heras, "Sequential reconstruction of equivalent currents from cylindrical near field," *Electron. Lett.*, vol. 35, no. 3, pp. 211-212, Feb. 1999.

[70] F. Las-Heras, "Radial field retrieval for current reconstruction from spherical acquisition," *Electron. Lett.*, vol. 36, no. 10, pp. 867-869, May 2000.

[71] Y. Alvarez, F. Las-Heras, and M. R. Pino, "Reconstruction of equivalent currents distribution over arbitrary three-dimensional surfaces based on integral equation algorithms," *IEEE Trans. Antennas Propag.*, vol. 55, no. 12, pp. 3460-3468, Dec. 2007.

[72] Y. Alvarez, A. Dominguez-Casas, C. Garcia-Gonzalez, and F. Las-Heras, "Geometry reconstruction of metallic bodies using the sources reconstruction method," *IEEE Antennas Wireless Propag. Lett.*, vol. 9, pp. 1197-1200, 2010.

[73] M. D. Migliore, "Minimum trace norm regularization (MTNR) in electromagnetic inverse problems," *IEEE Trans. Antennas Propag.*, vol. 64, no. 2, pp. 630-639, Feb. 2016.

[74] S. Caorsi and G. L. Gragnani, "Inverse scattering method for dielectric objects based on the reconstruction of nonmeasurable equivalent current density," *Radio Sci.*, vol. 34, no. 1, pp. 1-8, Jan. 1999.

[75] P. Rocca, M. Donelli, G. L. Gragnani, and A. Massa, "Iterative multiresolution retrieval of non-measurable equivalent currents for the imaging of dielectric objects," *Inverse Problems*, vol. 25, id. 055004, pp. 1-15, 2009.

[76] G. Oliveri, Y. Zhong, X. Chen, and A. Massa, "Multi-resolution subspace-based optimization method for inverse scattering," *J. Opt. Soc. Am. A*, vol. 28, no. 10, pp. 2057-2069, Oct. 2011.

[77] L. Poli, G. Oliveri, F. Viani, and A. Massa, "MT-BCS-based microwave imaging approach through minimum-norm current expansion," *IEEE Trans. Antennas Propag.*, vol. 61, no. 9, pp. 4722-4732, Sep. 2013.

[78] A. Ludwig, "The definition of cross polarization," *IEEE Trans. Antennas Propag.*, vol. 21, no. 1, pp. 116-119, Jan. 1973.

[79] T. A. Metzler, "Design and analysis of a microstrip reflectarray," PhD Thesis, Univ. Massachusetts, Amherst, 1992.

[80] C.A. Balanis, *Antenna theory: analysis and design*, Wiley & Sons., 2005, 3rd edn.

[81] TICRA, *GRASP User Manual* [Online], Copenhaghen, Denmark. Available: http://www.ticra.com/products/software/grasp.